UNIVERSITÀ DEGLI STUDI DI PALERMO

Dottorato in Scienze Fisiche e Chimiche
Dipartimento di Fisica e Chimica - "Emilio Segrè"

The influence of the explosion anisotropies and of the circumstellar medium on the evolution of Supernova Remnants and on particle acceleration at their shocks

Settore Scientifico Disciplinare - FIS/05 - Astronomia e Astrofisica

TESI DI
VINCENZO SAPIENZA

COORDINATORE DEL DOTTORATO
PROF. MARCO CANNAS

TUTOR
PROF. MARCO MICELI

XXXVI CICLO - ANNO ACCADEMICO 2023-2024

Abstract

This thesis is dedicated to the analysis of X-ray observations of supernova remnants (SNRs), complemented with the synthesis of X-ray spectra employing 3-Dimensional Magneto-Hydrodynamic (MHD) models. The primary objective of this work is to acquire a deeper understanding of how the supernova (SN) explosion and the circumstellar medium (CSM) impact both on the evolution of SNRs and on the mechanisms governing particle acceleration. In particular, I address three key challenges: i) investigating the impact of the environment on electron acceleration through the analysis of the non-thermal radiation in the Kepler's SNR, ii) revealing explosion anisotropies and wind residuals in the Vela SNR through the analysis of X-ray observations, iii) predicting the X-ray emission of the fast expanding ejecta in SN 1987A through the synthesis of the XRISM-Resolve spectrum from a dedicated 3D MHD model.

Synchrotron X-ray emission in young SNRs serves as a diagnostic tool to explore the population of high-energy electrons accelerated at the shock front and to understand the acceleration process. By conducting a spatially resolved spectral analysis using *NuSTAR* and *XMM-Newton* observations of Kepler's SNR, I study the non-thermal emission in hard X-rays, using a synchrotron radiation model in the loss-limited regime. The analysis reveals two distinct regimes of particle acceleration characterized by different Bohm factors. In the northern region, where the shock interacts with a dense CSM, I observe more efficient acceleration compared to the southern region, where the shock velocity is higher, and there are no indications of shock interaction with dense CSM. These results suggest an enhanced efficiency of the acceleration process in regions where the shock-CSM interaction generates an amplified and turbulent magnetic field.

In the proposed scenario, the synchrotron cooling time scale aligns with the acceleration time scale. Conversely, the low speed of a shock propagating in a dense medium is expected to increase the acceleration time scale, resulting in a lower maximum elec-

tron energy (and fainter non-thermal X-ray flux) for a given SNR age. To deepen this scenario at smaller scales, I investigate the temporal evolution of the synchrotron flux, taking advantage of the two deepest *Chandra*/ACIS X-ray observations of Kepler's SNR, performed in 2006 and 2014. Analyzing the spectra of different filaments in the northern shell, I measure their proper motion and estimate the ratio between the acceleration time-scale and the synchrotron cooling time. I identify a region with very low shock velocity and find that the acceleration time-scale is longer than the synchrotron cooling time therein. In this region, I measure a significant decrease in flux from 2006 to 2014, thus obtaining the first evidence of fading synchrotron emission in Kepler's SNR. Overall, these results contribute to a coherent understanding of the diverse electron acceleration regimes observed in Kepler's SNR and associated with its expansion into a non-uniform CSM.

Core-collapse SNRs have intricate morphologies arising from inherent asymmetries in the SN explosion and the propagation of explosion shock waves in highly heterogeneous environments. The Vela SNR, indeed, exhibits multiple ejecta fragments, commonly referred to as shrapnel, extending beyond the forward shock. Recent investigations have identified elevated silicon (Si) abundance in two specific shrapnel, denoted as A and G, positioned in opposite directions relative to the SNR center. This observation hints at the potential presence of a Si-rich jet-counterjet structure. To address this issue I conduct an analysis of an *XMM-Newton* observation focused on a luminous clump situated behind shrapnel G, which aligns with the trajectory connecting shrapnel A and G, with the aim to scrutinize its physical and chemical properties, determining its association with the supposed jet-like structure. I identify two distinct structures, each exhibiting different physical characteristics. The first structure displays a remarkable elongation along the axis connecting shrapnel A and G. Despite its X-ray spectrum being considerably softer than that of the other two shrapnel, hindering Si abundance determination, its physical and chemical properties are found to be consistent with those of shrapnel A and G. The second structure exhibits a higher temperature and resembles a thin filament. Thanks to the analysis of archived ROSAT data, I find that this filament is part of an extensive and cohesive structure identified in the western rim of the shell. This feature is interpreted as a signature of a prior interaction between the remnant and the stellar wind from its progenitor star. The peculiar Ne/O ratio identified in the wind residual raises the possibility of a Wolf-Rayet progenitor for the Vela SNR.

As for the case of SN 1987A, my research consists in evaluating the efficacy of the newly launched XRISM-Resolve high-resolution spectrometer in discerning distinctive signatures associated with shocked ejecta in SN 1987A. This celestial object presents a unique opportunity to scrutinize the transformation of a SN into a nascent SNR. Historically, the dominant source of X-ray emission has been the shocked CSM, with no conclusive identification of shocked ejecta. However, recent investigations provide compelling indications that the future X-ray emissions from SN 1987A will increasingly

originate from the ejecta. Leveraging a state-of-the-art, self-consistent MHD simulation that intricately depicts the evolutionary stages from SN 1987A to its remnant, I generated a synthetic XRISM-Resolve spectrum for SN 1987A performance verification phase observation anticipated in 2024. My predictions distinctly highlight the prominent role of shocked ejecta in shaping the emission line profiles. Doppler broadening, resulting from the bulk motion along the line of sight of the rapidly expanding ejecta, is demonstrated to significantly increase the line widths beyond previously observed values. The quantitative comparison between my synthetic spectra and the actual XRISM spectra will provide a robust diagnostic for establishing a direct correlation between the broadened line emission and the newly shocked ejecta. This correlation, in turn, will facilitate the retrieval of essential information regarding the dynamics and chemical composition of the ejecta from the X-ray emission.

Contents

1 Introduction

In the vast expanse of the cosmos, Supernova Remnants (SNRs) stand as enduring echoes of cataclysmic stellar explosions, namely Supernovae (SNe), that both dazzle the eye and challenge the mind. These remnants are not just stunning visual spectacles, they are also cosmic powerhouses, crucial to revealing secrets about particle acceleration, shock physics, and the genesis of essential cosmic elements.

The matter surrounding the explosion site, wiped out by the shock wave generated in the SN explosion, is intensely heated and compressed. Concurrently, it mixes with fragments from the progenitor star, expelled at supersonic speeds, commonly referred to as the ejecta. The dynamic interaction between the ejecta, sculpted by the SN explosion, and the encompassing ambient medium, intricately influences SNRs morphology, emission characteristics, and the mechanisms fostering the acceleration of cosmic particles. Disentangling the respective roles of the ejecta and the circumstellar medium (CSM) in shaping SNR morphology is crucial to understand the nature of SN explosions, the behavior of massive stars before their deaths, and the subsequent interaction between the expelled stellar material and the surrounding interstellar environment. Moreover, the study of this non-trivial interplay sheds light on the emission mechanisms within SNRs, providing invaluable insights into particle acceleration processes and the origin of cosmic rays. In the end, the feedback loop between the SN explosion and the CSM influences the surrounding interstellar medium (ISM), triggering new star formation, enriching the environment with heavy elements synthesized in the explosion, and influencing the dynamics of galactic ecosystems.

This thesis is aimed at comprehending the profound impact of both the SN explosion and the CSM on the evolution of SNRs and the mechanisms driving particle acceleration. To achieve this objective, I harness the diagnostic capabilities of X-ray spectroscopy and imaging. This involves a comprehensive analysis of X-ray observations and the synthesis of X-ray emission spectra derived from magneto-hydrodynamic (MHD) simulations.

Additionally, I exploit radio and γ-ray emission to complement and enrich the insights obtained from these analyses.

This chapter is structured as follows: In Section 1.1, the mechanisms driving SN explosions are described; Section 1.2 delves into shocks physics, its impact on the evolution of SNRs, and the classification of SNRs; Section 1.3 provides an in-depth review of the thermal emission processes within the X-ray emitting plasma; Section 1.4 explores the acceleration mechanisms operative within SNRs; Additionally, Section 1.5 and Section 1.6 respectively cover the non-thermal X-ray emission and the γ-ray emission arising from particle acceleration; Finally, Section 1.7 presents an overview of the thesis' structure and outline.

1.1 SN Explosion

The term Super-nova, defined for the first time by Baade & Zwicky (1934b), denotes an immensely powerful explosion which usually achieves remarkably intense peak luminosity ($L \approx 10^{42}$ erg/s). The relics of the progenitor star, namely ejecta, with a mass which usually spans in the range of 10^{33} g, are propelled into the CSM at extremely high speeds (around $\sim 10^4$ km/s), with a typical kinetic energy of the order of $\sim 10^{51}$ erg (1 foe).

The commonly used classification scheme for SNe is based on the the features observed in optical spectra and it was proposed by Minkowski (1941). This scheme divides the SN into two primary categories: Type I and Type II, alongside secondary classes (Ia, Ib, Ic, IIb, IIP, IIL). Type I SNe lack H lines in their optical spectra. If in a SN event Si lines are evident, then it will be classified as a *Type Ia SN*. If Si lines are absent but He lines are present, it will be classified as a *Type Ib SN*. If both Si and He lines are missing, it falls into the *Type Ic SN* category. Type II SNe, as a contrary, exhibit the presence of H lines in their optical spectra. Further differentiation within this category considers optical spectral traits and light curve shapes. *Type IIb Supernovae* exhibit H lines only in their early phases. *Type IIL Supernovae* (Linear) display a linear decay in their light curve. *Type IIP Supernovae* (Plateau) showcase a light curve featuring a sustained luminosity phase followed by a linear decline.

Beside this phenomenological classification, SNe are distinguished into two broad classes based on the physical explosion mechanisms (Hoyle & Fowler 1960). These two classes are Core-Collapse SNe (CCSNe) and thermonuclear SNe or Type Ia SNe (SN Ia).

1.1.1 Core-Collapse Explosion

CCSNe mark the conclusion of the life cycle of stars with zero age main sequence mass $M \gtrsim 8 M_\odot$. Throughout their lifespan, these stars progress through various cycles of

nuclear burning and contraction, leading to a layered structure. Starting from the core and extending outward, at the very end of massive star's life one expects the presence of: Iron-group elements at the core, followed by layers of Silicon-group elements, Oxygen and Magnesium (neon burning product), then layers rich in Magnesium and Neon (carbon-burning products), followed by a Carbon Shell, a Helium Shell, and an outer envelope composed of unprocessed Hydrogen-rich material.

The formation of the Iron-group core marks the onset of the end of the star's life. Indeed both fusion and fission processes involving Iron are endergonic (they require an energy input to take place), because the nuclear binding energy has a maximum when the atomic weight is around 56 amu. As a consequence, the inner part of the stellar core is accreted by Fe-rich "ashes", where nuclear burning does not occur. This inner core is sustained in hydrostatic equilibrium by the gradient of the electron degenerate pressure, which can counterbalance the gravitational force, provided that the mass M_i is lower than the Chandrasekhar limit ($M_{Ch} \sim 1.44\ Y_e^2\ \mathrm{M}_\odot$, where Y_e is the electron fraction). When this limit is exceeded, the collapse of the core into a proto-neutron star (PNS) liberates a gravitational energy of about $E \sim GM_i^2/R_{ns} \sim 10^{53}$ erg, R_{ns} being the PNS radius (of the order of 10 km). The majority ($\sim 99\%$) of this energy is radiated in the form of neutrinos, as attested by the observation of a neutrino burst linked to the explosion of SN 1987A (Hirata et al. 1987). The remaining $\sim 1\%$ of the total energy is typically released as kinetic energy of the ejecta.

As the PNS forms, the collapse abruptly halts (core bounce) and drives a shock wave through the inward-falling matter. However, the dissipation of kinetic energy in the matter swept up by the shock raises the temperature, creating high-energy photons. These photons break down Iron nuclei into free nucleons, trough photo-dissociation processes. The photo-disintegration drains approximately $1.7{\times}10^{52}$ erg/$M_\odot$ from the thermal reservoir, reducing the post-shock pressure. Within a millisecond after the core bounce, the shock wave stalls while it is still inside the Fe core.

A possible mechanism to re-energize the shock wave consists in the absorption of a fraction of the neutrinos escaping the PNS (also referred as neutrino-heating), in the post-shock medium (the so-called "gain region") and yet, some 2-D models fail in reproducing the SN explosion. To overturn this long-standing problem, recent researches, based on 3-D simulations, focus on the role of instabilities in the accretion shock, as they can help to enhance the neutrino-energy deposition in the gain region around the PNS. A prominent role is played by the convection instability, which enhances the dwell time in the gain region and significantly improves the efficiency of the neutrino heating. Moreover, the non-spherically symmetric standing accretion shock instability (SASI, Blondin et al. 2003), may also help to explain asymmetries in the explosions and NS kicks, as well as the distribution of pulsar spins (Blondin & Mezzacappa 2007). For reviews on the subject the reader can also see Woosley & Janka (2005); Mezzacappa (2005); Janka et al. (2007); Foglizzo (2016) and Janka (2017).

Another proposed mechanism contributing to a successful CCSN explosion, beyond neutrino energy deposition, involves considering the amplified stellar magnetic field resulting from differential rotation and compression. This process could trigger the formation of magneto-centrifugal jets, which drive the explosion (Wheeler et al. 2002). Indeed, long duration γ-ray bursts (intense flashes of γ-ray radiation in a highly collimated beam with a duration of only $2 - 30$ s) are usually associated with very energetic supernovae called hypernovae (e.g., Izzo et al. 2019). These events, likely driven by jets, find natural explanation within the framework of magneto-rotational explosions (Obergaulinger et al. 2009; Obergaulinger & Aloy 2020; Aloy & Obergaulinger 2021; Obergaulinger & Aloy 2021, 2022). Moreover, the potential for jet formation due to the stellar magnetic field raises the prospect of observing "normal" CCSNe exhibiting jet-like components.

1.1.2 Thermonuclear Explosion

Type Ia SNe are the result of a thermonuclear explosion that occurs in a binary system containing a carbon-oxygen (C/O) White Dwarf (WD). When a WD accretes sufficient material from the companion star to approach the Chandrasekhar mass limit, its core can reach $\sim 3 \times 10^9$ g cm^{-3} in density and $\sim 2 \times 10^8$ K in temperature. Under these extreme conditions, the fusion reactions of carbon and oxygen turn into a runaway process, which ultimately leads to the complete disruption of the WD (Nomoto et al. 1984).

The light curves observed in Type Ia SNe exhibit remarkable similarity, showcasing low variations in peak brightness. This consistency supports the hypothesis that all Type Ia SNe originate from explosions of similar objects that become unstable within a narrow range of conditions. Leveraging the uniformity observed in the Type Ia SN sample, researchers have established an empirical relationship between their peak brightness and the decay in magnitude 15 days after the peak (Phillips 1993). This relationship enables the calibration of the absolute peak brightness for each event. Consequently, Type Ia SNe serve as exceptional standard candles, extensively employed in cosmological investigations to accurately calculate distances in the Universe.

However, the precise nature of thermonuclear SN explosions remains somewhat elusive. C/O WD need to accumulate matter in order to reach the Chandrasekhar limit, indicating that thermonuclear SNe should occur in a binary system (Whelan & Iben 1973). Two scenarios for the progenitor systems were proposed:

1. the *single degenerate (SD)* scenario, in which the companion for the WD is either a main sequence star, or a post main sequence star;

2. the *double degenerate (DD)* scenario, in which the binary systems is composed by two WDs.

In the SD scenario, as the companion star fills its Roche lobe, some matter starts to spill from the Lagrangian point (L1) onto the WD, augmenting its mass until surpassing the Chandrasekhar limit, this increased mass triggers the runaway thermonuclear explosion, leading to the birth of a Type Ia SN. Conversely, the DD scenario occurs when two WDs, jointly possessing a mass surpassing the Chandrasekhar limit, collide and merge, initiating the process culminating in a Type Ia supernova.

It has to be said that both the SD and DD scenarios present their advantages and drawbacks. Historically, the SD scenario held considerable favor for an extended period because it naturally accounts for the uniformity observed in the light curves of Type Ia SNe. Additionally, this scenario provides a straightforward explanation for the explosion mechanism, attributing it to the growth of the WD through accretion from a companion star. However, this scenario is challenged by different aspects, including the narrow mass accretion range for a stable growth of the WD and the lack of the observations of survived companion stars. Presently, the paradigm has shifted in favor of the DD scenario. Recent advancements have addressed the challenges within this scenario, demonstrating the feasibility for mergers of WDs to result in explosions (Pakmor et al. 2010). These explosions also successfully replicate the uniformity observed in the light curves of Type Ia SNe (Pakmor et al. 2012).

However, differences between the scenarios extend to the environment of the explosion: DD explosions are expected to occur in a relatively homogeneous medium, while SD explosions often take place complex circumstellar environment, which is evident in some observed SNRs, e.g. Tycho's SNR and Kepler's SNR. In the end, observational evidences reveal that a mix of DD and SD progenitors might be necessary to explain observed SN rates, indicating that neither scenario alone can entirely account for all observed SNe Ia (Greggio et al. 2008).

1.2 The aftermath of the Explosion

The term SNR encompass the ensemble of structures resulting from a supernova explosion. Core collapse SNRs, as a result of their explosion mechanism, host a compact remnant such as a NS or a Black Hole. Beyond the presence of the compact remnant, the explosion of a SN generates a forceful blast wave, known as the forward shock, which sweeps the surrounding ambient medium accelerating, compressing and heating it. The ejecta behind the forward shock cool down rapidly because of their adiabatic expansion. However, the deceleration of the forward shock due to the interaction with the ambient medium produces a reverse shock, moving inward with respect to the ejecta rest frame, which sweeps and heats them (McKee 1974)[1]. The schematic structure of an SNR is illustrated in Figure 1.1. Moving from inner to outer radii there are: the freely expanding

[1] This year marks the 50th anniversary of the reverse shock

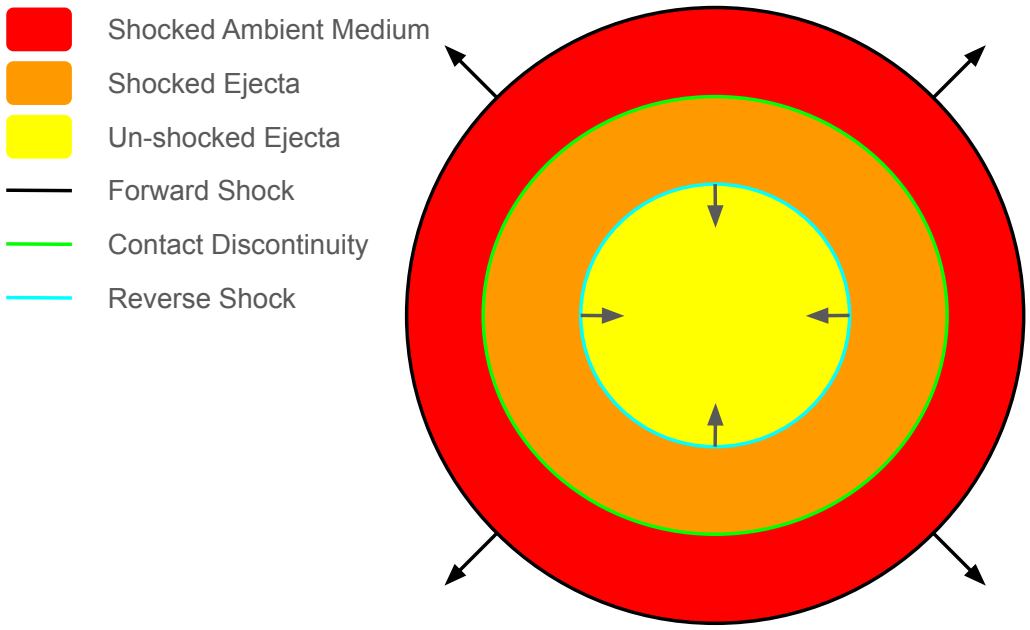

Figure 1.1: A sketch of the structure of a SNR, not drawn to scale. The contact discontinuity separates the shocked ambient medium from the shocked ejecta, which are swept by the forward shock and the reverse shock respectively.

and unshocked ejecta (in yellow), the reverse shock (cyan solid line), shocked ejecta (in orange), the contact discontinuity (green solid line) which divides the shocked ejecta from the shocked ambient medium (in red) and the forward shock (black solid line). Outside the circles stands the unshocked ambient medium.

1.2.1 Shocks in SNRs

Since SNRs contain multiple shock regions, understanding their dynamics involves delving into the shock physics. Shocks are thin transition layers (mathematically modeled as a discontinuity) of sudden variations in pressure, temperature, density and velocity. Hydrodynamic shocks occur whenever a gas moves through a medium at a velocity greater than the local sound speed:

$$c_s = \sqrt{\gamma \frac{p}{\rho}} \tag{1.1}$$

with p, ρ and γ being the upstream pressure, density and adiabatic index, respectively. A description of the basic physics behind shock dynamics can be found in Landau & Lifshitz (1959).

One needs to impose the conservation of mass, momentum and energy flux across the shock front. Typically in SNRs, the transition layers are much thinner than the curvature radii of the shocks, therefore in a first approximation they can be considered as plane parallel structures. In the reference frame of the shock, the hydrodynamic equation of conservation of mass, momentum and energy flux, also known as Rankine-Hugoniot jump conditions, can be written as:

$$\rho_2 v_2 = \rho_1 v_1 \tag{1.2}$$

$$p_2 + \rho_2 v_2^2 = p_1 + \rho_1 v_1^2 \tag{1.3}$$

$$v_2(p_2 + U_2 + \rho_2 v_2^2/2) = v_1(p_1 + U_1 + \rho_1 v_1^2/2) \tag{1.4}$$

where ρ, v, P and U are respectively the bulk velocity, density, pressure and density of internal energy of the gas, and the indexes 1 and 2 indicates the values in the pre-shock medium (also referred as upstream) and in the post-shock medium (also referred as downstream), respectively. For an ideal gas one can express the specific internal energy as

$$U = \frac{1}{\gamma - 1} p. \tag{1.5}$$

By inserting the Equation 1.2, Equation 1.3 and Equation 1.5 in Equation 1.4, one can solve

$$\chi = \frac{(\gamma + 1)\mathcal{M}}{(\gamma - 1)\mathcal{M} + 2}, \tag{1.6}$$

where the compression ratio across the shock is defined as $\chi \equiv \frac{\rho_2}{\rho_1} = \frac{v_1}{v_2}$ and the sonic Mach number is $\mathcal{M}^2 \equiv \frac{\rho_1 v_1^2}{\gamma p_1} = \frac{v_1^2}{c_s^2}$. By leveraging the ideal gas state equation and the Equation 1.3, and under the assumption $\mathcal{M} >> 1$, an expression for the downstream temperature can be derived:

$$kT_2 = \frac{1}{\chi}\left(1 - \frac{1}{\chi}\right)\mu_2 m_p v_1^2 \tag{1.7}$$

where μ_2 is the average downstream particle mass in units of the proton mass m_p.

In the physics of SNRs is frequent to encounter shocks with high Mach number ($\mathcal{M} >> 1$) and non-relativistic mono-atomic gasses, for which $\gamma = 5/3$. Therefore the Equation 1.2, 1.6 and 1.7 can be written as:

$$\chi = \frac{\gamma + 1}{\gamma - 1} = 4, \tag{1.8}$$

$$v_2 = \frac{1}{\chi} v_1 = \frac{1}{4} v_1, \tag{1.9}$$

$$kT_2 = \frac{3}{16}\mu_2 m_p v_1^2. \tag{1.10}$$

1.2.2 Evolution of SNRs

The evolution of a SNR hinges on the interaction between the primary shock and the surrounding medium, encompassing both the fossil ISM and the CSM shaped by the progenitor system, with its wind activity and mass loss history. Usually there can be identified four evolutionary phases in SNRs (e.g. Woltjer (1972)):

i. The *ejecta-dominated phase* where the ejecta mass still outweighs over the mass swept by the forward shock ($M_{ej} > M_{sw}$). This phase is sometimes referred to as the *free expansion phase*.

ii. The *energy-conservation* or *Sedov-Taylor phase* where the swept up mass surpasses the ejecta mass ($M_{ej} < M_{sw}$). This phase is also named adiabatic phase since during this phase the radiative losses are still considered negligible;

iii. The *pressure-driven* or *snow-plough phase* characterized by significant radiative losses. The shock wave evolution is dominated by the momentum conservation;

iv. The *merging phase* is reached when the shock velocity nears the local sound speed, gradually fading away and marking the end of the SNR.

It has to be noted that, the reality is far more intricate, as distinct regions within a single SNR might concurrently experience different evolutionary phases, adding layers of complexity to their overall evolution (e.g. RCW86, Vink et al. 2006; Yamaguchi et al. 2016).

Several analytical models were developed to describe the evolution of SNRs. The ejecta dominated phase can be approximated by the Chevalier (1982) model which is based on the assumption of a power-law density distribution of the outer ejecta. The Truelove & McKee (1999) model is the one which best approximates the transition from the ejecta dominated phase to the adiabatic phase.

The most used model for remnant which entered the energy conservation phase is the Sedov-Taylor self-similar solution (Taylor 1950; Sedov 1959). It assumes that the explosion energy E originates from a point source and is instantaneously injected into a uniform medium with uniform density ρ_0, and that no energy losses occur. The dynamics can be derived using a simple dimensional analysis. Assuming the shock radius as a function of energy, density and time ($R_s = \xi E^{\alpha} n^{\beta} t^{\gamma}$), the dimensional analysis gives

$$[L] = [ML^2t^{-2}]^{\alpha}[ML^{-3}]^{\beta}[t]^{\gamma}. \tag{1.11}$$

From Equation 1.11 it can be easily obtained $\alpha = -\beta = 1/5$ and $\gamma = 2/5$. So, the shock

radius R_s and velocity V_s will evolve as

$$R_s = \left(\xi \frac{E t^2}{\rho_0}\right)^{\frac{1}{5}}, \tag{1.12}$$

$$V_s = \frac{dR_s}{dt} = \frac{2}{5}\left(\xi \frac{E}{\rho_0}\right)^{\frac{1}{5}} t^{-\frac{3}{5}} = \frac{2}{5}\frac{R_s}{t}, \tag{1.13}$$

where ξ is a dimensionless constant depending on the adiabatic index, e.g. $\xi = 2.026$ for a mono-atomic gas. An analytic solution exists (Blandford & McKee 1976) also for a medium with a power-law density profile $\rho(r) \propto r^{-s}$. For such a density profile, the shock radius and the shock velocity depend on time like $R_s \propto t^{\beta}$, $V_s \propto \beta \frac{R_s}{t}$, with $\beta = 2/(5-s)$. An astrophysically case, relevant for this thesis, is s = 2, corresponding to a SNR shock moving through the progenitor's stellar wind, whose density profile scales as r^{-2} (for a steady wind).

1.2.3 Classification of SNRs

The evolution of SNRs and their interaction into the ambient medium yields a variety of potential morphologies. Indeed, SNRs are traditionally categorized into four distinct types based on the remnants' morphology: *Shell-type SNR, plerion* or *filled-center SNR*, *composite SNR* and *mixed-morphology SNR*. Examples for each class are shown in Figure 1.2. Shell-type SNRs exhibit a ring-like morphology, arising from the limb brightening of the spherical shell, as expected in a classical Sedov-Taylor evolution. Shell-type SNRs are the most common morphological class among SNRs and includes examples as Cassiopeia A, Kepler's SNR, the Cygnus Loop and SNR E0102-72.3 (see Figure 1.2, upper left panel).

Plerions, from the Greek word *"pleres"*, which stands for "full", are particularly bright in the central area while lacking shell-like emission. This morphology stems from the presence of a Pulsar Wind Nebula (PWN) formed by a rapidly rotating NS created in the core collapse (see Section 1.1). As spinning down, the NS releases energy a rate $\dot{E} = I\dot{\Omega}\Omega$ where I is the moment of inertia, Ω the angular frequency and $\dot{\Omega}$ its time derivative. This process generates a wind of ultra-relativistic electrons and positrons which advect and scatter in the magnetic field creating a nebula of relativistic particles emitting synchrotron and inverse Compton radiation. The nebula is surrounded by the ejecta (for a review on this subject the reader could also refer to Temim & Slane (2017)). However, the radio and X-ray emission from plerions are powered by the pulsar wind, not by the supernova explosion. The quintessential example for a center-filled SNR is the Crab Nebula (see Figure 1.2, upper right panel).

Composite SNRs are the second most common morphology class. Combining the previous definitions, they are shell-like remnants which also contain a PWN inside. This

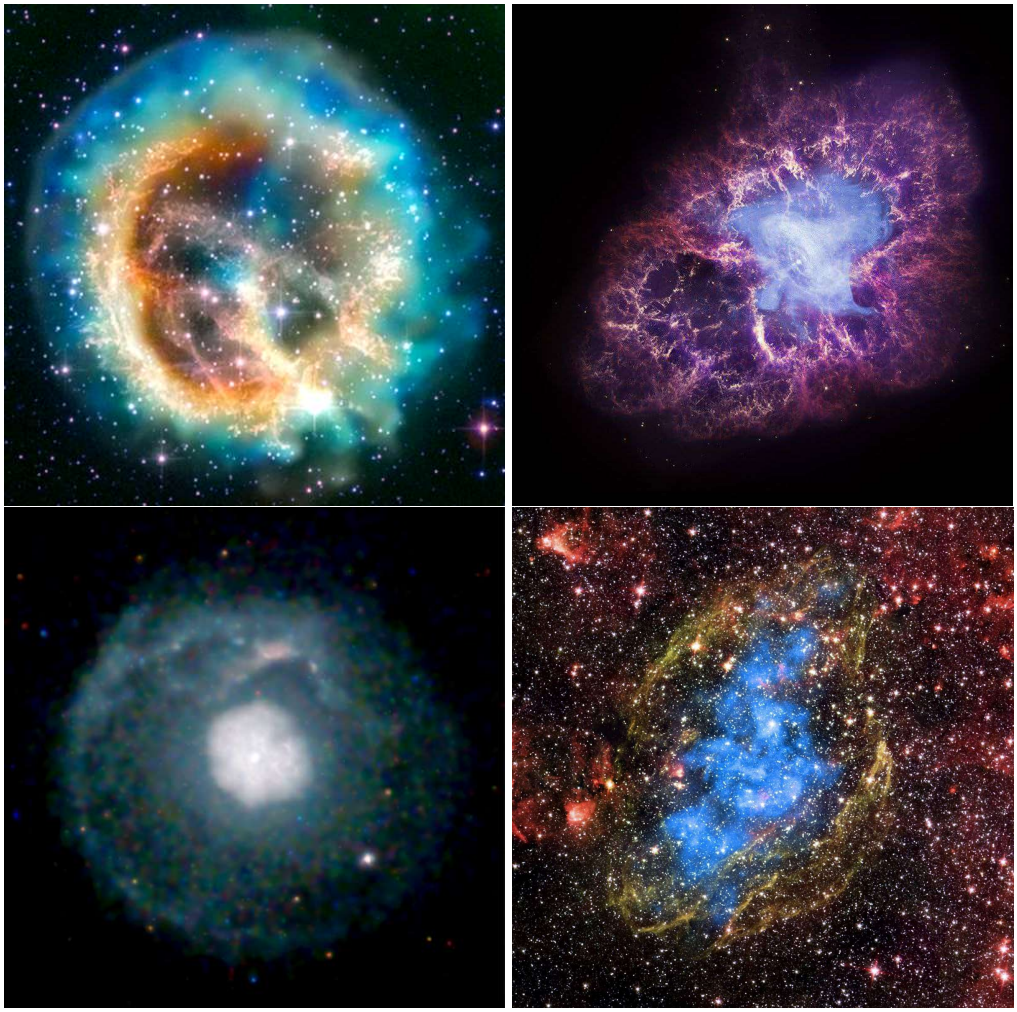

Figure 1.2: Examples of SNRs with different morphologies. *Upper left:* The shell-type SNR E0102-72.3 in the Large Magellanic Cloud (Credit: X-ray: NASA/CXC/MIT/D. Dewey & NASA/CXC/SAO/J. DePasquale; Optical: NASA/STScI). *Upper right:* The Crab Nebula, a plerion type remnant from the explosion of SN 1054 (Credit: X-ray: NASA/CXC/SAO; Optical: NASA/HST). *Lower left:* The composite SNR G21.5-0.9 observed by *Chandra* (Credit: Matheson & Safi-Harb 2005) *Lower right:* The mixed morphology SNR W44 (credit: X-ray: NASA/CXC/Univ. of Georgia/R.Shelton & NASA/CXC/GSFC/R.Petre; Infrared: NASA/JPL-Caltech).

classification includes remnants like Vela SNR, Kes 75 and G21.5-0.9 (see Figure 1.2, lower left panel; see also Slane et al. 2018; Temim et al. 2019; Matheson & Safi-Harb 2005).

The last category of SNRs, namely mixed morphology SNRs also known as thermal-

composite SNRs, shows a thermal X-ray emission from a hot plasma at the center and an external shell emitting in radio. In general, these SNRs are relatively old, and are associated with dense interstellar medium. Worth-noting examples are the Jellyfish Nebula (IC 443), W28, W49 B, and W44 (see Figure 1.2, lower right panel).

1.3 Thermal X-ray emission in SNRs

In Section 1.2 the application of the Rankine-Hugoniot jump condition reveals that the shock transition itself causes the conversion of incoming bulk kinetic energy into thermal energy, as indicated by the Equation 1.7 for the post-shock temperature. Since SNR shocks are characterized by low densities, typically $n \sim 1$ cm^{-3}, the mean free path for particle-particle interactions in the ambient medium greatly exceeds the size of the remnant itself. Indeed, the cross section for Coulomb interaction between charged particles is (Spitzer 2006)

$$\sigma_{Coul} \simeq 4\pi \frac{Z_1^2 Z_2^2 e^4}{v^4} \left(\frac{m_1 + m_2}{m_1 m_2} \right)^2, \tag{1.14}$$

and the corresponding collision time is $\tau_{Coul} = \dfrac{1}{n\sigma v} \propto v^3 \propto E^{\frac{3}{2}}$. Using the proton mass for m_1 and m_2 and considering a typical post-shock temperature of $kT = 0.1$ keV and density of $n = 0.1$ cm^{-1}, one obtain $\sigma_{Coul} \approx 10^{19}$ cm.

These value is comparable with the radii of young and middle aged SNRs and much larger than the shock front width, so the shock heating cannot be the results of particle-particle interactions. For this reason SNR shocks are commonly referred as *collisionless shock* (for a review on this topic see Treumann 2009). In such shocks the plasma heating occurs through interaction with plasma waves and electric fields in the shock transitions layers. Simulations by Bennett & Ellison (1995) show that the heating region in such shocks has a characteristic width of $\sim 10 - 100\ c/\omega_p$ (where ω_p is the plasma frequency), corresponding to a shock thickness $\Delta x = 10^7 n_e^{-1/2}$, which is 13 orders of magnitude smaller than the mean free path found with Coulomb collisions (also refer to Miceli 2023).

Once the plasma is heated to several million Kelvins, it emits thermal radiation predominantly in the X-ray band. The hot plasma in SNRs is typically optically thin, and its ionization distribution is often out of equilibrium. Thermal emission is usually characterized by the combination of continuum emission, including bremsstrahlung (free-free processes), radiative recombination continua (free-bound processes) and two-photons emission, and line emission from heavily ionized ion species excited by collisions with electrons (bound-bound processes).

1.3.1 Thermal continuum

Bremsstrahlung

Bremsstrahlung emission arises from the acceleration of electrons as they interact with ions. It is a free-free emission since it is due to a transition between two unbound states, resulting in the production of a continuum emission spectrum. The bremsstrahlung emissivity per unit frequency is given by the sum of the bremsstrahlung emissivity of all ion species in the plasma (e.g., Longair 2011; Vink 2020) and can be expressed as:

$$\epsilon_{ff}(\nu, T_e) = \frac{2^5 \pi e^6}{3 m_e c^3} \left(\frac{2\pi}{3 k m_e} \right)^{\frac{1}{2}} T_e^{-\frac{1}{2}} e^{-\frac{h\nu}{kT_e}} \times n_e \sum_i n_i Z_i^2 g_{ff}(Z_i, T_e) \text{ erg s}^{-1} \text{ cm}^{-3} \text{ Hz}^{-1}, \tag{1.15}$$

where $g_{ff} \approx 1$ is the Gaunt factor which depends on temperature, Z_i and n_i denote the atomic number and the ion density for the i-th species. By integrating the Equation 1.15 over all frequencies one obtains that the total emissivity is proportional to $\sqrt{T_e} n_e \sum_i n_i Z_i^2 g_{ff}(Z_i, T_e)$. This expression also illustrates the dependence of emissivity on $n_e \sum_i n_i Z_i^2$. Hence, the total radiation from a region of a given volume V is proportional to the emission measure (EM), defined as

$$\text{EM} = \int_V n_e \sum_i n_i Z_i^2 dV. \tag{1.16}$$

In a plasma characterized by solar, undersolar, or slightly oversolar abundances, the primary contribution to the bremsstrahlung emission originates from the Hydrogen ions and their stripped electrons, since H is by far the most abundant element. Therefore, assuming a uniform composition and density for an emitting plasma the EM is often approximated by EM= $n_e n_{\text{H}} V$.

Free-bound emission

Free-bound emission occurs when an ion captures an electron into an atomic shell and as a consequence a photon is emitted with energy $h\nu = E_e + \chi_n$, where E_e is the energy of the free electron and χ_n is the ionization potential of the shell n. The emissivity for free-bound emission due to an ion i', resulting in an ion i, is (Longair 2011)

$$\epsilon_{fb} = \sqrt{\frac{2}{\pi}} \frac{g_i}{g_{i'}} c \sigma_i(h\nu) \left(\frac{h\nu}{E_n} \right) \left(\frac{e_n^2}{m_e c^2 kT} \right)^{\frac{3}{2}} e^{-\frac{h\nu - E_n}{kT_e}} n_e n_{i'} \text{ erg s}^{-1} \text{ cm}^{-3} \text{ Hz}^{-1}, \tag{1.17}$$

where $h\nu \geq E_n$; $g_{i'}, g_i$ are the degeneration of the ion states before and after recombination and $\sigma(h\nu)$ is the photo-ionization cross section of the ion in its final state.

Two-photons emission

Two-photons emission arises from electrons that populate the 2s meta-stable state in hydrogen-like or helium-like ions. In these situations, since the decay from the meta-stable level to the ground state (1s level) is forbidden due to quantum selection rules, the electrons in the meta-stable level can be de-excited by emitting two photons. Although the total energy of the emitted photons corresponds to the energy gap between the meta-stable and ground levels, this process results in a continuum spectrum. Indeed, the individual photon's energy can vary within the interval from 0 to the energy gap, thus determining the continuum nature of the emitted radiation.

1.3.2 Line emission

In addition to the X-ray continuum emission, line emission stands as another crucial component within the spectra of SNRs. This line emission originates from the excitation of ions resulting from collisions between ions and thermal electrons. When ions become excited, they subsequently de-excite by emitting photons at an energy equal to the difference between the upper and lower ion energy states $h\nu = E_{exc} - E_l$. The emissivity of line emission for a particular transition of a z element from a j state to an i state is (Mewe 1999):

$$P_{ji} \propto A_z n_{\rm H} n_e F(T) \text{ photons cm}^{-3} \text{ s}^{-1}, \tag{1.18}$$

where A_z represents the abundance of the element z, and $F(T)$ denotes a function reflecting the temperature dependence due to the combined effects of ionization and excitation. In collisional ionization equilibrium, this function peaks at the characteristic line temperature. In the X-ray band, the line emission primarily arises from ions with minimal bound electrons such as hydrogen-like (H-like) and helium-like (He-like) ions which emit characteristic lines due to transitions between their energy levels. However, for elements like iron and nickel, line emission also emerges from ions with more than two electrons, particularly from electrons in the L-shell. This intricate arrangement results in closely clustered line emissions, forming what is known as the Fe-L complex within the 0.7-1.3 keV band.

Line broadening

With the introduction in the X-ray astronomy of high resolution spectrometers, it has become possible to resolve the different broadening effects (besides the instrumental one) to the line emission in SNRs. Indeed, line emission is usually affected by several physical and instrumental processes which broadens the line profile. This thesis will particularly delve into two physical effects: *Thermal Motion* Doppler Broadening and *Bulk Motion* Doppler Broadening.

In collisionless shocks, the ions in shock heated plasma are expected to exhibit a temperature which should follow Equation 1.10. Indeed, a mass proportional post shock temperature for ions has been observed in SNRs (Miceli et al. 2019; Miceli 2023; Raymond et al. 2017). Therefore the higher the temperature (and the mass) of the ions, the wider the distribution of velocities. This isotropic distribution of velocities corresponds to a Gaussian profile that effectively broadens the emission line. Therefore, assuming from Equation 1.10 that $T_i = AT_p$ (where A is the atomic mass of the i ion, and T_p is the protons temperature) the width of the resulting Gaussian line (σ_{th}) follow the expression:

$$\sigma_{th} = E\sqrt{\frac{kT_i}{m_i c^2}} = E\sqrt{\frac{kT_p}{m_p c^2}}, \tag{1.19}$$

where E is the energy of the emission line.

The second effect encompasses Doppler broadening arising from the plasma's bulk motion. When a photon is emitted by a moving source, it is affected by Doppler shift proportional to the projection of the velocity along the line-of-sight. Differential velocities across various parts of the emitting body lead to broadened spectral lines, with the line width directly correlated to the breadth of the velocity distribution.

1.3.3 Non Equilibrium Ionization

SNRs' plasma usually exhibits a state of non-equilibrium ionization (NEI) as the impulsive shock heating occurs on time-scales that are much shorter than those of the ionization and recombination processes. In an optically-thin plasma, the time evolution of the ionization fraction for a specific ionization state, F_i, is described by the equation

$$\frac{1}{n_e}\frac{dF_i}{dt} = \alpha_{i-1}(T)F_{i-1} - [\alpha_i(T) + R_{i-1}(T)]F_i + R_i(T)F_{i+1}, \tag{1.20}$$

where α_i and R_i stand for the ionization and recombination rate for a generic i state, respectively.

When the plasma reaches the condition of collisional ionization equilibrium (CIE), ionization and recombination processes balance each other and from Equation 1.20 one obtains $\frac{1}{n_e}\frac{dF_i}{dt} = 0$. The state of ionization scales with the so-called ionization age, which is defined as $\tau = \int n_e dt$ (derived from the Equation 1.20). A plasma approaching the CIE typically shows a value of τ of the order of 10^{12} s cm^{-3} (Smith & Hughes 2010). As a consequence, low density plasma, like those in SNRs ($n_e \sim 1$ cm^{-3}), reach the CIE conditions in the order of $t = 10^{12}$ s corresponding to $t \approx 3 \times 10^4$ yrs. This implies that young SNRs are usually in NEI condition, specifically they are *under-ionized*. Therefore, the highly ionized states at a given temperature are less populated than in CIE conditions.

The impact of NEI on spectra becomes evident when examining the ratio between H-like and He-like lines within a specific species. In fact, the ratio between He-like and H-like lines tends to be higher for under-ionized plasma with respect to that observed in CIE at identical temperatures.

Interestingly, a sample of mixed morphology SNRs shows opposite NEI conditions, characterized by the presence of overionized (i.e. recombining) plasma, which is strongly indicative of a rapid cooling. Different possibilities have been proposed to explain these particular conditions, namely adiabatic cooling (e.g., Miceli et al. 2010) and thermal conduction (e.g., Kawasaki et al. 2002), the two channels having different relative weights depending on the remnant evolutionary stage (for a review, see Yamaguchi 2020).

1.4 SNRs as particle accelerators

In a groundbreaking study, Hess (1912) found that the observed intensity of ionizing radiation consistently increases with altitude. This (at the time) unexpected rise in radiation levels strongly indicated an extraterrestrial source for the ionizing radiation, leading to the discovery of what are now called cosmic rays (CRs). The spectrum of CRs spans a vast range of energies, extending up to approximately 10^{20} eV, as depicted in Fig 1.3. Aside from the energy band influenced by solar wind properties (below 10^{11} eV), the spectrum exhibit a near power-law behavior described by the expression:

$$dN(E) \propto E^{-q} dE, \tag{1.21}$$

where the spectral index is $q = 2.7$ below 3×10^{15} eV, $q = 3.1$ up to 5×10^{18} eV, and again $q = 2.7$ thereafter. The steepening is usually referred to as the "knee" of the X-ray spectrum, while the flattening feature is usually named "ankle". The galactic influence in the CRs spectrum is commonly retained to be dominant up to the knee feature.

Baade & Zwicky (1934a) suggested that SNe explosions could be the source of CRs. Up to these days, it's generally accepted that the energy provided by the SN explosions can satisfy the production of CR up to energies of $10^{14} - 10^{15}$ eV. However, the actual acceleration mechanism is believed to occur over more extended time-scales, within SNR shocks. The primary argument favoring SNRs as the predominant source of CRs in our Galaxy centers around their energetics. To maintain the observed energy density of cosmic rays within our Galaxy, estimated at $U_{cr} \approx 1$ eV cm^{-3}, a power input of about $dE/dt \approx 1.2 \times 10^{41}$ erg s^{-1} is required (Hillas 2005). Considering the canonical kinetic energy output from SN explosions (around 10^{51} erg, as discussed in Section 1.1), and given a Galactic SN rate ranging between 2-3 supernovae per century, the kinetic power delivered is approximately $dE/dt \approx 1 \times 10^{42}$ erg s^{-1}. This indicates that SNe possess the necessary energy reservoir to fuel cosmic rays in our Galaxy, provided that SNR are capable of effectively transferring approximately $\sim 10\%$ of their energy output to the production of cosmic rays.

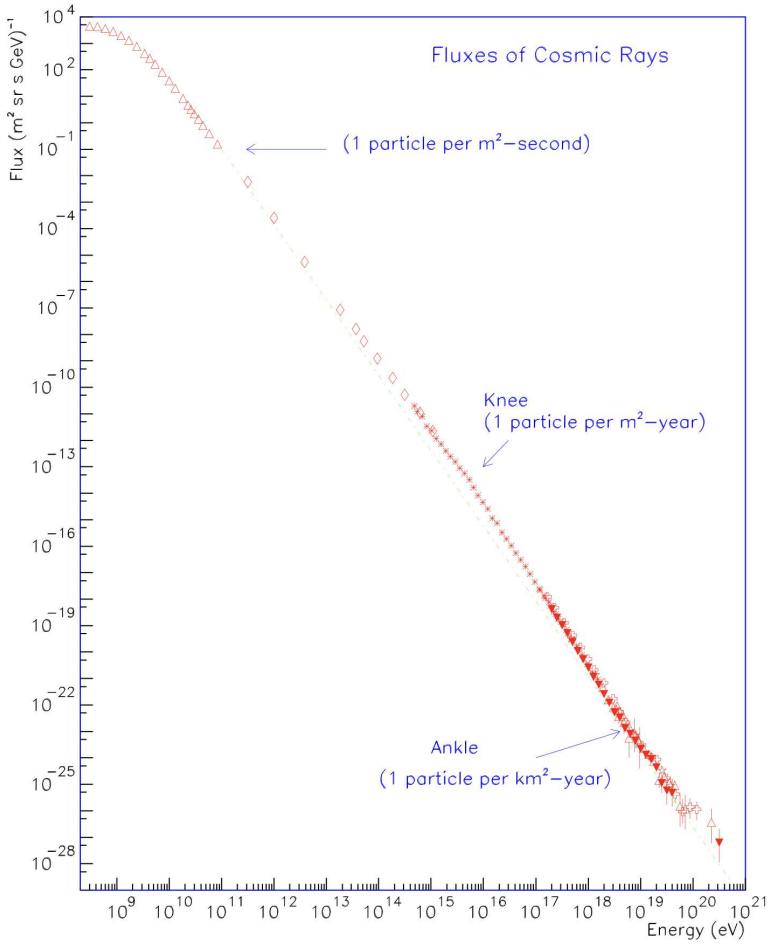

Figure 1.3: The CR spectrum, with its two features, the “knee” and the “ankle” (Credit: Olinto 2001, compilation by S. P. Swordy).

1.4.1 Diffusive Shock Acceleration

The primary mechanism behind the acceleration of CRs through collisionless shocks is the first order Fermi acceleration, usually referred to as the diffusive shock acceleration (DSA). This theory was developed by several independent scientists between 1977 and 1978 (Axford et al. 1977; Bell 1978a,b; Blandford & Ostriker 1978). DSA operates on the concept that charged particles within the shock-heated plasma have the opportunity to recross the shock front, moving from the downstream to the upstream medium, as they scatter around because of turbulence in the magnetic field. Once in the upstream region, they continue to scatter until they are again overtaken by the shock, thus initiating a cyclic process of acceleration (for a representative illustration refer to Figure 1.4). The energy gain associated with one complete acceleration cycle, from downstream to upstream and

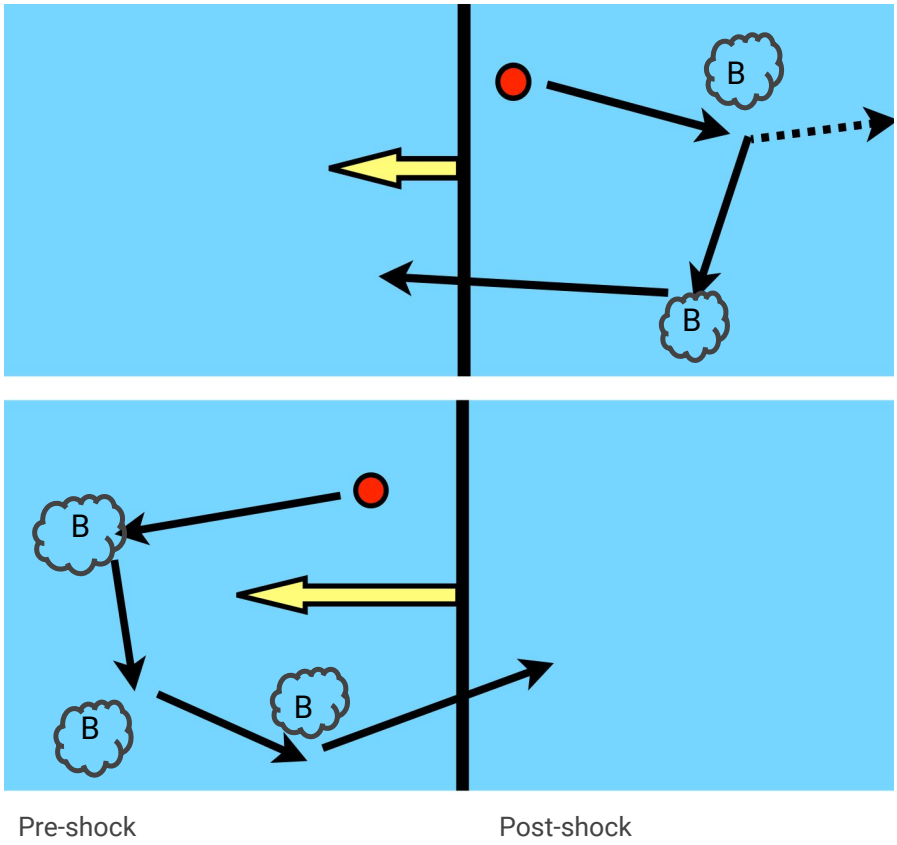

Figure 1.4: Representative sketch of an acceleration cycle according to the DSA theory in the shock rest frame.

back, can be approximated by the expression:

$$\left\langle \frac{\Delta E}{E} \right\rangle \approx \frac{4}{3} \frac{V_{sh}}{c}, \tag{1.22}$$

where V_{sh} is the shock velocity.

Throughout each cycle, particles face a finite chance of never re-crossing the shock due to the downstream movement of the shocked plasma, thus being advected in the downstream medium. Accounting for the probability of a particle to accelerate for at least N cycles, the energy distribution of the particles aligns to a power-law distribution (See Equation 1.21) with $q = \frac{\chi+2}{\chi-1}$, which for high Mach number shock gives $q = 2$ (see Equation 1.8). While the Galactic CR spectral index is measured at $q = 2.7$ (see Figure 1.3), the source spectrum is expected to be around $q \approx 2.2$ due to energy-dependent diffusion. The proximity of the predicted power-law index of $q = 2$ to the observed CR power-law at the source provides substantial support to the validity of the DSA theory.

To achieve the right spectral index at the source, one has to take in account non-linear DSA theories, which will not be discussed here (for further information about nonlinear DSA see Eichler 1979; Ellison & Eichler 1984).

It must be pointed out that while the CR spectral index does not depend on the shock velocity (provided that $\mathcal{M} >> 1$), the acceleration time scale exhibits a notable dependence on the shock velocity. Indeed the acceleration time is given by (Malkov & Drury 2001)

$$\tau_{acc} \approx 1014 \frac{\eta}{\delta Z} \left(\frac{E_{max}}{10^{14}\ \mathrm{eV}} \right) \left(\frac{V_{sh}}{5000\ \mathrm{km\ s^{-1}}} \right)^{-2} \left(\frac{B}{10\ \mu\mathrm{G}} \right)^{-1} \mathrm{yr}. \tag{1.23}$$

In this equation δ is a parameter which accounts for the energy dependence of the diffusion coefficient (it is strictly less than 1 and typically ranges between 0.3 and 0.7), η is the Bohm diffusing factor, i.e. the ratio between the diffusion coefficient and $c\lambda/3$ (where λ is the Larmor radius, the minimum value $\eta = 1$ corresponding to the Bohm limit) and E_{max} is the cutoff energy synchrotron emitting electrons. Shocks of young SNRs are capable to accelerate particles up to energies of 10^{14} eV provided that the shock velocity remains high for at least 1000 yr. The Bohm factor is closely linked to the turbulence of the magnetic field, which scatters charged particles. Specifically, the turbulence generated by the interaction between the shock and the surrounding medium amplifies the magnetic field through turbulent dynamo action (see Balsara et al. 2001 and Giacalone & Jokipii 2007), resulting in a reduction of the electron's mean free path and facilitating their acceleration.

The presence of turbulent magnetic fields in SNRs is testified by several observational indications, such as the low radio (e.g. DeLaney et al. 2002) and X-ray (e.g. Vink et al. 2022) polarization fraction. It has also been observed a correlation between an enhanced electrons acceleration and a dense ISM (which generate turbulences) in the SNR RX J1713.7-3946 (Inoue et al. 2012; Sano et al. 2015) and in some regions of RCW 86 (Suzuki et al. 2022). At the same time, lower levels of magnetic turbulence (larger polarization fractions) were observed in remnants evolving in a more uniform environment (namely SN 1006, Zhou et al. 2023), thus showing the important role played by the ambient medium in this context.

1.5 Non-Thermal X-ray emission in SNRs

Relativistic electrons, accelerated at the shock front, and moving in a magnetic field, emit synchrotron radiation. Synchrotron radiation from ultrarelativistic electrons can be detected up to the hard X-ray band. The first unambiguous detection of non-thermal X-ray emission in a SNR, discovered in SN 1006, goes back to Koyama et al. (1995).

Due to this accelerated motion, the particle radiates a total power of

$$\left(\frac{dE}{dt}\right)_{syn} = \frac{4}{3}\sigma_T c\beta^2\gamma^2 U_B, \tag{1.24}$$

with σ_T being the Thomson cross section, $\beta = v/c$, γ is the Lorentz factor and $U_B = B^2/8\pi$, represents the magnetic field's energy density.

For an electron with energy E (expressed as E_{100} in units of 100 TeV), the synchrotron emission reaches a sharp peak at a frequency ν, given by the relation (Ginzburg & Syrovatskii 1965)

$$h\nu = 13.9 B_{\perp 100} E_{100}^2 \text{ keV}, \tag{1.25}$$

where $B_{\perp 100} \approx \sqrt{2/3} B_{100}$ is the magnetic field component perpendicular to the electron's motion, in units of 100 μG.

As outlined in Section 1.4, the synchrotron radiation from SNRs arises from a population of relativistic electrons with a distribution of energy which follows a power-law (see Equation 1.21). This electron population in turn, generates a radiation spectrum exhibiting a power-law distribution in frequency $\epsilon_{syn}(\nu) \propto \nu^{-\alpha}$, characterized by a spectral index $\alpha = \frac{q-1}{2}$, where q represents the electron distribution's spectral index. In the X-ray band, it is more common to express the luminosity density as a unit of photons per seconds per energy, with an associated photon spectral index of $\Gamma = \alpha + 1 = \frac{q+1}{2}$.

It is essential to note that non-thermal emission spectra usually are observed to present a cutoff at high energy (usually at X-ray energies), which mirrors a cutoff in the electron energy spectra. The physical cause behind this cutoff remains not completely clear (Reynolds 2008). Various scenarios can be invoked to explain the cutoff in the spectrum, such as: the *age-limited* scenario and the *loss-limited* scenario. In the age-limited case, the highest energy (E_{age}) achievable by electrons depends on the duration of the acceleration process, which is constrained by the remnant's age (especially for young SNRs). This energy can be approximated by

$$E_{age} \approx 1.25 \left(\frac{B}{100\mu\text{G}}\right)^{-2} \left(\frac{t_{age}}{1000\text{yrs}}\right)^{-1} \text{TeV}. \tag{1.26}$$

This scenario introduces a high-energy exponential cutoff to the power-law distribution described in Equation 1.21 (Reynolds 1998):

$$N(E) \propto E^{-q} e^{-\frac{E}{E_{cut}}} \tag{1.27}$$

When the acceleration time scale (shown in Equation 1.23) becomes comparable with the radiative losses time scale, the maximum attainable energy for an electron will then be constrained by radiative losses, leading to the loss-limited scenario. Electrons, indeed, lose energy through radiative losses at a rate equivalent to the total power radiated

by synchrotron radiation, already expressed in Equation 1.24. Leveraging this equation, one could estimate the time scale for the radiative losses as:

$$\tau_{syn} \equiv \left| \frac{E}{dE/dt} \right| \approx \frac{634}{B^2 E} \text{ s } \approx 12.5 \left(\frac{E}{100\text{TeV}} \right)^{-1} \left(\frac{B}{100\mu\text{G}} \right)^{-2} \text{yr.} \tag{1.28}$$

This loss time, when expressed in terms of the observed photon energy (using Equation 1.25) can be approximated as:

$$\tau_{syn} \approx 55 \left(\frac{h\nu}{1\text{keV}} \right)^{-1/2} \left(\frac{B}{100\mu\text{G}} \right)^{-3/2} \text{yr.} \tag{1.29}$$

Zirakashvili & Aharonian (2007) derived analytically the X-ray spectrum for synchrotron radiation originating from shock-accelerated electrons in a loss-limited scenario, described by:

$$\frac{dN_X}{d\varepsilon} \propto \left(\frac{\varepsilon}{\varepsilon_0} \right)^{-2} \left[1 + 0.38 \sqrt{\frac{\varepsilon}{\varepsilon_0}} \right]^{\frac{11}{4}} \exp\left(- \sqrt{\frac{\varepsilon}{\varepsilon_0}} \right), \tag{1.30}$$

where ε and ε_0 denote respectively the photon energy and the cutoff energy parameter.

1.6 γ-ray emission in SNRs

The current generation of space and ground observatories covering energy bands from GeV to TeV (e.g. Fermi LAT, H.E.S.S., MAGIC, and VERITAS) has enabled the detection of γ-ray emissions from a rapidly increasing number of SNRs (e.g. Acero et al. 2016; Collaboration 2018). The emission in the $\gamma-$ray band is a crucial element to understand the physics behind the acceleration of CRs in SNRs. Indeed, it arises from interactions between high-energy particles, either accelerated electrons or protons, and matter or radiation fields within the remnant. There are primarily two mechanisms behind γ-ray emission in SNRs: the inverse Compton (IC) scattering, arising from the leptonic part of the accelerated particles, and Pion decay, resulting from the hadronic component of the spectrum.

While Compton scattering involves a photon transferring energy to lower-energy electrons, IC scattering consists in the reverse process, i.e. a high-energy electron transferring energy to a low-energy photon. The loss of power for a single electron can be given by (Longair 2011)

$$\left(\frac{dE}{dt} \right)_{IC} = \frac{4}{3} \sigma_T c \beta^2 \gamma^2 U_{rad}, \tag{1.31}$$

where U_{rad} is the energy density of the radiation field. Looking back to Equation 1.24 one can easily note the similarities with the IC equation. Nonetheless, instead

of a variation based on the magnetic field energy density (Equation 1.24) the radiated power for the IC scattering relies on the incident photons energy density field. The background photon spectrum (which is upscattered by the electrons) typically comprises a combination of the cosmic microwave background (CMB), near infrared (NIR) and far infrared (FIR) photons emitted by the dust produced in the cold (unshocked) ejecta, and for some sources, the synchrotron emission produced by the same electron population. Electrons with energies of the order of TeV can boost a photon up to γ-ray energies (10^{13} – 10^{14} eV).

Next to the IC scattering, Pion decay is one of the most important γ-ray continuum radiation mechanisms. This process arises from the collisions of hadronic cosmic rays, i.e. atomic nuclei and cosmic-ray protons, with atomic nuclei in the local gas. Indeed, in the interaction of a pair of hadrons (typically an accelerated proton colliding with a target proton) produces a neutral pion (π^0) following:

$$p^+ + p^+ \rightarrow p^+ + p^+ + \pi^0. \tag{1.32}$$

The produced π^0, with rest mass of 140 MeV/c^2, subsequently decay in 2 γ-ray photons. These photons each carry an energy of $m_{\pi^0}c^2/2$ in the pion's rest frame. However, the pion usually possesses excess kinetic energy in the observer's frame, especially when originating from a high-energy cosmic-ray proton. The resulting spectrum manifests itself with a characteristic shape, usually referred as *pion bump* (but see discussion in Sect. 2.5 of Gabici et al. 2019).

1.7 Thesis Outline

This thesis is dedicated to unraveling the intricate dynamics of SNRs, shedding light on the interplay between SN explosions, CSM, and the mechanisms steering particle acceleration. Through a meticulous analysis of X-ray observations and the synthesis of X-ray spectra via 3-D MHD models, the study aims to characterize the physical and chemical properties of SNRs. The integration of radio and γ-ray emission data further enhances the depth of understanding. The thesis focuses on three key challenges in this research field, preceded by Chapter 2, where I provide insights on the telescopes used to carry out the analysis. Each chapter delves into specific facets of the complex relationships between SN explosions, CSM, and the resulting evolution of SNRs. I here give the structure and a brief summary of the content of the different chapters.

In Chapter 3 I investigate the non-thermal emission in the external shell of the young Kepler's SNR, by conducting a spatially resolved spectral analysis of *NuSTAR* and *XMM-Newton* observations. Employing the model of synchrotron radiation in the loss-limited regime (see Section 1.5, Equation 1.30), I constrain the cutoff energy dependence of synchrotron radiation on the shock velocity. This analysis reveals two distinct regimes of particle acceleration characterized by differing Bohm factors: In the north, where the

shock interacts with a dense CSM, I observe a more efficient acceleration process (lower Bohm factors) compared to the southern areas, where the shock velocity is high and there is no sign of interaction with dense CSM. Combining hard X-ray spectra with radio and $\gamma-$ray observations, I construct a spectral energy distribution. My results suggest that the observed $\gamma-$ray emission predominantly originates from the northern part of the shell, potentially indicating a mainly hadronic origin.

In Chapter 4, I further investigate the case of Kepler's SNR. I study the temporal evolution of synchrotron flux using two deep *Chandra* X-ray observations performed in 2006 and 2014. Analyzing spectra from different filaments and measuring their proper motion, I estimate the ratio between acceleration and synchrotron cooling times (see Section 1.4 and 1.5). With this approach, I find a region in the northern part of the shell exhibiting a very low shock velocity. In this region, I measure an acceleration time-scale that is significantly longer than the synchrotron cooling time and I report a notable decrease in flux from 2006 to 2014. This result marks the first evidence of fading synchrotron emission in Kepler's SNR.

In Chapter 5, I analyze an *XMM-Newton* observation focused on a bright clump in the Vela SNR. This region lies along the axis connecting two ejecta knots known as shrapnel A and G, namely behind shrapnel G. Shrapnel A and G are the only two Si-rich ejecta knots identified in the Vela SNR so far (Katsuda & Tsunemi 2006; García et al. 2017). These two shrapnel are positioned in opposite directions with respect to the SNR center, hinting at a Si-rich jet-counterjet structure, which may look somehow similar to that observed in Cassiopeia A SNR. I investigate this clump's physical and chemical properties to discern its association with the hypothesized jet-like structure. My analysis unveils the presence of two distinct structures with differing characteristics. The first structure, elongated along the shrapnel A-G axis, has properties which closely align with those of shrapnel A and G. The second structure, running southeast-northwest, and characterized by a higher temperature, resemble a thin filament. Further analysis of ROSAT data reveals this filament's integration into a substantial, coherent structure along the western rim of the shell. This large-scale, coherent feature runs perpendicular to the jet-like structure, and is possibly the aftermath of the progenitor star's stellar wind. Its chemical properties hints at a possible Wolf-Rayet progenitor for Vela SNR.

In Chapter 6, by leveraging a state-of-the-art MHD simulation, comprehensively describing the evolution from SN 1987A to its remnant, I synthesized the spectrum as predicted to be observed with XRISM-Resolve, the new high-resolution spectrometer's on board of the newly launched XRISM satellite (See Section 2.5). My objective is to evaluate XRISM-Resolve's efficacy in identifying signatures of shocked ejecta within SN 1987A, since recent studies suggest the emergence of the ejecta component in the X-ray emission in the coming years. My projections for the 2024 (corresponding the allocated observation during performance verification phase) distinctly highlight the pivotal role of shocked ejecta in shaping the emission line profiles. The Doppler broadening stemming

from the bulk motion along the line of sight of the rapidly expanding ejecta significantly increases line widths beyond observed values. A quantitative comparison between my synthetic spectra and the actual XRISM spectra will facilitate establishing a robust correlation between the broadened line emission and freshly shocked ejecta.

In Chapter 7 I draw my final thoughts and conclusions, adding future prospects for my research activities.

2

X-ray Telescopes

X-ray telescopes well-suit the study of SNRs as explained in Section 1.3 and Section 1.5. In fact, this thesis is mainly focused on the analysis and on the synthesis of data from several X-ray telescopes for the study of the shocked structures in SNRs.

Contrary to what one may think, X-ray telescopes greatly differ from the classical optical telescopes. As a matter of fact, to focus X-rays for astronomical purposes is not an easy task. Since our atmosphere is opaque to X-rays, this kind of telescopes need to be space-borne, i.e. mounted on rockets, on artificial satellites or on stratospheric balloons. The second issue in the design of an X-ray telescope is that, usual parabolic mirror cannot focus X-rays due to the high penetration propriety of high energy photons. X-rays that strike mirrors nearly perpendicular to the mirror surface are either transmitted or absorbed, not reflected. So X-ray telescopes must have grazing incidence mirrors as optics, i.e. mirrors that reflect X-rays impacting at low angles ($\theta \sim 1°$), typically nested to maximize the collecting area. The most commonly used architecture for the design of the focusing mirrors is the Wolter Type I (briefly Wolter-I; Wolter 1952) since it has the simplest mechanical configuration. This configuration is a combination of paraboloid and hyperboloid mirrors as shown in Figure 2.1.

In this chapter I will review all the telescopes used in this work of thesis. In particular: in Section 2.1 I will describe the *ROSAT* telescope; Section 2.2 will be dedicated to *XMM-Newton*; Section 2.3 delves into the characteristics of the *Chandra X-ray Observatory*; In Section 2.4 I will explore the features of *NuSTAR* telescope; Finally, Section 2.5 will be dedicated to briefly describe XRISM and its high-resolution spectrometer Resolve.

2.1 *ROSAT*

The *ROSAT* mission, which is a short name for *RO*entgen *SAT*ellite, was a collaborative mission funded by Germany, the United States, and the United Kingdom. Launched on June 1, 1990, aboard a *Delta II* rocket, its primary objective was the completion of an exhaustive eighteen-month all-sky survey known as the *ROSAT* All Sky Survey (RASS). Following the conclusion of its main mission, *ROSAT* continued to explore the Universe in X-rays for over eight years before its final shutdown on February 12^{th}, 1999.

The focusing mirrors are designed with four nested grazing incidence Wolter-I mirrors, boasting a maximum aperture of 83.5 cm and a focal length of 240 cm. These mirrors were meticulously coated with a thin layer of gold to optimize X-ray reflectivity and operated at typical grazing angles between 1° and 2°.

The focal plane instrumentation comprised two identical *Position Sensitive Proportional Counters* (PSPC-B and PSPC-C) along with a *High Resolution Imager* (HRI) placed on a rotating platform, which enabled the positioning of each detector on the focal plane. The PSPCs functioned as multiwire proportional counters, offering an energy resolution of $\Delta E/E = 0.43\sqrt{0.93\text{keV}/E}$ and a spatial resolution of approximately 25 arcsec at 1 keV across a 2° diameter Field of View (FoV).

Initially, PSPC-C was designated as the primary detector until its failure on January 25, 1991, following which the reserved PSPC-B detector took over. Each PSPC essentially consisted of two separate counters: an anode with two cathodes for position sensing, sensitive to X-rays, and an anode serving as the anti-coincidence counter for background rejection. These electrodes were wire grids bonded onto a ceramic support frame. Guard wires with increasing diameters at the edges of the anode grids were implemented to reduce the electric field. Contained within a gas-filled counter composed of a mixture of 65% argon, 20% xenon, and 15% methane, these anode and cathode grids facilitated X-ray absorption. When an X-ray photon passed through the thin plastic entrance window, it underwent photoelectric absorption within the counter gas, generating a primary electron. This primary electron caused ionization of other gas atoms, creating a secondary electron cloud proportional to the energy of the incident X-ray photon. More information about *ROSAT* can be found in the *ROSAT* User's Handbook[1].

2.2 *XMM-Newton*

The X-ray Multi-mirror Mission (*XMM-Newton*) is the current European Space Agency's (ESA) X-ray observatory. Launched via an Ariane 5 ESA space rocket on December 10, 1999, it was placed in a High Elliptical Orbit (HEO) with a nearly 48-hour revolution period. *XMM-Newton* houses three X-ray telescopes each incorporating 58 grazing

[1] https://heasarc.gsfc.nasa.gov/docs/rosat/ruh/handbook/handbook.html

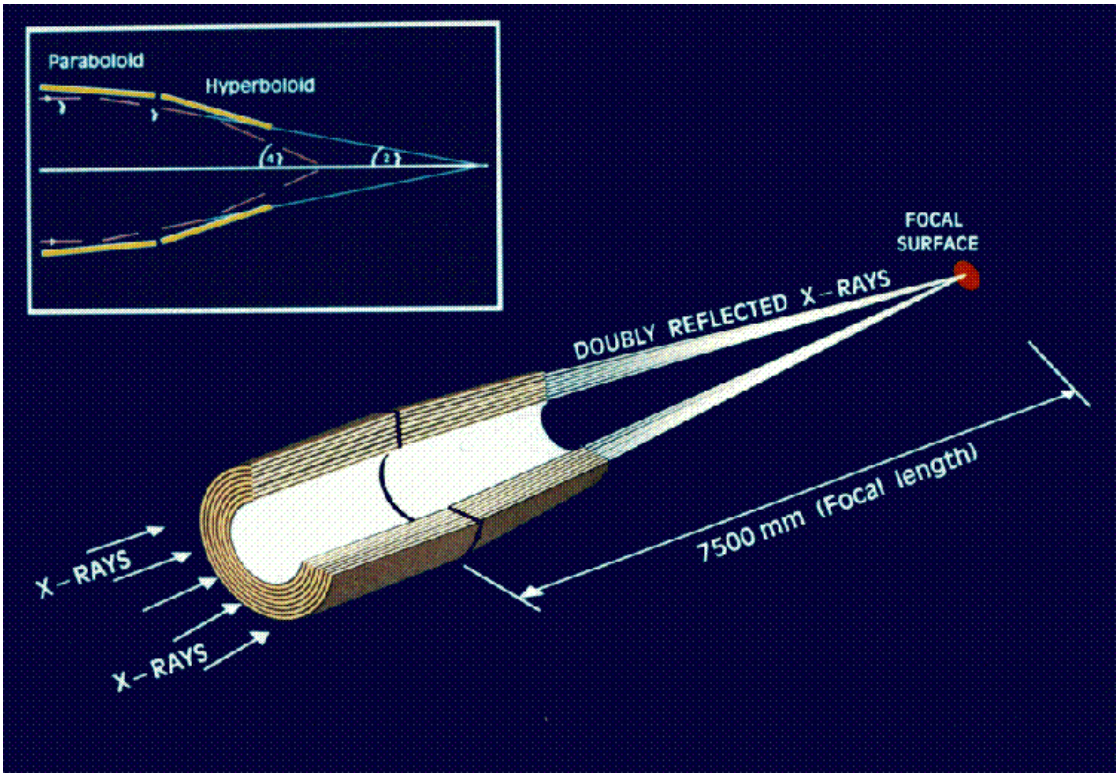

Figure 2.1: *XMM-Newton* example of the schematic of a Wolter type I configuration. (Credit: "*XMM-Newton* User's handbook", Issue 2.21, 2023; ESA: XMM-Newton SOC).

incidence mirrors nested in a coaxial and cofocal Wolter-I configuration (refer to Figure 2.1 for the mirror configuration). These mirrors operate at a grazing angle of 30'. The telescopes possess a focal length of 7.5 m and a diameter of 0.7 m.

The instrumentation aboard *XMM-Newton* includes the *European Photon Imaging Camera* (EPIC), comprising three X-ray CCD cameras, two *Reflection Grating Spectrometers* (RGS) for X-ray high-resolution spectroscopy of point-like sources within the $0.3 - 2.1$ keV energy band, and an *Optical Monitor* (OM), namely an optical telescope with a 30 cm diameter.

Through this section I will focus on the EPIC cameras, since I only use them in this work of thesis. EPIC cameras offer the possibility to perform sensitive imaging observations over the telescopes' FoV of 30 arcmin with a Point Spread Function (PSF) of $\sim 5''$ (full width half maximum), in the energy range $0.15 - 15$ keV with a spectral resolution $\Delta E/E \sim 0.02-0.05$. The EPIC's effective area (refer to Figure 2.2), calculated by multiplying the geometric area by the mirror reflection efficiency and the detector

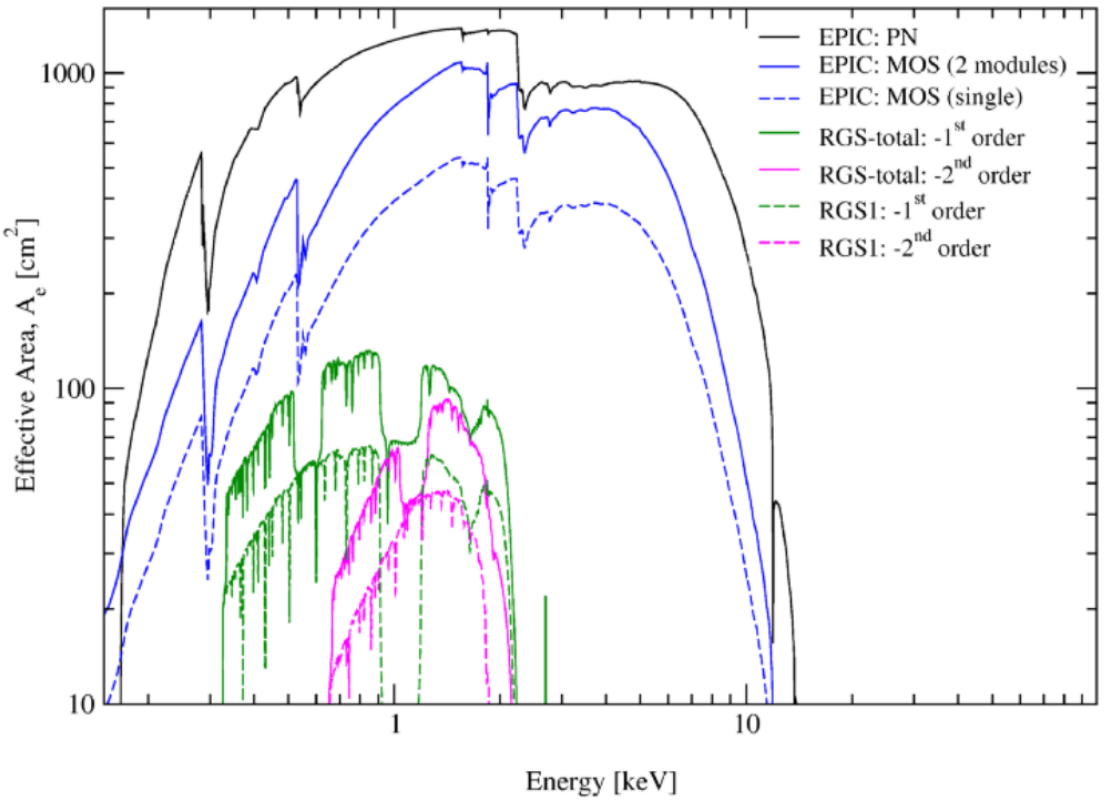

Figure 2.2: Net effective area for all the instrument on board *XMM-Newton* in logarithmic scale. (Credit: "*XMM-Newton* User's handbook", Issue 2.21, 2023; ESA: XMM-Newton SOC).

quantum efficiency, stands as one of the highest achieved for an X-ray telescope, with a peak at over 1000 cm^2 at 1.5 keV. Energy-dependent vignetting reduces the effective area off-axis, with a decrease larger than a factor of two at the borders of the FOV. Two of the EPICs within *XMM-Newton* utilize Metal-Oxide Semiconductor (MOS) CCDs installed at the focal planes where also the gratings of the RGS spectrometers are equipped. These gratings divert approximately half of the incident flux, resulting in only 44% of the original incoming flux reaching the MOS cameras. The third telescope, on the other hand, hosts a single instrument at its focal plane known as EPIC pn. Each MOS camera incorporates seven CCDs, all front illuminated, implying that X-rays impact the detector side where the electrodes are situated. These MOS cameras exhibit a quantum efficiency higher than 10% in the 0.3 – 10 keV energy band, with an imaging section comprising 600x600 pixels. Each pixel, measuring 40 µm square, covers a span of 1.1x1.1 arcsec within the FoV. On the other hand, the pn-CCDs in EPIC pn are back illuminated. The

pn camera consists of twelve 3x1 cm pn CCDs, each with 200x64 pixels, resulting in a pixel size of 150x150 µm.

The EPIC cameras exhibit various modes of data acquisition. For the investigation of extended sources such as SNRs, the optimal pn setting is the Extended Full Frame (EFF), as it necessitates the largest available FoV for spatially resolving the object. Similarly, the most suitable MOS setting is the Full Frame (FF) mode. Given that the EPIC detectors aren't solely sensitive to X-rays but also to infrared (IR), visible, and ultraviolet (UV) photons, aluminized optical blocking filters are integrated into the cameras. These filters serve to diminish the contamination of the X-ray signal by these other photon types. Each EPIC camera comprises four filters: thin, medium, thick, and closed. The first three are chosen based on the flux of the sources in the FOV, while the last is used to protect the CCDs from soft protons in specific parts of the orbit. All the information about *XMM-Newton* can be found in the *XMM-Newton* Users' Handbook[2].

2.3 *Chandra X-ray Observatory*

The *Chandra X-ray Observatory* (CXO), often referred as *Chandra*, is the National Aeronautics and Space Administration's (NASA's) prominent X-ray space telescope, launched into space aboard the Space Shuttle Columbia during STS-93 on July 23, 1999. It orbits in a HEO, with an apogee of 134000 km and a perigee of 14000 km.

Chandra combines an efficient high-resolution imaging X-ray telescope with a suite of different spectroscopic instruments. The design of its focusing mirrors comprises a set of four nested paraboloid-hyperboloid grazing-incidence X-ray mirrors, with the largest mirror boasting a diameter of 1.2 meters, a focal length reaching 10 meters, and an impressive PSF of less than 0.5 arcsec.

The Science Instrument Module (SIM), responsible for adjusting the telescope's focal length and positioning instruments orthogonal to the optical axis, houses the observatory's two focal instruments: the Advanced CCD Imaging Spectrometer (ACIS) and the High-Resolution Camera (HRC). In this context, the thesis will delve into the description of the ACIS instrument, which stands as the sole instrument utilized. The ACIS consists of two distinct CCD arrays: the ACIS-I, a 4-chip square array, and the ACIS-S, a 6-chip linear array. The former excels in imaging, leveraging the entire FoV of 16 arcmin, while the latter is better suited for dispersed spectra when a grating is posed in the optical axis. These cameras offer exceptional spatial resolution ($\approx$ 0.492 arcsec) and moderate spectral resolution ($E/\Delta E \approx 20-50$ at $1-6$ keV) within a broad energy band spanning from 0.5 to 8 keV. However, during the years the efficiency of the ACIS cameras at energies below 1 keV has been compromised due to molecular

[2] http://xmm-tools.cosmos.esa.int/external/xmm_user_support/documentation/uhb/XMM_UHB.pdf

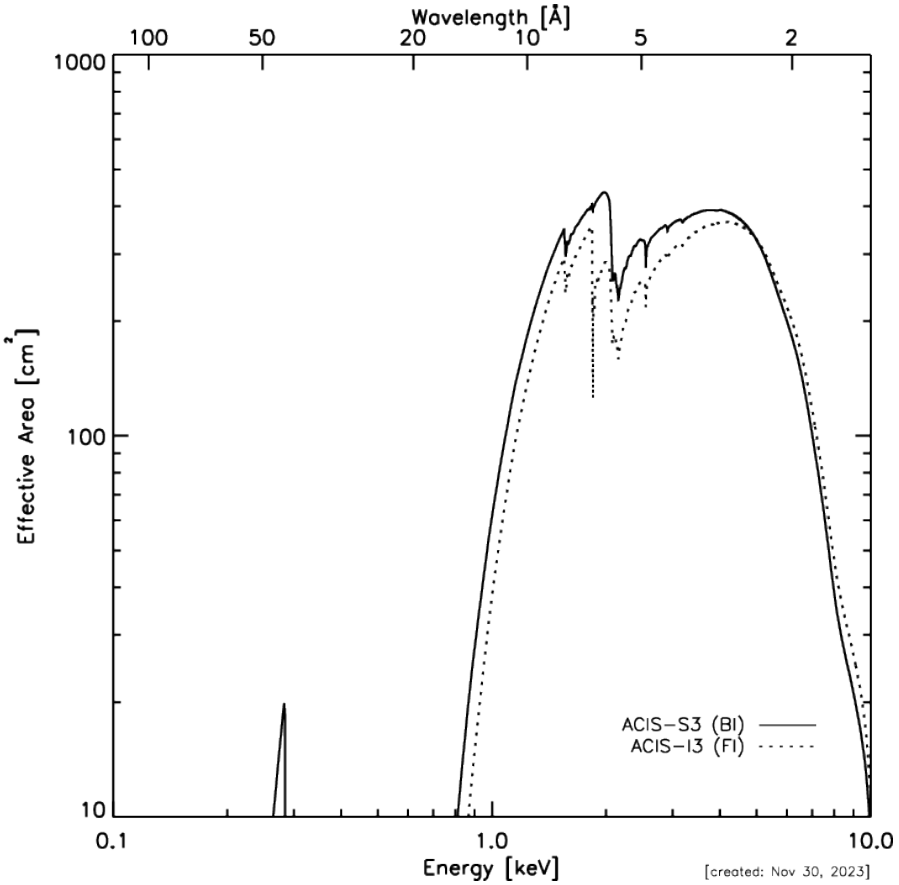

Figure 2.3: ACIS Effective area as a function of energy as it is expected to be in the 2024. Dashed line marks the third CCD for the I array and the solid line the third CCD for the S array. (Credit: Chandra Proposers' Observatory Guide)

contamination on the optical blocking filter. As a result, after 25 years of activities, as illustrated in Figure 2.3, the current effective area for the ACIS arrays below 1 keV is negligible. All the details illustrated here about CXO can be found at the Chandra Proposers' Observatory Guide[3].

2.4 *NuSTAR*

The Nuclear Spectroscopic Telescope Array (*NuSTAR*) was launched on June 13, 2012 on a Pegasus XL vehicle under the lead of Caltech institute. *NuSTAR* is capable to focus high energy X-rays (3 – 79 keV). It operates in a Low Earth Orbit (LEO) with an altitute

[3] https://cxc.harvard.edu/proposer/POG/html/index.html

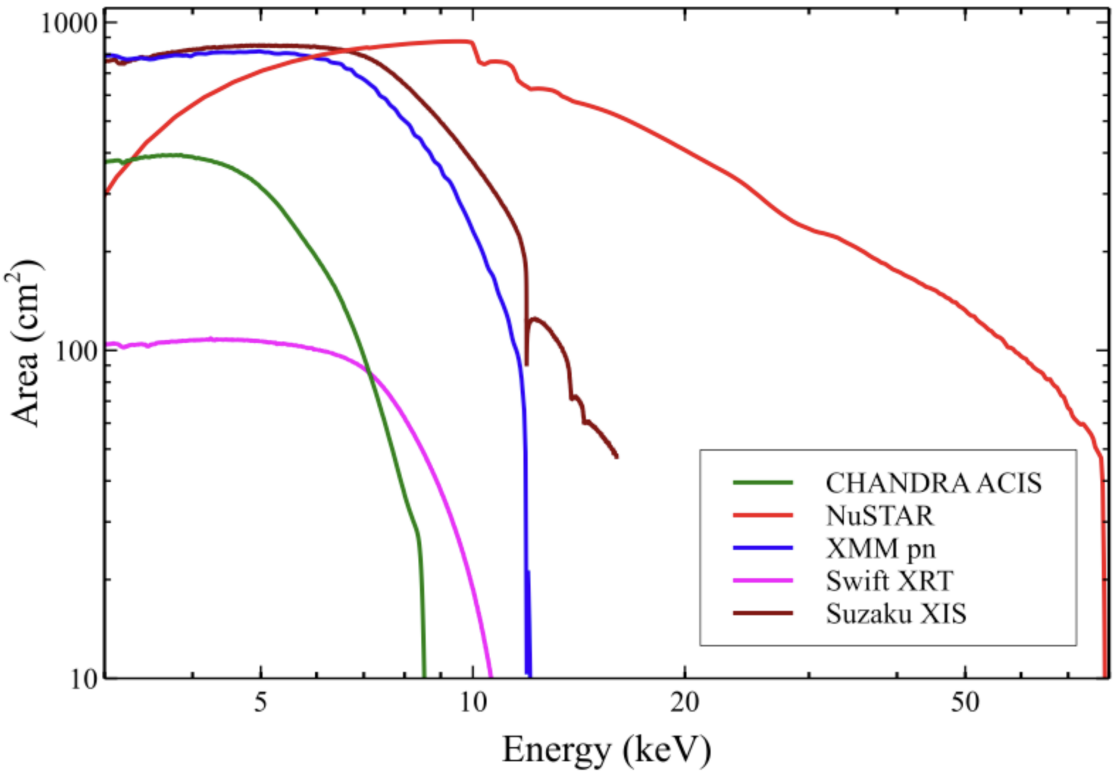

Figure 2.4: Effective collecting area of *NuSTAR* (red curve) compared to that of other operating X-ray telescopes, including *XMM-Newton* (blue) and *Chandra* (green). (Credit: NuSTAR Observatory Guide)

of 610 km.

NuSTAR is equipped with two co-aligned conical Wolter-I X-ray telescopes. Each optic has 133 mirror shell nested; the outer 43 are coated with W/Si multilayer while the inner 90 are coated with Pt/C, reaching the highest efficient reflectivity at 78.4 keV (Pt K-edge). In the fully deployed configuration, the X-ray optics and the detectors bench are separated by a stiff mast that permit to achieve a 10 m focal length. This design allows to reach a moderate angular resolution with a PSF of 18″, and the resulting FoV spans approximately 12 arcmin.

The focal plane bench hosts two solid state photon counting detectors modules, usually referred to as Focal Plane Module A (FPMA) and B (FPMB). Each module is composed by a 2x2 array of 2 mm thick CdZnTe (CZT) crystal hybrid pixel detectors.

Figure 2.4 compares the effective areas of different operating X-ray telescopes. Although the EPIC-pn has a larger effective area below 6 keV, *NuSTAR* is sensitive in a much wider range, up to almost 80 keV. *Chandra*, on the other side, exhibits a lower

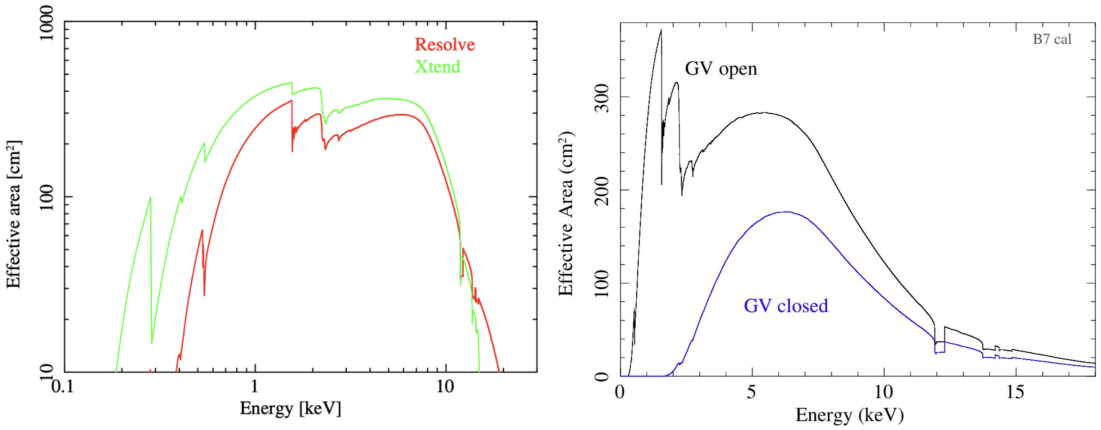

Figure 2.5: *Left panel:* On-axis effective area of XRISM Resolve (red) and Xtend (green) in log-log scale. *Right panel:* Resolve Effective area without (black solid line) and with the gate valve closed (blue solid line) in linear scale. (Credit: XRISM quick reference document)

effective area, but provides the best spatial resolution ever reached by an X-ray telescope. All the information shown here can be found in the *NuSTAR* Observatory Guide[4].

2.5 XRISM

The X-Ray Imaging and Spectroscopy Mission (XRISM) is an X-ray space telescope developed by the Japan Aerospace Exploration Agency (JAXA) in collaboration with NASA with the aim to investigate the X-ray Universe with high resolution spectroscopy. It was launched on September 6, 2023, utilizing an H-IIA rocket and seamlessly integrated into a LEO.

XRISM comprises two identical X-ray Mirror Assembly (XMA), which bear a resemblance in concept to the X-ray telescope (XRT) utilized in the Suzaku mission. Each XMA consists of 203 thin reflector shells intricately nested in a tight, co-focused, and coaxial configuration. Employing a conical approximation of the Wolter-I optic design, these assemblies achieve a focal length of 5.6 m, with the largest mirror boasting a diameter of 45 centimeters and presenting a PSF of 1.3 arcmin.

The two instruments on the focal plane are: The high resolution spectrometer Resolve, and the soft X-ray imager Xtend. In this thesis I will focus on the Resolve spectrometer.

The Resolve spectrometer consists in an X-ray microcalorimeter array featuring a 6x6 pixel setup positioned at the focal plain of the XMA. This setup enables non-dispersive high-resolution spectroscopy, offering a remarkable resolution capability of ($\Delta E \sim 5$

[4] https://heasarc.gsfc.nasa.gov/docs/nustar/nustar_obsguide.pdf

eV). Additionally, it allows limited imaging within a 3' x 3' FoV in the soft X-ray band spanning from 0.3 to 12 keV, boasting a substantial effective area of at least 210 cm^2 (see Figure 2.5). Being a non-dispersive spectrometer, Resolve excels in acquiring high-resolution spectra from both point-like and extended sources. Its impressive effective area exceeding 200 cm^2 in the Fe K-band (see Figure 2.5) surpasses that of other high-resolution spectrometers, contributing significantly to its observational capabilities in this spectral range.

However, after the launch of XRISM, a protective gate-valve over Resolve has failed to open. This issue, though significantly affecting the Resolve instrumental capabilities, fortunately does not hamper the instrument from operating. This is because there is a Be filter on the gate-valve, which consents to observe, albeit with a lower resulting effective area, in the 1.7-10 keV energy band (See Figure 2.5, right panel). All the details given here can be also found in the XRISM quick reference document[5].

[5] https://xrism.isas.jaxa.jp/research/analysis/manuals/xrqr_v1.pdf

3

A spatially resolved study of hard X-ray emission in Kepler's SNR: indications of different regimes of particle acceleration

Abstract

Synchrotron X-ray emission in young SNRs is a powerful diagnostic tool to study the population of high energy electrons accelerated at the shock front and the acceleration process. I performed a spatially resolved spectral analysis of *NuSTAR* and *XMM-Newton* observations of the young Kepler's SNR, aiming to study in detail its non-thermal emission in hard X-rays. I selected a set of regions all around the rim of the shell and extracted the corresponding spectra. The spectra were analyzed by adopting a model of synchrotron radiation in the loss-limited regime, to constrain the dependence of the cutoff energy of the synchrotron radiation on the shock velocity. I identify two different regimes of particle acceleration, characterized by different Bohm factors. In the north, where the shock interacts with a dense CSM, I find a more efficient acceleration than in the south, where the shock velocity is higher and there are no signs of shock interaction with dense CSM. My results suggest an enhanced efficiency of the acceleration process in regions where the shock-CSM interaction generates an amplified and turbulent magnetic field. By combining hard X-ray spectra with radio and $\gamma-$ray observations of Kepler's SNR, I model the spectral energy distribution. In the light of my results I propose that the observed $\gamma-$ray emission is mainly hadronic, and originates in the northern part of the shell.

The work presented in this Chapter has been published under the title "*A spatially resolved study of hard X-ray emission in Kepler's SNR: indications of different regimes of particle acceleration*" in the scientific journal "The Astrophysical Journal, Volume 935, id. 152" (Sapienza et al. 2022, DOI: https://doi.org/10.3847/1538-4357/

ac8160).

3.1 Introduction

Blast wave shocks in SNRs are sites of particle acceleration and are believed to be the primary source of galactic CRs. For shocks in SNRs, the main acceleration mechanism is the DSA (for a brief review refer to Section 1.4; Bell 1978a,b; Axford et al. 1977; Blandford & Ostriker 1978). The first evidence for high-energy ($E > 10^{12}$ eV) electrons accelerated in SNR shocks came with the detection of non-thermal X-ray emission of SN 1006 (Koyama et al. 1995). As a matter of fact, the study of X-ray synchrotron emission of SNRs can provide helpful insights about the acceleration process, such as the shape of the electron energy distribution and the mechanisms that limit the maximum energy that electrons can reach. As discussed in Sect. 1.5, different mechanisms can be invoked to limit the maximum electron energy in the acceleration process (Reynolds 2008); for example, it can be limited by radiative losses (*loss-limited* scenario) or by the finite acceleration time available (*age-limited* scenario).

Kepler's SNR owes its name to Johannes Kepler, who extensively studied its parent supernova (SN 1604). This remnant has a roughly spherical shape with an angular radius of approximately 1.8′ with two characteristic protrusions (also called "ears"), one located in the south-east of the shell and the other located in the north-west. The SNR is very likely the result of a type Ia SN (Kinugasa & Tsunemi 1999). Reynolds et al. (2007) found that Kepler's SNR is interacting with nitrogen-rich CSM in the north and suggest a single-degenerate scenario for the explosion (with the companion possibly being a runaway AGB star, see Bandiera 1987, Velázquez et al. 2006, Chiotellis et al. 2012 and Kasuga et al. 2021), albeit there is no evidence for a survived companion star (Kerzendorf & Sim 2014, Ruiz-Lapuente et al. 2018).

Reynoso & Goss (1999) derived a distance of 4.8 ± 1.4 kpc, based on H I absorption from radio observations, while Aharonian et al. (2008) suggested a lower limit of 6.4 kpc motivated by the lack of a detectable γ-ray flux. However, recent estimates based on proper motion measurements derived a distance $d = 5.1^{+0.8}_{-0.7}$ kpc (Sankrit et al. 2016). I then adopt a distance of $d = 5$ kpc throughout this thesis for this SNR.

Prominent particle acceleration in Kepler's SNR is testified by its energetic non-thermal emission. The detection of GeV $\gamma-$ray emission from Kepler's SNR was recently presented by Xiang & Jiang (2021) and interpreted as a signature of hadronic emission. Similar conclusions were reported by Acero et al. (2022) who propose the hadronic emission to originate in the northern part of the shell, while synchrotron and Inverse Compton emission are interpreted as originating in the southern regions. H. E. S. S. Collaboration et al. (2022) reported the detection of Very High Energy (VHE) γ-ray emission from Kepler's SNR.

The presence of non-thermal X-ray emission in Kepler's SNR was first discovered in

its south-eastern region by Cassam-Chenaï et al. (2004), using an *XMM-Newton* observation. Reynolds et al. (2007) conducted a spectral analysis in several regions of Kepler's SNR confirming that some of them are dominated by synchrotron radiation. Recently, Nagayoshi et al. (2021) reported the first robust detection of hard X-ray emission, in the 15-30 keV band, by analyzing a *Suzaku* HXD observation. Several spatially resolved studies found that the roll-off frequency of the synchrotron radiation in Kepler's SNR lies in the range $\nu_r \sim 1 - 8 \times 10^{17}$ Hz (Cassam-Chenaï et al. 2004, Bamba et al. 2005, Nagayoshi et al. 2021). One can estimate if the cutoff energy (E_{max}) of the synchrotron emitting electrons is loss-limited or time-limited by comparing the time-scale for synchrotron losses (τ_{sync}, see Equation 1.28) with the age of the remnant (t_{age} = 419 yrs). On the basis of the one-zone model of broad-band Spectral Energy Distribution (SED), Nagayoshi et al. (2021) adopted a magnetic field of $\sim$ 40 μG and a roll-off frequency $\nu_r = 1 \times 10^{17}$ Hz, corresponding to $\tau_{sync} \sim 330$ yrs (refer to Equation 1.29). Non-linear DSA predicts an amplification of the magnetic field strength as a result of the flux of kinetic energy of the CRs streaming ahead of the shock (Bell 2004). Estimates of the magnetic field strength in Kepler's SNR, based on the thickness of the X-ray synchrotron filaments, provide values in the range 170-250 μG (Völk et al. 2005, Parizot et al. 2006, Rettig & Pohl 2012, Reynolds et al. 2021). Assuming a value of magnetic field of 170 μG and the roll of frequency measured by Nagayoshi et al. (2021) I obtain $\tau_{sync} \sim 30$ yrs. In any case, the synchrotron cooling time is always lower than the age of Kepler's SNR and I can therefore consider the loss-limited scenario as the most appropriate for this source.

Tsuji et al. (2021) measured the cutoff photon energy in different regions of several SNRs, Kepler's SNR among them, by describing the non-thermal X-ray emission with the loss-limited model proposed by Zirakashvili & Aharonian (2007) (see Equation 1.30). In this model, the cutoff photon energy (ϵ_0) is related to the shock speed, v_{sh}, through $\epsilon_0 \propto v_{sh}^2 \eta^{-1}$ where η, or Bohm diffusing factor, is the ratio between the diffusion coefficient and $c\lambda/3$ (where λ is the Larmor radius, the minimum value $\eta = 1$ corresponding to the Bohm limit) and is strongly related to the turbulence of the magnetic field, which scatter the charged particles. Tsuji et al. (2021) studied the dependence of ϵ_0 on v_{sh}, with a spatially resolved spectral analysis in order to estimate η in different remnants. However, the spatially resolved analysis of Kepler's SNR lacks of the hard part of the spectrum, and the $\epsilon_0 - v_{sh}$ plot shows a clear trend only for synchrotron dominated regions, while no correlation can be found for other regions. Lopez et al. (2015) performed a similar analysis using a deep *NuSTAR* observation of Tycho's SNR. They found that in Tycho's SNR the highest energy electrons are accelerated at the fastest shocks, with a steep dependence of the roll-off frequency on the shock speed.

In this chapter, I present the first analysis of an archive *NuSTAR* observation of Kepler's SNR. I exploit the high sensitivity of the *NuSTAR* telescope in the high energy X-ray to study the morphological and spectral properties in this energy band. I also perform

a spatially resolved measurement of the cutoff energy of the synchrotron radiation, combining the *NuSTAR* data with an *XMM-Newton* observation, which allows me to get physical insights on the origin of non-thermal emission. I describe the data reduction in Section 3.2. Section 3.3 is dedicated to the results of image and spectral analysis. Discussion and conclusions are presented in Section 3.4 and Section 3.5, respectively.

3.2 Data reduction

3.2.1 *NuSTAR* observation

The *NuSTAR* (see Sect. 2.4) observation of Kepler's SNR was performed from October 7, 2014 for an exposure time of 246 ks (Obs. ID: 40001020002, PI: F. Harrison), with pointing coordinates $\alpha_{J2000} = 17^h30^m36.4^s$ and $\delta_{J2000} = -21°30'13''$. I processed the data using `nupipeline` of the *NuSTAR Data Analysis Software* (NuSTARDAS version 2.0.0 with CALDB version 20210202) included in HEAsoft version 6.28.

The maps shown in this chapter were obtained by summing the photon counts detected in each pixel by the two CZT detectors FPMA and FPMB in a given energy band. I performed a spatially resolved spectral analysis for both FPMA and FPMB by extracting the spectra from different regions of the remnant using the `nuproducts` pipeline for an extended source. Spectra were rebinned to have at least 25 counts per bin. For each region, FPMA and FPMB spectra were fitted simultaneously. I used the `nuproducts` pipeline to produce the redistribution matrix file (RMF) and the ancillary response file (ARF), and to extract the background spectrum. As for the background, I selected an extraction region for each spectrum, outside of the shell and in the same chip as the source extraction region.

3.2.2 *XMM-Newton* Observation

I complemented *NuSTAR* data analysis with the analysis of an *XMM-Newton* EPIC (see Sect. 2.2) observation of Kepler's SNR, performed from March 19, 2020 for an exposure time of 140 ks (Obs. ID: 0842550101, PI: T. Sato). The observation has pointing coordinates $\alpha_{J2000} = 17^h30^m36.9^s$, $\delta_{J2000} = -21°30'01.1''$, and was performed with the thick filter, in FF mode for the EPIC MOS cameras, and in large window mode for the EPIC pn camera.

I processed the Observation Data Files (ODF) using the `emproc` and the `epproc` tasks of the Science Analysis System (SAS) software, version 18.0.0, respectively for the MOS and the pn cameras. The obtained event files were filtered for soft-proton contamination using the `espfilt` task, thus obtaining a screened exposure time of 108.2 ks for MOS1, 110.1 for MOS2 and 94.7 ks for the pn camera. Images of the MOS cameras were background subtracted by adopting the double subtraction procedure

described in Miceli et al. (2006), retaining only events with `FLAG = 0` and `PATTERN ≤ 12`. With this method I removed instrumental, particles and diffuse X-ray background from the images by using the Filter Wheel Closed (FWC)[1] and the Blank Sky (BS)[2] files available at XMM ESAC web pages. Count-rate images were obtained by mosaicking MOS 1 and MOS 2 maps, correcting for the vignetting and then adaptively smoothed (with the `asmooth` task) to a signal-to-noise ratio of 10.

I analyzed the EPIC-pn spectra extracted from the same regions adopted for the *NuSTAR* spectral analysis. To take into account the vignetting effect in the spectra, I added a "weight" column to the pn event file with the `evigweight` SAS command. Spectra were extracted by using the `evselect` task, retaining only events with `FLAG = 0` and `PATTERN ≤ 4`. For each spectrum, I produced the RMF and ARF files, with the `rmfgen` and the `arfgen` tasks, respectively. Spectra were rebinned so as to have at least 25 counts per bin. For the background, I selected two extraction regions outside the shell: one, at south, for regions 1-5, and one, at north, for regions 6-11 and for the "Hard Knot" (see Section 3.3.1 and Figure 3.1 for the region selection). Spectral analysis of *NuSTAR* and *XMM-Newton* data was performed with the HEAsoft software XSPEC version 12.11.1 (Arnaud 1996). Spectra from different cameras were fitted simultaneously.

3.2.3 *Chandra* Observation

To study in detail the morphology of the remnant, I also analyzed *Chandra* (see Sect. 2.3) observations performed between April 27, 2006 and August 3, 2006 for a total exposure time of 750 ks (Obs. ID: 6714, 6715, 6716, 6717, 6718, 7366; PI: S. Reynolds). Data were reprocessed with the CIAO v4.13 software using CALDB 4.9.4. I reprocessed the data by using the `chandra_repro` task. Mosaicked flux images were obtained by using the `merge_obs` task.

3.3 Results

3.3.1 Images

Figure 3.1 shows the *NuSTAR* count image in the 3 – 8 keV, 8 – 15 keV, and 15 – 30 keV bands, together with the *XMM-Newton* count-rate image in the 4.1 – 6 keV band. The presence of source photons up to 30 keV confirms the detection of hard X-rays by Nagayoshi et al. (2021). Thanks to the angular resolution of *NuSTAR*, I can also reveal the spatial distribution of the hard X-ray emission in Kepler's SNR. Figure 3.1 shows

[1] https://www.cosmos.esa.int/web/xmm-newton/filter-closed

[2] http://xmm-tools.cosmos.esa.int/external/xmm_calibration//background/bs_repository/blanksky_all.html

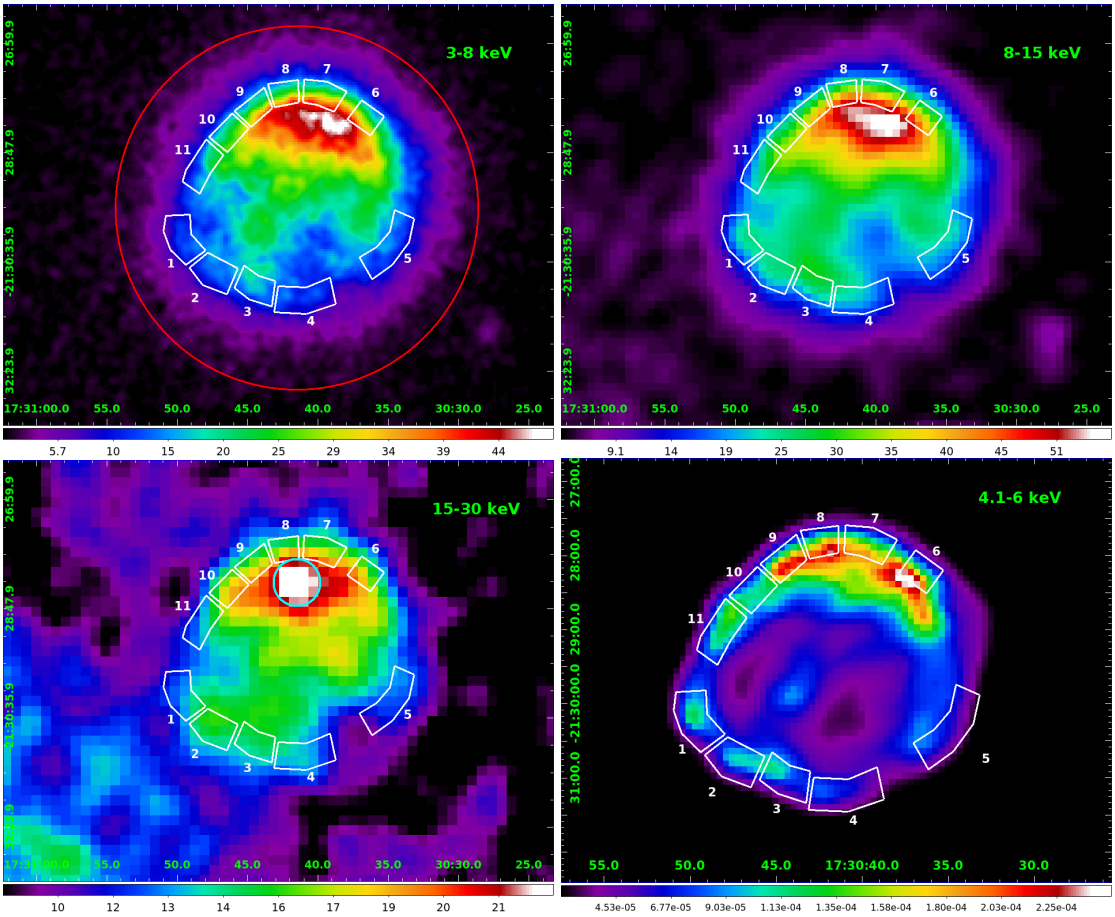

Figure 3.1: *Upper-left panel: NuSTAR* count image in the 3 – 8 keV band in linear scale. The bin size is 2.5″, and the image was smoothed through the convolution with a Gaussian with $\sigma = 7.5''$. The red circle marks the extraction region for the total spectrum (see Section 3.3.2). *Upper-right panel: NuSTAR* count image in the 8 – 15 keV band in linear scale. The bin size is 7.5″, and the image was smoothed through the convolution with a Gaussian with $\sigma = 22.5''$. *Bottom-left panel: NuSTAR* count image in the 15 – 30 keV band in linear scale. The bin size is 10″, and the image was smoothed through the convolution with a Gaussian with $\sigma = 30''$. The cyan circle marks the extraction region for the hard X-ray knot (see Section 3.3.4) Regions selected for the spatially resolved spectral analysis at the rim of the shell are indicated by white polygons. *Bottom-right panel: XMM-Newton* count-rate image in the 4.1 – 6 keV band in linear scale. The bin size is 5″ and the image was adaptively smoothed to a signal-to-noise ratio of 10. North is up and east is to the left.

that the morphology of the emission in the 8 – 15 keV band is roughly similar to the soft X-ray emission, being brighter in the northern part of the shell, where the shock is interacting with the nitrogen-rich CSM. Similarly, in the 15 – 30 keV band I observe a higher surface brightness in the north than in the south. However, some differences in the morphology of the hard X-ray emission with respect to the soft emission are visible, as, for example, the position of the peak in surface brightness in the 15 – 30 keV band, which is located to the east with respect to the peak in the 3 – 8 keV map. I also notice an enhancement in the surface brightness at southeast. The 4.1 – 6.0 keV *XMM-Newton* count-rate image is bright in the outermost regions of the remnant, where synchrotron filaments have been spotted (Reynolds et al. 2007). I point out that, because of the higher densities expected in the northern part of the shell, I also expect a larger contribution of thermal bremsstrahlung therein. The high-energy tail of thermal bremsstrahlung can, in principle, contribute to the 15 – 30 keV emission in the northern part of the shell. However, as I show in Section 3.3.3, the bulk of the hard X-ray emission of Kepler's SNR has likely a non-thermal origin.

3.3.2 Total Spectrum

I extract the spectrum of the whole Kepler's SNR from *NuSTAR* FPMA and FPMB using a circle with a radius of 3' and center coordinates $\alpha_{J2000} = 17^h30^m41.44^s$ and $\delta_{J2000} = -21°29'27.7''$, shown in Figure 3.1. I model the FPMA and FPMB global spectra in the 4.1 – 30 keV band, I exclude the 3 – 4.1 keV band to avoid the strong contamination of thermal emission present in this energy band. I model the hard X-rays as non-thermal emission, by adopting a similar approach as Lopez et al. (2015). However, here I describe the continuum as synchrotron emission from an electron energy distribution limited by radiative losses (hereafter loss-limited model, Zirakashvili & Aharonian 2007), which has been shown to provide an accurate description of non-thermal X-ray emission in young SNRs (e.g., Zirakashvili & Aharonian 2010; Morlino & Caprioli 2012; Miceli et al. 2013a; Tsuji et al. 2021). The spectrum of the loss-limited model is given by Equation 1.30. I include interstellar absorption (`Tbabs` model in XSPEC), with a hydrogen column density fixed to $n_{\rm H} = 6.4 \times 10^{21}$ cm^{-2} (as in Katsuda et al. 2015). I also include three ad-hoc Doppler-broadened Gaussian components to model the Fe K line (at $\sim$ 6.4 keV, see Yang et al. 2013), the Cr and Mn emission lines and the Ni emission lines. Figure 3.2 shows the total spectra (FPMA and FPMB) of Kepler's SNR with the corresponding best fit model and residuals. The best-fit values, with error bars at 68% confidence level, are reported in Table 3.1. The fit provides a $\chi^2/d.o.f. = 1115.82/918$ and an average cutoff energy parameter $\varepsilon_0 = 0.640^{+0.014}_{-0.013}$ keV. This value of ε_0 corresponds to a roll-off frequency $\nu_r = 1.55^{+0.03}_{-0.03} \times 10^{17}$ Hz, which is in good agreement with the estimate obtained by Nagayoshi et al. (2021, $\sim 1 \times 10^{17}$ Hz) on the basis of the modeling of the broad band spectral energy distribution.

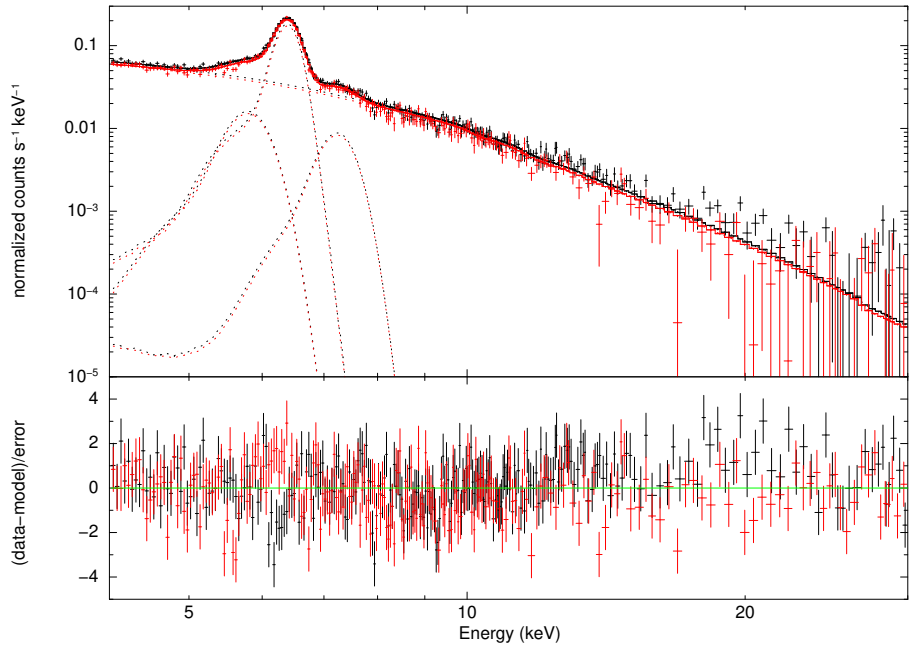

Figure 3.2: FPMA (black) and FPMB (red) total spectra of Kepler's SNR with the corresponding best-fit model and residual in the 4.1 − 30 keV band.

I fitted simultaneously the *NuSTAR* FPMA and FPMB spectra (in the 4.1 − 30 keV band), and the *Suzaku* HXD-PIN spectrum (in the 15 − 30 keV band), with the loss-limited model. I allowed the normalization of the *Suzaku* spectra to differ from that of the *NuSTAR* spectra within a 10% to account for the characteristic cross-calibration factor between the two telescopes (Madsen et al. 2017). I found that the hard X-ray flux of Kepler's SNR in the 15 − 30 keV band is $F_X = 1.05^{+0.04}_{-0.03} \times 10^{-12}$ erg cm^{-2} s^{-1} ($F_X = 1.15^{+0.02}_{-0.24} \times 10^{-12}$ erg cm^{-2} s^{-1} for Suzaku HXD, taking into account the cross-calibration factor). Though this value is lower than that reported by Nagayoshi et al. (2021, $F_X = 2.75^{+0.78+0.81}_{-0.77-0.82} \times 10^{-12}$ erg cm^{-2} s^{-1}), it is still consistent with it, considering the cross-calibration factor and the 90% statistical and systematic errors.

3.3.3 Spatially resolved Spectral Analysis

I performed a spatially resolved spectral analysis by analyzing the spectra extracted from the eleven regions shown in Figure 3.1. I focus on the outer rim of the shell, by defining

Table 3.1: Best-ft values for Kepler's SNR *NuSTAR* spectra.

Parameter	Value
Fe K center (keV)	$6.4018^{+0.0016}_{-0.0014}$
σ (keV)	$0.091^{+0.003}_{-0.003}$
Norm (10^{-4} photons cm^{-2} s^{-1})	$2.96^{+0.02}_{-0.02}$
ε_0 (keV)	$0.640^{+0.014}_{-0.013}$
norm (10^{-3})	$29.0^{+1.8}_{-1.7}$
$\chi^2/d.o.f.$	1115.82/918

Notes. Errors are at the 68% confidence level.

regions with similar photon counts in the 8 – 30 keV band ($N_{8-30} \approx 800$) in order to investigate the relation between the shock velocity and the maximum energy of electrons accelerated at the shock front.

To ascertain the origin of the hard X-ray emission, I first focus on the *NuSTAR* spectra in the 8 – 30 keV band. The emission in this band is characterized by a featureless continuum, which can be modeled with a power-law with spectral index $\Gamma \sim 3$ in all the eleven regions considered. As an example, in the southern part of the shell, I obtain $\Gamma = 3.5^{+0.5}_{-0.4}$ in region 2 and $\Gamma = 2.7^{+0.3}_{-0.3}$ in region 5; similarly, in the northern limb, $\Gamma = 3.0^{+0.4}_{-0.4}$ in region 7 and $\Gamma = 2.7^{+0.5}_{-0.4}$ in region 10. By modeling this relatively flat emission as a thermal bremsstrahlung, I derive quite high plasma temperatures (namely, $kT = 5.8^{+1.8}_{-1.2}$ keV in region 2, $kT = 9^{+3}_{-2}$ keV in region 5, $kT = 7.8^{+2.8}_{-1.8}$ keV in region 7 and $kT = 10^{+5}_{-3}$ keV in region 10). I then consider the bulk of the hard X-ray emission to be non-thermal. However, I point out that, by including a thermal contribution to the hard X-ray spectra, my conclusions stay unaffected, as shown below.

I fit the spectra in the 4.1 – 30 keV band (4.1 – 8 keV for EPIC-pn and 4.1 – 30 keV for *NuSTAR* FPMA and FPMB) using the loss-limited model with an additional Gaussian component to take into account the Fe K line. I also added a further Gaussian component in regions 8-11 to model the Cr/Mn K line detected therein. The spectra from all regions, with the corresponding best-fit model and residual, are shown in Figure 3.3.

The best-fit values for all regions (with the corresponding $\chi^2/d.o.f.$) are shown in Table 3.2 (error bars are at 68% confidence level).

As a crosscheck, I verified that my assumption on the non-thermal origin of the hard X-ray emission is consistent with the broadband X-ray spectrum. To this end, I fit the spectra of all the regions in the 0.3 – 30 keV (0.3 – 8 keV for EPIC-pn and 3 – 30 keV for *NuSTAR* FPMA and FPMB) by adding thermal components to the loss-limited model derived above.

The soft X-ray spectra (0.3 – 4.1 keV) for the northern regions show prominent thermal emission features, as the Fe-L line complex in the 0.7 – 1.2 keV band, and the

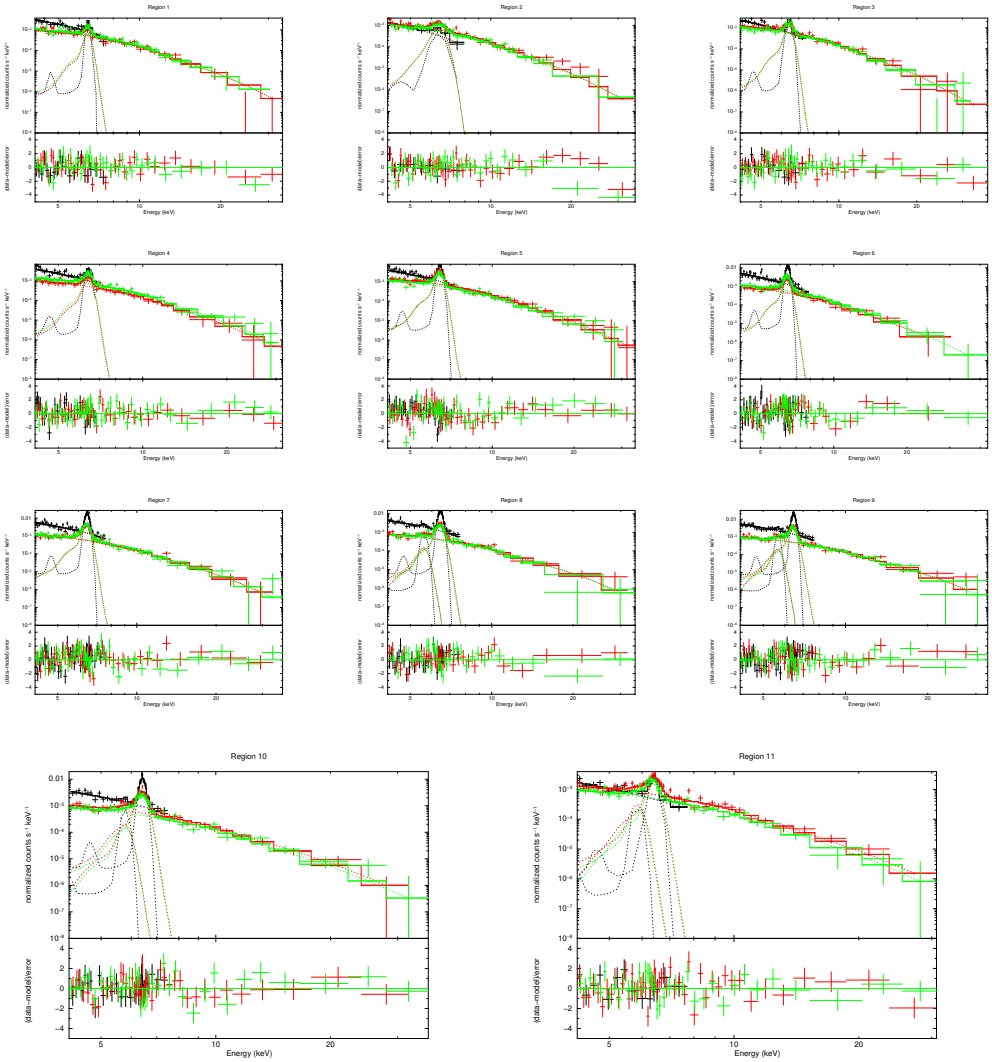

Figure 3.3: EPIC-pn (black), FPMA (red) and FPMB (green) spectra extracted from regions 1-11 (see Figure 3.1) with the corresponding best-fit model and residual in the 4.1 – 30 keV band (see Table 3.2 for the best-fit values).

Si, S, Ar, Ca K lines, respectively at ∼ 1.86, keV ∼ 2.48 keV, ∼ 3.11 keV and ∼ 3.86 keV. All the spectra are shown in Figure 3.4, with the corresponding best-fit model and residuals.

The spectra extracted from southern regions (regions 1 – 5, characterized by a fainter thermal emission) are well described by two components of isothermal optically thin plasma in NEI with non-solar abundances and Doppler broadening (`bvrnei` model in XSPEC), in addition to the absorbed loss-limited model (the parameters of the loss-

Table 3.2: Best-fit values for spectra from regions labeled from 1 to 11.

Region #	Fe K center (keV)	σ (keV)	norm (10^{-6} photons cm^{-2} s^{-1})	ε_0 (keV)	norm (10^{-3})	$\chi^2/d.o.f.$
1	$6.445^{+0.019}_{-0.018}$	< 0.08	$0.99^{+0.12}_{-0.12}$	$0.57^{+0.07}_{-0.06}$	$0.65^{+0.24}_{-0.18}$	107.08/97
2	$6.38^{+0.04}_{-0.04}$	$0.26^{+0.06}_{-0.05}$	$0.66^{+0.09}_{-0.08}$	$0.47^{+0.05}_{-0.04}$	$0.48^{+0.17}_{-0.13}$	117.76/90
3	$6.427^{+0.018}_{-0.016}$	$0.09^{+0.02}_{-0.02}$	$1.21^{+0.10}_{-0.11}$	$0.43^{+0.04}_{-0.04}$	$1.1^{+0.4}_{-0.3}$	97.02/93
4	$6.395^{+0.016}_{-0.014}$	$0.10^{+0.02}_{-0.02}$	$2.27^{+0.18}_{-0.18}$	$0.48^{+0.05}_{-0.04}$	$1.3^{+0.4}_{-0.3}$	117.52/118
5	$6.410^{+0.009}_{-0.008}$	$0.084^{+0.014}_{-0.014}$	$3.87^{+0.19}_{-0.19}$	$0.54^{+0.06}_{-0.05}$	$0.9^{+0.3}_{-0.2}$	175.24/128
6	$6.441^{+0.007}_{-0.006}$	$0.082^{+0.008}_{-0.008}$	$6.6^{+0.3}_{-0.3}$	$0.50^{+0.05}_{-0.04}$	$1.5^{+0.5}_{-0.4}$	168.34/121
7	$6.448^{+0.005}_{-0.005}$	$0.083^{+0.006}_{-0.007}$	$9.7^{+0.3}_{-0.3}$	$0.59^{+0.06}_{-0.05}$	$1.0^{+0.3}_{-0.3}$	189.15/154
8	$6.443^{+0.006}_{-0.007}$	$0.091^{+0.008}_{-0.008}$	$7.2^{+0.3}_{-0.3}$	$0.67^{+0.09}_{-0.07}$	$0.60^{+0.24}_{-0.17}$	123.26/111
9	$6.434^{+0.005}_{-0.005}$	$0.067^{+0.007}_{-0.007}$	$9.2^{+0.3}_{-0.3}$	$0.64^{+0.08}_{-0.07}$	$0.8^{+0.3}_{-0.2}$	158.83/131
10	$6.419^{-0.006}_{-0.007}$	$0.078^{+0.009}_{-0.009}$	$5.4^{+0.2}_{-0.2}$	$0.59^{+0.07}_{-0.06}$	$0.68^{+0.26}_{-0.19}$	108.60/109
11	$6.404^{+0.012}_{-0.013}$	$0.09^{+0.03}_{-0.02}$	$1.54^{+0.10}_{-0.10}$	$0.59^{+0.06}_{-0.06}$	$0.34^{+0.12}_{-0.09}$	121.37/98
Hard Knot	$6.428^{+0.004}_{-0.003}$	$0.101^{+0.004}_{-0.004}$	$24.8^{+0.6}_{-0.6}$	$0.70^{+0.04}_{-0.04}$	$1.5^{+0.2}_{-0.2}$	466.54/340

Notes. Errors are at the 68% confidence level.

limited model are fixed to the best-fit values shown in Table 3.2). I also included two Gaussian lines to take into account missing Fe-L lines in the `bvrnei` model (as in Katsuda et al. 2015). The spectra extracted from northern regions (regions 6-11, characterized by a brighter thermal emission) were fitted by adding to the loss-limited model (with parameters fixed to the values in Table 3.2) three thermal components. I found a degeneracy between the Fe abundance, the normalization and the temperature (kT_h) of the hottest component of the plasma. Nagayoshi et al. (2021) found $kT_h = 3.74^{+0.12}_{-0.03}$ keV so I decided to set an upper limit of 4 keV for kT_h. The values of the best-fit parameters are listed in Table 3.3 and 3.4. This model provides a good description of the spectra of all regions ($1 < \chi^2/d.o.f. < 1.4$). I note that in Table 3.4, the spectral fitting analysis indicates higher abundances of intermediate mass elements (e.g., Si, S, Ar, Ca) than in Katsuda et al. (2015) and Holland-Ashford et al. (2023). Although I cannot entirely rule out the possibility that this effect might be partially due to the assumption of a dominating non-thermal continuum (since a lower thermal continuum would require higher abundances to better fit the emission lines), it is important to note that CCD spectra typically exhibit a degeneracy between the abundances and the normalization parameter. To verify this, I checked that dividing the abundances by a factor of ten and simultaneously multiplying the normalization parameter by the same factor did not significantly affect the quality of the fit. Nonetheless, this fitting analysis is intended as a phenomenological crosscheck to verify the initial assumption. I conclude that the modeling of the synchrotron emission adopted in the analysis of the "hard" spectra is consistent with the broadband X-ray spectra and provides a robust description of the non-thermal emission in Kepler's SNR.

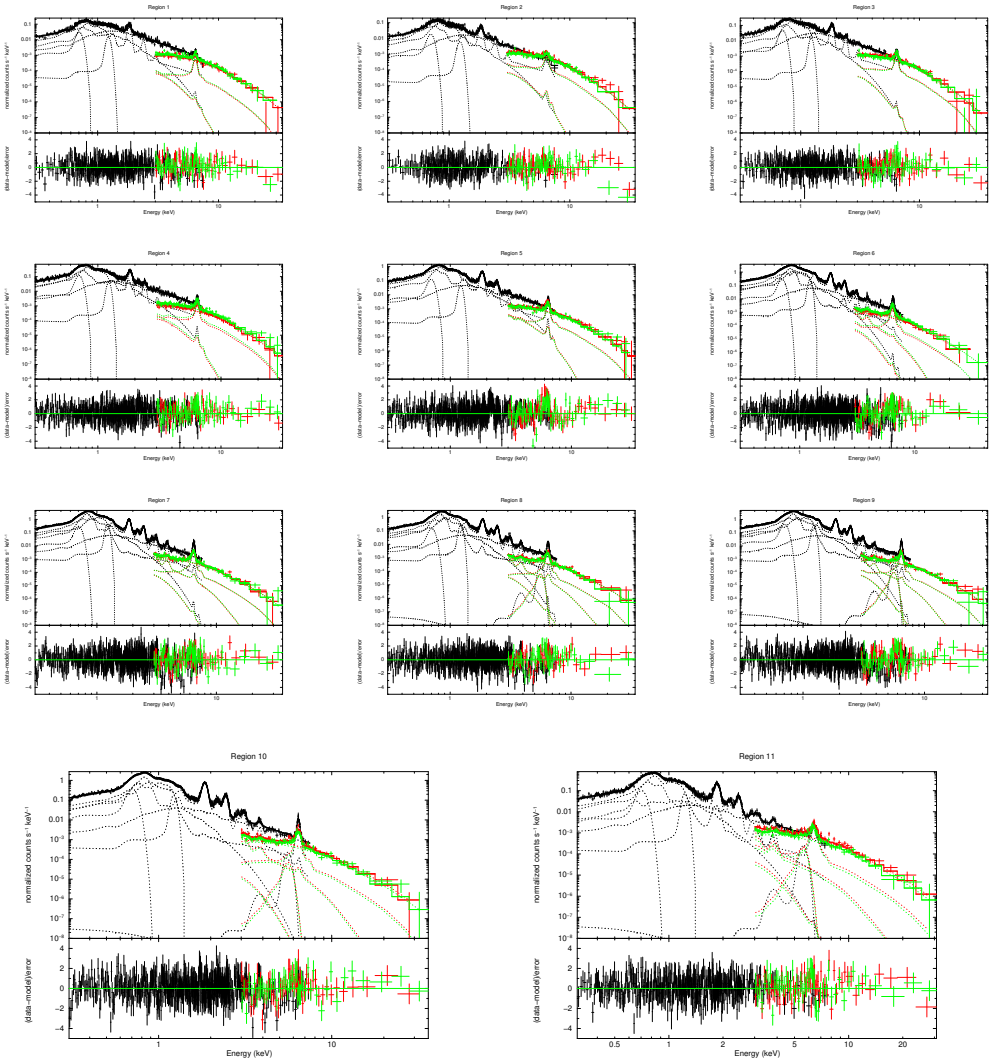

Figure 3.4: EPIC-pn (black), FPMA (red) and FPMB (green) spectra extracted from regions 1-11 (see Figure 3.1) with the corresponding best-fit model and residual in the 0.3 – 30 keV band.

3.3.4 Hard X-ray knot

Lastly, I analyzed the spectrum of the knot with the brightest hard X-ray emission, which I spotted in the 15-30 keV band map of Kepler's SNR. In particular, I extracted the EPIC-pn, FPMA and FPMB spectra from the circular region indicated by the cyan circle in the lower left panel of Figure 3.1.

I modeled the spectra in the the 4.1 – 30 keV band (4.1 – 8 keV for EPIC-pn and

Table 3.3: Best-fit values for broadband spectra of southern regions (1-5).

Component	Parameter	#1	#2	#3	#4	#5
TBabs	n_H (10^{22} cm^{-2})			0.64(fixed)		
$\texttt{gauss}_1$	Fe L+O K (keV)			0.708(fixed)		
	Norm (10^{-4} photons cm^{-2} s^{-1})	$2.8^{+0.6}_{-0.7}$	$1.7^{+0.7}_{-0.7}$	$4.3^{+0.9}_{-0.9}$	$11.0^{+1.3}_{-1.2}$	$11.6^{+1.3}_{-2.1}$
$\texttt{gauss}_2$	Fe L+Ne K (keV)			1.227(fixed)		
	Norm (10^{-4} photons cm^{-2} s^{-1})	$0.053^{+0.017}_{-0.014}$	$0.026^{+0.014}_{-0.014}$	$0.051^{+0.016}_{-0.016}$	$0.14^{+0.02}_{-0.02}$	$0.15^{+0.03}_{-0.02}$
$\texttt{brvnei}_1$	kT_1 (keV)	$0.63^{+0.09}_{-0.05}$	$0.65^{0.11}_{-0.09}$	$0.54^{+0.06}_{-0.06}$	$0.68^{+0.03}_{-0.07}$	$0.721^{+0.007}_{-0.073}$
	O	1 (fixed)	$1.5^{+1.0}_{0.9}$	$2.2^{+0.3}_{-0.6}$	$0.31^{+0.18}_{-0.17}$	1 (fixed)
	Ne	1 (fixed)	$1.3^{+1.1}_{-0.9}$	1 (fixed)	< 0.5	1 (fixed)
	Mg	1 (fixed)	6^{+4}_{-3}	$4.80485^{+1.7}_{-1.4}$	$0.9^{+0.5}_{-0.5}$	$4.3^{+0.8}_{-0.7}$
	Si		1 (fixed)		$9.0^{+1.9}_{-1.8}$	1 (fixed)
	Fe	19^{+5}_{-3}	81^{+18}_{-15}	51^{+12}_{-7}	50^{+4}_{-5}	107^{+4}_{-5}
	τ_1 (10^9 cm^{-3} s)	< 0.6	$1.05^{+0.14}_{-0.13}$	< 0.62	$0.83^{+0.07}_{-0.12}$	$1.20^{+0.04}_{-0.03}$
	Velocity (10^4 km s^{-1})	0	$0.7^{+0.3}_{-0.5}$	0	0	$0.64^{+0.07}_{-0.10}$
	EM_1 (10^{56} cm^{-3})	$2.9^{+0.4}_{-0.8}$	$0.62^{+0.20}_{-0.14}$	$2.4^{+0.7}_{-0.8}$	$4.6^{+1.1}_{-0.4}$	$4.16^{+0.10}_{-0.27}$
	kT_2 (keV)	> 3.88	> 3.89	> 3.93	> 3.91	> 3.95
$\texttt{brvnei}_2$	O	1 (fixed)	< 2.5	< 1.7	5^{+3}_{-2}	1 (fixed)
	Ne	$3.7^{+5.3}_{-1.4}$	$2.4^{+1.2}_{-1.0}$	$4.2^{1.3}_{-0.8}$	$5.2^{+2.1}_{-1.3}$	23^{+10}_{-3}
	Mg	5^{+7}_{-2}	$1.2^{+0.9}_{-0.8}$	$1.2^{+0.7}_{-0.5}$	$2.3^{1.0}_{-0.7}$	$14.0^{+1.3}_{-3.0}$
	Si	$45^{+64}_{-1.7}$	20^{+6}_{-4}	30^{+10}_{-6}	37^{+14}_{-8}	170^{+720}_{-40}
	S	50^{+80}_{-20}	23^{+9}_{-6}	38^{14}_{-9}	48^{+19}_{-11}	300^{+700}_{-40}
	Ar	50^{+100}_{-40}	26^{+24}_{-19}	40^{+30}_{-20}	36^{+25}_{-17}	180^{+40}_{-50}
	Ca		1 (fixed)		24^{+30}_{-22}	110^{+70}_{-80}
	Fe	27^{+3}_{-2}	$13.8^{1.2}_{-1.1}$	$21.5^{+1.3}_{-1.2}$	$26.8^{+1.1}_{-1.3}$	$43.5^{+0.7}_{-1.7}$
	Ni			=Fe		
	τ_2 (10^9cm^{-3} s)	$4.51^{+2.3}_{0.17}$	$5.3^{+0.3}_{-0.2}$	$4.65^{+0.14}_{-0.12}$	$5.12^{+0.13}_{-0.13}$	$7.14^{+0.10}_{-0.07}$
	Velocity (10^4 km s^{-1})	$0.58^{+0.09}_{-0.09}$	$0.738^{+0.09}_{-0.10}$	$0.42^{+0.06}_{-0.07}$	$0.42^{+0.05}_{-0.05}$	$0.57^{0.02}_{-0.03}$
	EM_2 (10^{56} cm^{-3})	$1.959^{+0.003}_{-0.004}$	$0.050^{+0.004}_{-0.004}$	$0.074^{+0.003}_{-0.004}$	$0.113^{+0.007}_{-0.006}$	$0.095^{+0.006}_{-0.007}$
	$\chi^2/d.o.f.$	458.98/456	403.14/355	423.15/443	608.79/573	824.00/626

Notes. Solar abundances from Anders & Grevesse (1989). τ lower limit set to be 5×10^8 cm^{-3} s. Abundances upper limit is set to be 1000 times the solar one. Velocity upper limit set to be 1×10^4 m s^{-1}. Abundances consistent with their solar values were fixed to 1.

4.1 − 30 keV for *NuSTAR* FPMA and FPMB) by adopting the loss-limited model (with the additional Gaussian component) described in detail in Section 3.3.3. Spectra from the hard knot, with the corresponding best-fit model and residual, are shown in Figure 3.5, while the best fit values (with errors at the 68% confidence level) are shown in Table 3.2.

3.4 Discussion

Table 3.4: Best-fit values for broadband spectra of northern regions (6-11).

Component	Parameter	#6	#7	#8	#9	#10	#11
TBabs	n_H (10^{22} cm^{-2})	0.64(fixed)					
$\texttt{gauss}_1$	Fe L+O K (keV)	0.708(fixed)					
	Norm (10^{-4} photons cm^{-2} s^{-1})	$18.5^{+1.7}_{-1.8}$	$17.16^{+0.15}_{-0.15}$	$8.6^{+1.3}_{-1.3}$	$25.2^{+1.7}_{-1.5}$	$22.1^{+1.2}_{-1.4}$	$5.9^{+1.2}_{-0.7}$
$\texttt{gauss}_2$	Fe L+Ne K (keV)	1.227(fixed)					
	Norm (10^{-4} photons cm^{-2} s^{-1})	$0.83^{+0.07}_{-0.05}$	$1.413^{+0.06}_{-0.06}$	$1.02^{+0.05}_{-0.05}$	$1.18^{+0.06}_{-0.06}$	$0.584099^{+0.04}_{-0.04}$	$0.23^{+0.02}_{-0.02}$
$\texttt{gauss}_3$	Cr K+Mn K (keV)	5.6 (fixed)					
	Norm (10^{-4} photons cm^{-2} s^{-1})	/	/	$0.003^{+0.002}_{-0.002}$	$0.006^{+0.002}_{-0.002}$	$0.0024^{+0.0017}_{-0.0016}$	$0.0029^{+0.0009}_{-0.0009}$
$\texttt{brvnei}_1$	kT_1 (keV)	$0.409^{+0.011}_{-0.017}$	$0.431^{+0.006}_{-0.013}$	$0.442^{+0.015}_{-0.013}$	$0.430^{+0.007}_{-0.008}$	$0.341519^{+0.013}_{-0.014}$	$0.389980^{+0.04}_{-0.02}$
	C	$2.0^{+0.9}_{-0.9}$	$7.8^{+3.0}_{-1.8}$	11^{+6}_{-3}	$7.0^{+2.3}_{-1.7}$	31^{+6}_{-6}	< 7
	N	0 (fixed)					
	O	$0.41^{+0.05}_{-0.04}$	$0.58^{+0.16}_{-0.09}$	$0.90^{+0.4}_{-0.2}$	$0.68^{+0.14}_{-0.10}$	$1.40^{+0.15}_{-0.15}$	$0.34^{+0.12}_{-0.09}$
	Ne	$4.1^{+0.4}_{-0.4}$	$7.1^{+1.8}_{-1.0}$	$6.6^{+2.6}_{-1.3}$	$6.1^{+1.1}_{-0.8}$	$12.8^{+1.7}_{-1.7}$	$2.9^{+0.9}_{-0.5}$
	Mg	$5.0^{+0.7}_{-0.6}$	$12.3^{3.1}_{-1.7}$	10^{+4}_{-2}	$11.6^{+2.1}_{-1.3}$	29^{+4}_{-4}	1 (fixed)
	Fe	$51.4^{1.4}_{-5.7}$	93^{+27}_{-15}	100^{+40}_{-20}	109^{+22}_{-16}	275^{+12}_{-9}	70^{+24}_{-15}
	Ni	=Fe					
	τ_1 (10^9cm^{-3} s)	$1.23^{+0.06}_{-0.07}$	$1.41^{+0.05}_{-0.04}$	$1.50^{+0.06}_{-0.05}$	$1.30^{+0.03}_{-0.03}$	$0.993^{+0.05}_{-0.04}$	$1.08^{+0.07}_{-0.07}$
	Velocity (10^4 km s^{-1})	> 0.74	$0.55^{+0.05}_{-0.05}$	0 (fixed)	$0.60^{+0.05}_{-0.05}$	$0.36^{+0.11}_{-0.13}$	$0.65^{+0.17}_{-0.16}$
	EM_1 (10^{56} cm^{-3})	32^{+4}_{-3}	16^{+3}_{-4}	8^{+2}_{-2}	18^{+3}_{-3}	$7.5^{+0.3}_{-0.3}$	$7.4^{+1.8}_{-1.8}$
	kT_2 (keV)	$0.97^{+0.06}_{-0.05}$	$1.32^{+0.06}_{-0.06}$	$1.43^{0.07}_{-0.06}$	$1.23^{+0.06}_{-0.04}$	$1.15^{+0.06}_{-0.03}$	$1.50^{+0.20}_{-0.16}$
	O	42^{+10}_{-9}	20^{+7}_{-6}	27^{+10}_{-8}	33^{+10}_{-9}	11.2175^{+2}_{-2}	30^{+26}_{-26}
	Ne	46^{+10}_{-9}	1 (fixed)		40^{+9}_{-10}	9.00606^{+3}_{-2}	22^{+16}_{-21}
	Mg	58^{+11}_{-12}	61^{+8}_{-10}	72^{+14}_{-17}	69^{+12}_{-15}	$18.4^{+2.2}_{-1.8}$	46^{+16}_{-40}
	Si	180^{+30}_{-60}	230^{+30}_{-40}	270^{+50}_{-70}	280^{+50}_{-70}	114^{+11}_{-9}	300^{+100}_{-270}
	S	290^{+60}_{-90}	380^{+50}_{-60}	470^{+80}_{-90}	480^{+90}_{-90}	183^{+18}_{-16}	450^{+160}_{-390}
$\texttt{brvnei}_2$	Ar	350^{+100}_{-90}	370^{+80}_{-70}	520^{+110}_{-140}	520^{+130}_{-140}	240^{+30}_{-30}	250^{+240}_{-220}
	Ca	> 600	> 800	> 700	> 800	360^{+90}_{-80}	> 100
	Fe	28^{+6}_{-6}	69^{+9}_{-12}	90^{+17}_{-23}	70^{+11}_{-18}	$24.8^{+2.4}_{-0.8}$	1 (fixed)
	Ni	=Fe					
	τ_2 (10^9cm^{-3} s)	57^{+6}_{-6}	43^{+3}_{-3}	36^{+2}_{-2}	$39.9^{+1.8}_{-2.8}$	$38.0^{+1.1}_{-4.4}$	32^{+6}_{-5}
	Velocity (10^4 km s^{-1})	$0.394^{+0.017}_{-0.017}$	$0.533^{+0.014}_{-0.014}$	$0.438^{+0.016}_{-0.015}$	$0.39^{+0.05}_{-0.05}$	$0.480^{+0.014}_{-0.014}$	$0.48^{+0.03}_{-0.04}$
	EM_2 (10^{56} cm^{-3})	$0.121^{+0.003}_{-0.010}$	$0.074^{+0.016}_{-0.008}$	$0.044^{+0.015}_{-0.007}$	$0.068^{+0.022}_{-0.011}$	$0.140^{+0.012}_{-0.012}$	$0.011^{+0.079}_{-0.003}$
	kT_3 (keV)	> 3.91	> 3.98	> 3.97	> 3.95	> 3.96	> 3.88
	Ne	40^{+30}_{-30}			1 (fixed)		
	Si	1 (fixed)		< 50	1 (fixed)		28^{+146}_{-17}
	S	134^{+134}_{-133}			1 (fixed)		
	Ar	600^{+400}_{-400}	< 500	1 (fixed)	< 500	1 (fixed)	
	Ca			1 (fixed)			190^{+470}_{-110}
$\texttt{brvnei}_3$	Fe	> 900	> 800	> 800	> 900	> 970	190^{+720}_{-80}
	Ni	=Fe					
	τ_3 (10^9cm^{-3} s)	$6.49^{0.18}_{0.22}$	$6.78^{+0.12}_{-0.11}$	$6.32^{+0.12}_{-0.11}$	$6.50^{+0.09}_{-0.11}$	$6.31^{+0.13}_{-0.13}$	$6.49^{+0.19}_{-0.21}$
	Velocity (10^4 km s^{-1})	$0.59^{+0.06}_{-0.06}$	$0.53^{+0.04}_{-0.04}$	$0.59^{+0.05}_{-0.05}$	$0.43^{+0.05}_{-0.05}$	$10.51^{+0.06}_{-0.06}$	> 0.9
	EM_3 (10^{56} cm^{-3})	$0.0100^{+0.0006}_{-0.0004}$	$0.0134^{+0.0027}_{-0.0002}$	$0.0099^{+0.0032}_{-0.0002}$	$0.0137^{+0.0024}_{-0.0002}$	$0.0078^{+0.0002}_{-0.0002}$	$0.014^{+0.008}_{-0.011}$
	$\chi^2/d.o.f.$	834.12/662	927.60/713	748.64/644	860.19/681	7748.25/628	545.85/494

Notes. Solar abundances from Anders & Grevesse (1989). τ lower limit set to be 5×10^8 cm^{-3} s. Abundances upper limit is set to be 1000 times the solar one. Velocity upper limit set to be 1×10^4 m s^{-1}. Abundances consistent with their solar values were fixed to 1.

3.4.1 Different regimes of particle acceleration in Kepler's SNR

The cutoff energy parameter ε_0 is a crucial factor in order to characterize the acceleration mechanism in SNRs, because it is determined by the balance between acceleration and cooling in the synchrotron emission process. Zirakashvili & Aharonian (2007) derived

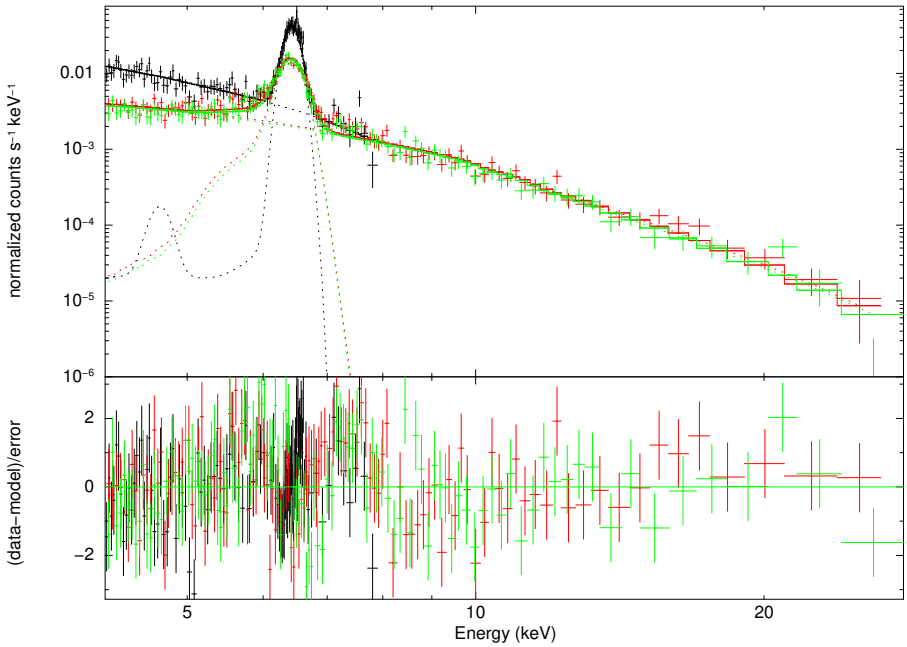

Figure 3.5: EPIC-pn (black), FPMA (red) and FPMB (green) spectra of the hardest knot in Kepler's SNR (cyan circle in Figure 3.1) with the corresponding best-fit model and residual in the 4.1 − 30 keV band.

a relation between ε_0, the Bohm factor and the shock velocity,

$$\varepsilon_0 = \frac{1.6}{\eta}\left(\frac{v_{sh}}{4000 \text{ km s}^{-1}}\right)^2 \text{keV}. \tag{3.1}$$

By adopting the same approach as Tsuji et al. (2021), I show in the left panel of Figure 3.6 the values of ε_0 obtained from the spectral fittings of the regions with a proper motion measurement available either in Katsuda et al. (2008) or in Coffin et al. (2022), as a function of the corresponding v_{sh} (refer to Appendix A.1 for details on selection criteria). I mark with different colors data points derived for southern regions (black) and northern regions (red). In northern regions I obtain, on average, lower shock velocities and higher ε_0 values than in southern regions ($\varepsilon_0^S = 0.48 \pm 0.02$ keV, $\varepsilon_0^N = 0.60 \pm 0.03$ keV, for regions 2-5 and regions 6-9/11, respectively). Moreover, the figure shows that southern and northern regions identify two distinct clusters. This suggests the presence of two different regimes of electron acceleration in the same SNR. If I describe each of

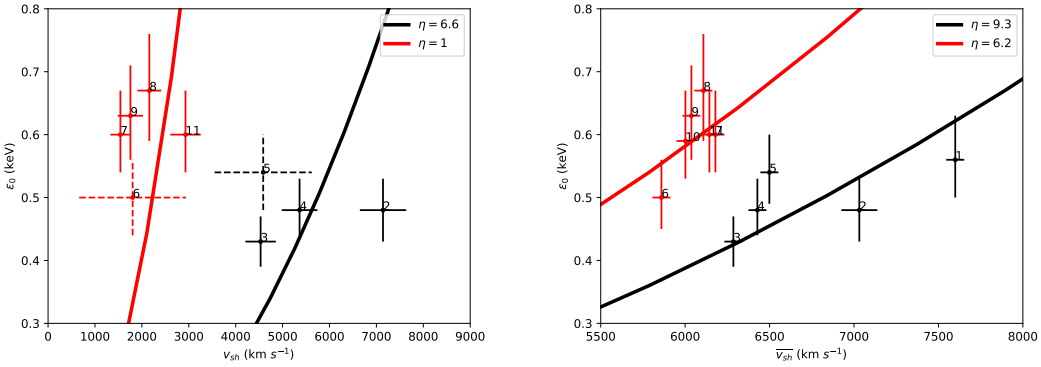

Figure 3.6: *left panel:* Synchrotron cutoff energy vs. current shock velocity derived from Coffin et al. (2022), (solid crosses) and Katsuda et al. 2008 (dashed crosses, see Appendix A.1 for details). Red crosses mark northern regions (6-9/11) and the red solid curve is the corresponding best-fit curve obtained from Equation 3.1. Black crosses mark southern regions (2-5) and the black solid curve is the corresponding best-fit curve obtained from Equation 3.1. *right panel:* Synchrotron cutoff energy vs. average shock speed for Kepler's SNR. Red crosses mark regions 6-11, and the red solid curve is the corresponding best-fit curve obtained from Equation 3.1. Black crosses mark regions 1-5, and the black solid curve is the corresponding best-fit curve obtained from Equation 3.1.

the two clusters with Equation 3.1, I can derive the corresponding best fit values of the Bohm diffusing factor, obtaining $\eta = 6.6 \pm 1.6$ in the south and reaching the Bohm limit in the north. These values are similar to those derived by Tsuji et al. (2021), who find $\eta \sim 0.3 - 4$. However, Tsuji et al. (2021) adopted a distance of 4 kpc (instead of 5 kpc) to derive the shock velocity from the proper motion measurements, thus obtaining lower velocities than those reported in the left panel of Figure 3.6, which is in line with their lower values of η.

Taking into account these results, I can estimate the acceleration time of electrons as described in Equation 1.23. Considering $\delta = 0.5$ and taking the values I found in the northern shell ($v_{sh} = 1800$ km s^{-1}, $\eta = 1$ and $\varepsilon_0 = 0.64$ keV), I derive $t_{acc} \approx 300 \cdot \left(\frac{B}{100\mu\text{G}}\right)^{-\frac{3}{2}}$ yr. Such a high value of the acceleration time may suggest that the electrons started to accelerate before the interaction of the shock with the CSM, which produced a deceleration of the northern shock front. Aharonian & Atoyan (1999) suggested that the shock velocity should be larger than 2000 km s^{-1} to emit synchrotron X-rays (see also Vink 2008). Thus the existence of synchrotron X-rays implies that the deceleration started recently. Similar situation happens in a super-bubble with synchrotron X-rays, 30 Dor C (Bamba et al. 2004), where the supernova shock just

hit the shell of the super-bubble and emit synchrotron X-rays (Yamaguchi et al. 2009) although Lopez et al. (2020) suggests the super-bubble itself accelerate electrons.

In this framework, the current shock velocity may not be representative of the shock conditions over the whole acceleration process. I then explore an alternative scenario, by studying the relationship between the synchrotron cutoff energy and the average shock velocity, $\overline{v_{sh}}$ in all the regions selected for my spatially resolved spectral analysis. I derived $\overline{v_{sh}}$ for each region as $\overline{v_{sh}} = r_{sh}/t_{age}$, where r_{sh} is the radius of the shock. I estimated r_{sh} for regions 1-11 by measuring the distance between the shock front and the center of the remnant (whose position was carefully derived by Sato & Hughes 2017). The measuring procedure was performed detecting the edge at the azimuthal center of each region on the *Chandra* flux image in the $4.1 - 6$ keV band, to exploit the high spatial resolution of the *Chandra* mirrors (I associated to the angular distance an error of 1.5").

Figure 3.6 (*right panel*) shows the values of ε_0 obtained from the spectral fittings of the eleven regions analyzed, as a function of the corresponding $\overline{v_{sh}}$. Again, in northern regions I obtain, on average, lower shock velocities and higher ε_0 values than in southern regions ($\varepsilon_0^S = 0.48 \pm 0.02$ keV, $\varepsilon_0^N = 0.59 \pm 0.02$ keV, for regions 1-5 and regions 6-11, respectively). Moreover, also in this plot, southern and northern regions clearly identify two distinct clusters. Therefore, by adopting the average shock velocities, I recover the presence of two different regimes of electron acceleration in the Kepler's SNR. Each of the two clusters can be well described by Equation 3.1 with a specific value of η. I then derive the corresponding best fit values of the Bohm diffusing factor, obtaining $\eta = 9.3 \pm 0.4$ in the north and $\eta = 6.2 \pm 0.2$ in the south, with a null hypothesis probability of $\sim 90\%$. These values of η are higher than those derived with the current shock velocities. This is because the deceleration of the shock front makes the current velocities systematically lower than the average velocities (see Equation 3.1 for the dependence of η on v_{sh}). Therefore, the values of the Bohm factors should be taken with some caution.

The two scenarios considered above, namely synchrotron emission originating from i) electrons accelerated in the current shock conditions (i. e., freshly accelerated electrons in a high magnetic field) and ii) electrons accelerated well before the interaction with the dense CSM at north (i. e., longer acceleration times, possibly associated with a lower magnetic field, as in Nagayoshi et al. 2021), may be considered as two limiting cases, bracketing the actual evolution of the system.

Nevertheless, regardless of the shock velocity adopted (current velocity vs. average velocity), my conclusions do not change, since both the plots shown in Figure 3.6 point toward a more efficient (i.e. closer to the Bohm limit) electron acceleration in the north than in the south.

On the other hand, a scenario in which ε_0 does not depend on the shock velocity is also possible. I tested this possibility by fitting the data points of Figure 3.6 with a constant ε_0, and obtained a null hypothesis probability of $\sim 15\%$, which is well below

the value obtained in the loss-limited case, but still statistically acceptable. However, a framework where ε_0 does not depend on v_{sh} would indicate that the maximum electron energy is not limited by radiative losses and, as explained in Section 3.1, this would imply a magnetic field lower than 30 μG (assuming ε_0=0.5 keV), which is at odds with the observations (Völk et al. 2005, Parizot et al. 2006, Rettig & Pohl 2012, Reynolds et al. 2021).

The cutoff energies discussed above were obtained by assuming that the X-ray continuum above 4 keV is ascribed to synchrotron radiation. I then checked how a possible contamination of thermal emission in the hard X-ray spectra of northern regions (where thermal emission is the highest) affects my results. I found that if I model the hard continuum of regions 6-11 with a combination of synchrotron radiation and thermal bremsstrahlung, the value of ε_0 systematically increases with the contribution of thermal emission. The values of ε_0 for regions 6-11 shown in Table 3.2 and Figure 3.6 should then be considered as lower limits. This means that the acceleration efficiency in the north may be even higher (and the Bohm diffusing factor lower) than that derived by neglecting the contribution of thermal emission to the hard X-ray continuum. I conclude that the evidence of more efficient acceleration in the northern part of Kepler's SNR is solid. Southern regions, where the thermal emission has a lower surface brightness, are less affected by thermal contamination and the synchrotron component is better constrained. I note that Tsuji et al. (2021) finds small-scale variations in ε_0, with local peaks reaching values of the order of 1.5 keV (higher than those reported in my Table 3.2). This may be due to the absence of *NuSTAR* data for Kepler's SNR in Tsuji et al. (2021) and to the different size of the extraction regions (my regions being significantly larger than theirs).

I note that in the southern part of Kepler's SNR, where the ambient density is similar to that observed in Tycho's SNR (Blair et al. 2007), I recover similar results as those obtained for Tycho's SNR by Lopez et al. (2015), who found that the cutoff energy increases with the shock velocity (i.e., where the ambient density is low). At odds with Tycho's SNR, however, Kepler's SNR is interacting with a much denser environment in the north (4-7 times denser, Blair et al. 2007; Katsuda et al. 2008), where I register a different regime of particle acceleration.

The presence of two different acceleration regimes and of a higher acceleration efficiency in regions 6-11 might be explained by considering the turbulent magnetic field generated in the interaction between the shock front and the dense CSM in the north. Inoue et al. (2012) modelling RX J1713.7-3946 SNR with a 3D magneto-hydrodynamic (MHD) simulation, show that a shock wave that sweeps a cloudy medium generates an amplified magnetic field, as a result of the dynamo action induced by the turbulent shock-cloud interaction (See also Orlando et al. 2008). An amplified magnetic field may lead toward a more efficient acceleration process and to a lower η Bohm factor. This interpretation is in line with the findings obtained for RX J1713.7-3946 by Sano et al.

(2015), who observed that the synchrotron photon index is anti-correlated with the X-ray intensity. Indeed, I found the highest value of ε_0 in the "Hard Knot" region, which I identified in the northern part of the shell as a bright feature in the 15 – 30 keV map (see Figure 3.1 and Table 3.2). In general, my findings show that in Kepler's SNR the ε_0 parameter is high in the region where the shock interacts with high density CSM, thus indicating a similar scenario as that proposed for RX J1713.7-3946.

3.4.2 Spectral Energy Distribution

Several SNRs are known to emit γ-rays up to TeV energy (e.g.Ackermann et al. 2013, H. E. S. S. Collaboration et al. 2018, Aleksić et al. 2012). Xiang & Jiang (2021) reported a likely detection (with $\sim 4\sigma$ significance) of γ-ray emission in the 0.2 – 500 GeV band from the region of Kepler's SNR by analyzing Fermi Large Area Telescope (LAT) data. Using the same Fermi LAT data, Acero et al. (2022) confirmed this detection up to 6.0σ. Moreover, H. E. S. S. Collaboration et al. (2022) reported the detection of VHE emission from Kepler's SNR based on a deep observation of the High Energy Stereoscopic System (H.E.S.S.).

In this section, I model the SED of Kepler's SNR for the non-thermal emission, using radio (DeLaney et al. 2002), X-ray (*NuSTAR* FPMA and FPMB in the 8 – 30 keV band from this work and HXD-PIN from Nagayoshi et al. 2021), GeV (Acero et al. 2022) and TeV H. E. S. S. Collaboration et al. (2022) data, and give some constraints on the particle energy distribution, and on the ambient density and magnetic field.

I use the radiative code `naima` (version 0.9.1, Zabalza 2015) to model the SED. I considered a lepto-hadronic one-zone stationary model to describe the multi-band emission spectrum. In this model, the synchrotron and IC emission are assumed to stem from the same electron distribution, which is described by a power-law with an exponential cutoff. I considered the same seed photon field as Nagayoshi et al. (2021) for the IC emission: the CMB radiation, a FIR component (T = 29.5 K and u_{FIR} = 1.08 eV cm^{-3}), and a NIR component (T = 1800 K and u_{NIR} = 2.25 eV cm^{-3}). As for the hadrons, I assumed a power law energy distribution with an exponential cutoff. The model that best reproduces the observed data is shown in Figure 3.7 (left panel).

My model gives for the leptonic part a spectral index α = 2.44 and a cutoff energy E_{cut} = 16 TeV. The electrons emit synchrotron radiation in a magnetic field of 100 μG. For the hadronic part I assumed the same spectral index and an energy cutoff of 500 TeV. The total kinetic energy of protons (W_p), interacting with a post shock medium with density of 20 cm^{-3} (consistent with density value of the shock-CSM interacting region, Kasuga et al. 2021), was set to be 15 times the electrons total kinetic energy ($W_p = 4.2 \times 10^{48}$ erg). As a comparison I also modeled the SED using the value for the magnetic field proposed by Nagayoshi et al. 2021 (B=40 μG, see Figure 3.7 right panel), with α = 2.44 and E_{cut} = 35 TeV for the leptonic part. For the hadronic part of the model I adopted the same assumption as before but with $W_p = 5.4 \times 10^{48}$ erg (4 times

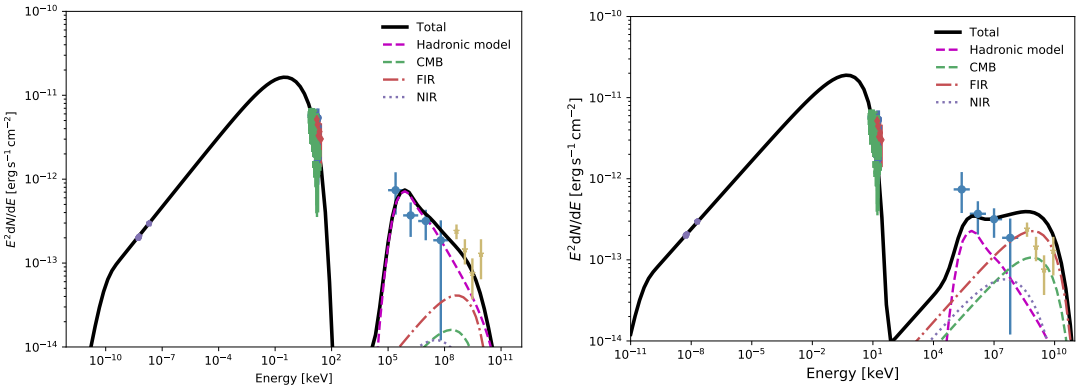

Figure 3.7: *Left panel:* Spectral Energy Distribution of Kepler's SNR. Radio data (violet) are from DeLaney et al. (2002), NuSTAR (FPMA and FPMB, blue and green respectively) X-ray data are extracted from the whole remnant, HXD-PIN X-ray data (dark red) are from Nagayoshi et al. (2021), GeV γ-ray data (steel blue) are from Acero et al. (2022) and TeV γ-ray data (yellow) are from H. E. S. S. Collaboration et al. (2022). The black curve indicates my combined lepto-hadronic model, including contributions from π^0 decay (dashed magenta curve), and Inverse Compton emission from the cosmic microwave background (green dashed curve), far-infrared (red, dash-dotted curve) and near-infrared emission (purple dotted curve). In the lepto-hadronic model, the magnetic field is 100 μG and the post shock density is 20 cm^{-3}. *Right panel:* Same as left panel, but with a magnetic field of 40 μG and a post shock density of 5 cm^{-3}.

the electrons total kinetic energy) and a post shock medium density of 5 cm^{-3}. This last case gives a poor fit compared with the case where the magnetic field is higher.

3.5 Conclusions

I analyzed an archive *NuSTAR* observation of Kepler's SNR. I detected hard X-ray emission up to $\sim$ 30 keV, mainly stemming from the northern part of the remnant, where the shock front is interacting with dense circumstellar material. I verified that the bulk of the hard X-ray emission is non-thermal and performed a spatially resolved spectral analysis focusing on the outer rim of the shell by combining *NuSTAR* and *XMM-Newton* spectra. I adopted the loss-limited synchrotron emission model by Zirakashvili & Aharonian (2007) to determine the cutoff photon energy parameter in 11 regions. I identified two different acceleration regimes in the northern and southern limbs of Kepler's SNR. In particular, I found lower Bohm factors (i.e. more efficient electron acceleration) in the northern part of the shell than in the south. I suggest that the

interaction of the shock front with the high density CSM at north generates an amplified, possibly turbulent, magnetic field, which facilitates the particle acceleration process.

An alternative scenario of constant cutoff energy across the shell of Kepler's SNR is disfavored by my analysis. This would imply that the maximum electron energy is not limited by radiative losses (which would require that the magnetic field is much smaller than that observed), though it cannot be statistically excluded.

I produced the spectral energy distribution including also *NuSTAR* X-ray data. I were able to reproduce all the data with a lepto-hadronic model with a magnetic field of 100 μG, a medium density of 20 cm^{-3}, electron energy $W_e = 2.7 \times 10^{47}$ erg and proton energy $W_p = 4.2 \times 10^{48}$ erg. The density I found in modeling the SED is consistent with that derived in the northern region by Kasuga et al. (2021), suggesting a scenario in which the majority of the hadronic emission originates in the northern part of the remnant. The bright non-thermal hard X-ray emission that I detected in the northern half of Kepler's SNR strongly suggests that this region is also site of leptonic emission. Further insights on the morphology and the spectral characteristics of the γ-ray emission from Kepler's SNR will be provided by the next generation of γ-ray telescopes such as the Cherenkov Telescope Array Observatory (CTAO), which will enhance by order of magnitudes the spatial and spectral resolution of the γ-ray observatories

4

Unraveling the Effects of Dense Medium on a Near to Bohm-Limit Acceleration in Kepler's SNR

Abstract

The maximum energy of electrons in SNR shocks is limited by radiative losses, where the synchrotron cooling time equals the acceleration time. Conversely, slower shock speeds in dense mediums increase the acceleration time, leading to lower maximum electron energies and fainter X-ray emissions. In Kepler's SNR, an enhanced electron acceleration, which proceeds near the Bohm limit, occurs in the north of its shell, where the shock is slowed by a dense CSM. To investigate whether this scenario still holds at smaller scales, I analyzed the temporal evolution of synchrotron flux in filamentary structures using the two deepest *Chandra*/ACIS X-ray observations in 2006 and 2014. I examined spectra from different filaments in the northern shell. I measured proper motion and calculated the ratio of acceleration to synchrotron time-scales. The interaction with the turbulent and dense northern CSM induces competing effects on electron acceleration, with reduced electron mean free path and Bohm factor enhancing acceleration efficiency, but lower shock velocity increasing the acceleration time-scale. In most filaments, these effects compensate each other, but in one region the acceleration time-scale exceeds the synchrotron time-scale, resulting in a significant decrease in nonthermal X-ray emission from 2006 to 2014, indicating fading synchrotron emission. My findings provide a coherent understanding of the different regimes of electron acceleration observed in Kepler's SNR through various diagnostics.

The work presented in this Chapter has been submitted under the title "*Unraveling the Effects of Dense Medium on a Near to Bohm-Limit Acceleration in Kepler's SNR*" in the scientific journal "The Astrophysical Journal". Part of this work was published

in the Proceedings (PoS) of the 38^{th} International Cosmic Ray Conference (ICRC2023; Sapienza 2023; DOI: https://doi.org/10.22323/1.444.0843).

4.1 Introduction

SNRs are prominent accelerators of particles, thus they are widely considered the primary origin of galactic cosmic rays. The first observational evidence of very high energy ($E > 10^{12}$ eV) electrons accelerated at SNR shocks was discovered by Koyama et al. (1995), who detected nonthermal X-ray emission stemming from SN 1006 (where also efficient hadronic acceleration has been reported, e. g., Giuffrida et al. 2022). Indeed, the outer shells of young SNRs typically emit synchrotron radiation in the X-ray band, which can be used as a diagnostic tool to deepen our understanding of the acceleration process. The study of X-ray synchrotron emission can provide information about the shape of the electron energy distribution and the mechanism that limit the maximum energy that electrons can reach (e. g., Miceli et al. 2013a).

Kepler's SNR, as already discussed in Chapter 3, is the aftermath of the explosion of the historical type Ia SN 1604 at $d \approx 5$ kpc from us. I will adopt $d = 5$ kpc also throughout this Chapter.

Kepler's SNR is an interesting object to study the acceleration process, in order to understand how the environment affects the acceleration mechanism. The remnant is indeed interacting with a dense nitrogen-rich CSM cloud in the north (Reynolds et al. 2007, Katsuda et al. 2015, Kasuga et al. 2021). Prominent particle acceleration in Kepler's SNR is testified by its energetic non-thermal emission. The presence of non-thermal X-ray emission in Kepler's SNR was first discovered in its south-eastern region by Cassam-Chenaï et al. (2004). Recently, Nagayoshi et al. (2021) reported the first strong detection of hard X-ray emission within the 15-30 keV band from Kepler's SNR, by analyzing a *Suzaku* HXD observation.

In a recent study, (Tsuji et al. 2021) analyzed the cutoff photon energy (ε_0) of synchrotron radiation across different regions of several SNRs, including Kepler's SNR. To this end, the authors used a model of synchrotron emission, originally proposed by Zirakashvili & Aharonian (2007), where the electron maximum energy is limited by radiation losses. In this scenario, ε_0 is related to the shock speed according to the Equation 3.1. The spatially resolved analysis of Kepler's SNR by Tsuji et al. (2021), lacked of the hard part of the spectrum, so no clear correlation between the shock velocity and the synchrotron cutoff energy was found, except for the synchrotron dominated regions.

In the work presented in the previous Chapter (Sapienza et al. 2022, Chapter 3), by making use of *NuSTAR* and *XMM-Newton* data, I performed a spatially resolved spectral analysis of Kepler's SNR, using the hard part of the X-ray spectrum where the emission is dominated by synchrotron radiation. The spectra were analyzed by adopting the loss-

Table 4.1: *Chandra* observations table.

Obs ID	Exp. Time (ks)	R. A.	Dec.	Start Date
6714	157.8	$17^h\ 30^m\ 42.0^s$	-21°29' 00.0"	27/04/2006
6715	159.1	$17^h\ 30^m\ 41.2^s$	-21°29' 31.4"	03/08/2006
6716	158.0	$17^h\ 30^m\ 42.0^s$	-21°29' 00.0"	05/05/2006
6717	106.8	$17^h\ 30^m\ 41.2^s$	-21°29' 31.4"	13/07/2006
6718	107.8	$17^h\ 30^m\ 41.2^s$	-21°29' 31.4"	21/07/2006
7366	51.5	$17^h\ 30^m\ 41.2^s$	-21°29' 31.4"	16/07/2006
16004	102.7	$17^h\ 30^m\ 41.2^s$	-21°29' 31.4"	13/05/2014
16614	36.4	$17^h\ 30^m\ 41.2^s$	-21°29' 31.4"	16/05/2014

limited model. I identified two different regimes of particle acceleration, characterized by different Bohm factors. In the north, where the shock interacts with a dense CSM, I found a more efficient acceleration (i.e., lower Bohm factor) than in the south, where the shock velocity is higher and there are no signs of shock interaction with dense CSM. This can be explained by considering that the interaction of the shock front with the dense CSM at north is associated with a turbulent magnetic field, which boosts the particle acceleration process. On the other hand, the low shock speeds measured in the north (Katsuda et al. 2008; Coffin et al. 2022) leads to a high acceleration time scale (~300 yrs), which can result in a decrease of the maximum electron energy by radiation losses. To unravel this intricate scenario on smaller scales I studied the evolution of the synchrotron flux in several filaments of Kepler's SNR, making use of the two deepest set of *Chandra*/ACIS observations performed in 2006 and 2014.

This Chapter is organized as follows: in Section 4.2 I present the datasets and the data reduction process, whereas in Section 4.3 I show the results obtained from the spectral analysis. Discussions and conclusion are drawn respectively in Section 4.4 and in Section 4.5.

4.2 Observation and Data Reduction

For my analysis I made use of different *Chandra*/ACIS observations for two epochs, namely 2006 and 2014, as summarized in Table 4.1. Data were analyzed with the CIAO v4.13 software, using CALDB 4.9.4. I reprocessed the data by using the `chandra_repro` task. I mosaicked flux images for each year by using the `merge_obs` task. In order to measure proper motion, I followed the same astrometric alignment procedure described by Coffin et al. (2022), selecting the same point sources (also highlighted in yellow in Figure 4.1). For the proper motion measurement only, I use the deep 2006 observation (Obs. ID: 6715) as the relative reference to which I aligned the 2014 deepest observation (Obs. ID: 16004), in order to minimize systematic errors in the reprojections. To extract

spectra, I used the `specextract` CIAO command. I then combined the spectra from the same epochs by using the `combine_spectra` CIAO command. The spectra were rebinned by using the optimal binning algorithm (Kaastra & Bleeker 2016). Spectral analysis was performed on XSPEC v. 12.11.1 Arnaud (1996). I adopted the Cash statistic (C-stat) for the fitting procedure.

4.3 Results

4.3.1 Spectra

For my spatially resolved spectral analysis I consider only regions characterized by:

i) a bright synchrotron emission;

ii) a sharp edge in the radial distribution of surface brightness (see Bamba et al. 2005);

iii) low contamination from thermal emission.

I identify 6 filamentary regions in the northern part of Kepler's SNR that are clearly visible in the 4.1 − 6 keV energy band, were the synchrotron radiation dominates the emission, and are located at the rim of the shell. These regions are shown in red in Figure 4.1 and labeled as 1 − 6. As a comparison, I also consider 3 regions in the south (shown in white and labeled as 7 − 9 in Figure 4.1).

The source spectra were fitted by adopting the loss-limited model proposed by Zirakashvili & Aharonian (2007), to describe the synchrotron emission, and a component from optically thin plasma in non-equilibrium of ionization (`vnei`) to account for the residual thermal emission (plus 2 Gaussian components to take in account the missing Fe L lines in the model, as in Chapter 3, see also Katsuda et al. 2015 and Sapienza et al. 2022). I modeled the background by a phenomenological fitting of the spectrum extracted from the green region in Figure 4.1. The background model (properly scaled to account for the different areas of the extraction regions) was then added to the source model. From the best-fit model of each region, I computed the flux in the 4.1 − 6 keV band by using the `cflux` convolution model[1]. I note that in the 4.1 − 6 keV band the flux is dominated by the nonthermal component, whose contribution is always > 90% of the total in each region (see also Figure 4.2 and 4.3). The best-fit parameters for 2006 and 2014 are shown in Table 4.2, while the spectra with the best-fit model and residuals are shown in Figure 4.2 and Figure 4.3.

[1] In the `cflux` model, the normalization of one of the additive models must be fixed to a non-zero value (https://heasarc.gsfc.nasa.gov/xanadu/xspec/manual/node289.html), so I fixed the normalization of the thermal component.

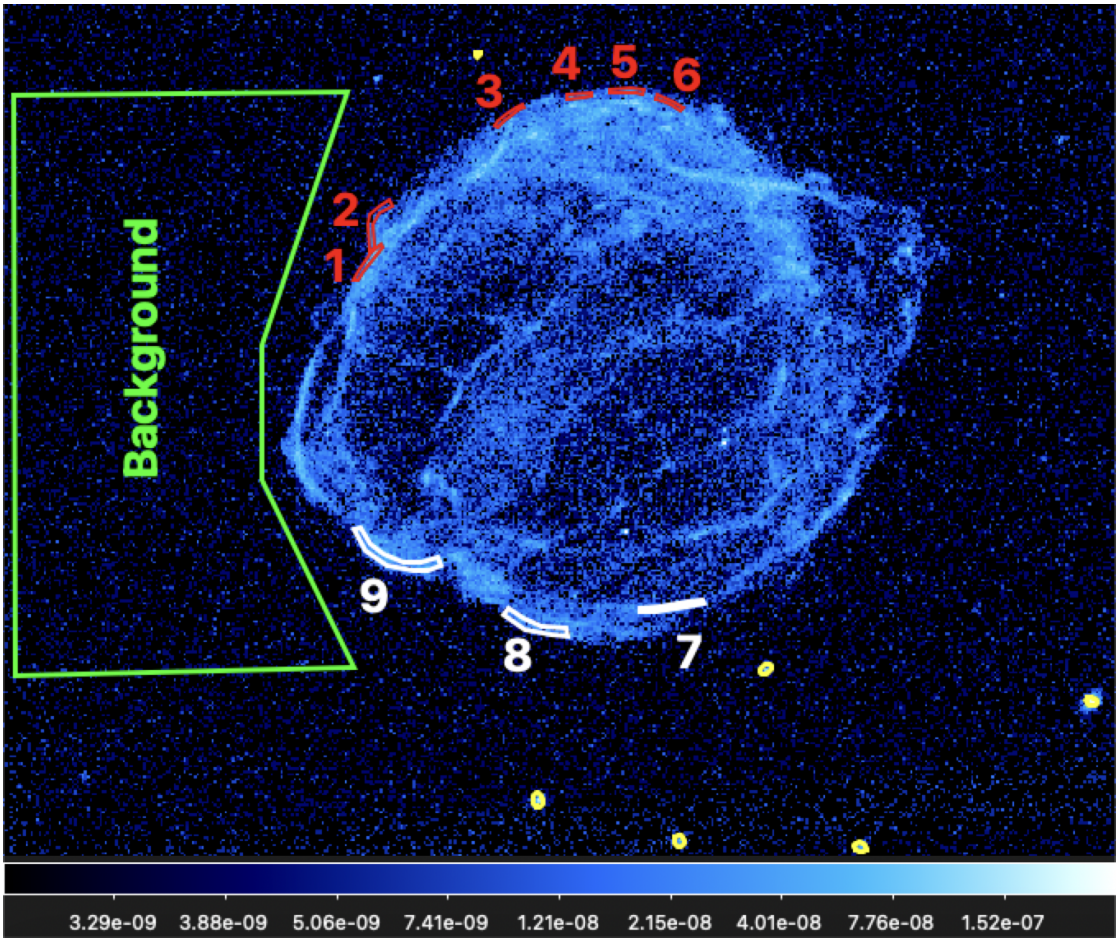

Figure 4.1: *Chandra* flux map of Kepler's SNR in the 4.1 – 6 keV band. Source regions are marked with red polygons for the north and white polygons for the south. The background region is marked with a green polygon, while yellow ellipses indicate the point sources used for the astrometric alignment (as in Coffin et al. 2022).

4.3.2 Shock velocity measurement

To estimate of the shock velocity, I measured the proper motion from 2006 to 2014 in all the nine regions. I mirrored the methodology adopted by Katsuda et al. (2008), where a deeper description of the procedure can be found. I extract the one dimensional radial counts profiles of each filament from both 2006 and 2014 epochs. The profiles were extracted using *Chandra*/ACIS events file with 0.492" pixel. Each profile was then remapped into a 40 times denser grid using a quadratic interpolation, in a similar fashion to Williams et al. (2016). The square root of the counts was taken as statistical

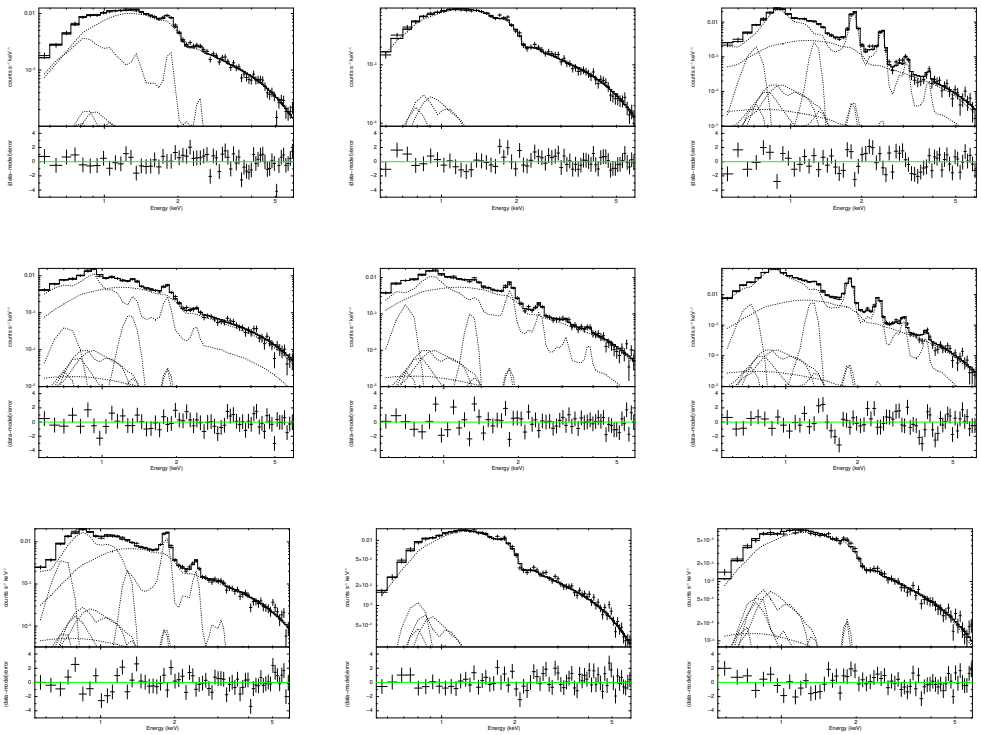

Figure 4.2: Spectra extracted from the regions in Figure 4.1 with best-fit models and residuals for the year 2006

uncertainty. I then shifted the 2014 profile relative to the 2006 profile, minimizing the value of χ^2. Figure 4.4 shows an example of the radial count profiles (for region 2) before and after the shifting procedure. In this Chapter, I only report the statistical errors, which are the 90% confidence limits resulting from a χ^2 increase $\Delta\chi^2 = 2.706$. Once obtained the best-fit value for the angular shift (θ), one can derive the shock velocities for each region (assuming a distance $d = 5$ kpc, as stated in Section 3.1). The shock velocities with their uncertainties are also reported in Table 4.2.

4.4 Discussion

4.4.1 Cut-off photon energy ε_0 vs. the shock speed V_{sh}

By employing the same methodology outlined in my previous work, deeply described in Chapter 3 (Sapienza et al. 2022), I present in Figure 4.5 the values of ε_0 for the two epochs analyzed: 2006 (left panel) and 2014 (right panel; listed in Table 4.2) as a

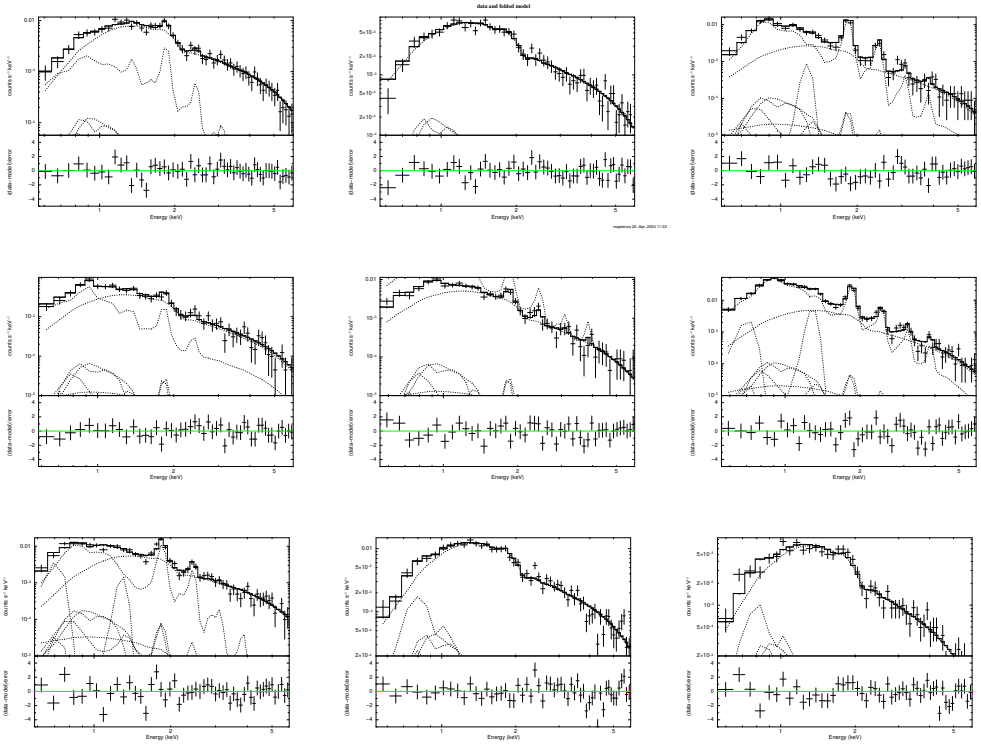

Figure 4.3: Spectra extracted from the regions in Figure 4.1 with best-fit models and residuals for the year 2014

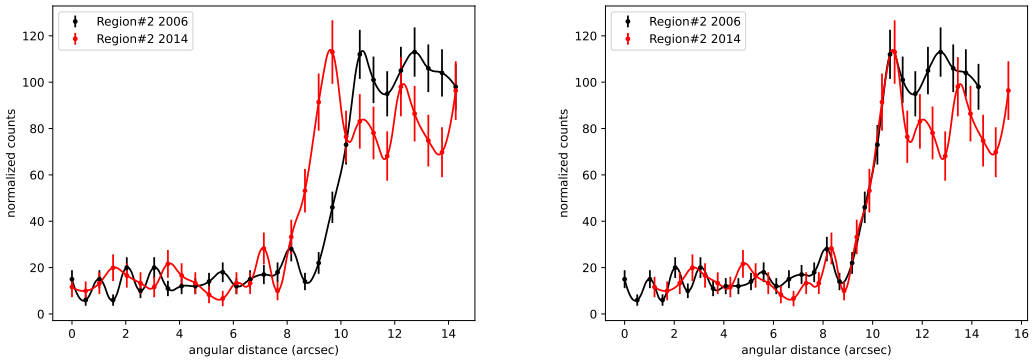

Figure 4.4: *Left panel:* Example of the one dimensional radial count profile for region 2 in 2006 (in black) and in 2014 (in red). *Right panel:* same as the left panel, but with the 2014 profile shifted according to the procedure described in Williams et al. (2016).

Table 4.2: Best-fit parameters for the regions shown in Figure 4.1.

Region #	ε_0 (keV)		Flux 4.1 – 6 keV ($\mathrm{Log_{10}}$ erg cm^{-2} s^{-1})		V_{sh} (km s^{-1})
	2006	2014	2006	2014	
1	$0.50^{+0.04}_{-0.04}$	$0.9^{+0.3}_{-0.2}$	-13.742 ± 0.014	-13.68 ± 0.03	3570 ± 100
2	$0.73^{+0.07}_{-0.06}$	$0.80^{+0.23}_{-0.16}$	-13.808 ± 0.014	-13.81 ± 0.03	4690 ± 120
3	$0.45^{+0.07}_{-0.05}$	$0.41^{+0.18}_{-0.10}$	-14.36 ± 0.03	-14.33 ± 0.07	3690 ± 50
4	$0.34^{+0.04}_{-0.03}$	$0.38^{+0.14}_{-0.09}$	-14.17 ± 0.02	-14.21 ± 0.05	1870 ± 70
5	$0.35^{+0.04}_{-0.04}$	$0.19^{+0.05}_{-0.03}$	-14.19 ± 0.02	-14.42 ± 0.06	1520 ± 100
6	$0.218^{+0.019}_{-0.017}$	$0.23^{+0.06}_{-0.04}$	-14.22 ± 0.02	-14.20 ± 0.06	1590 ± 60
7	$0.32^{+0.03}_{-0.02}$	$0.51^{+0.16}_{-0.10}$	-13.963 ± 0.018	-13.89 ± 0.04	4160 ± 70
8	$1.07^{+0.12}_{-0.10}$	$0.89^{+0.24}_{-0.16}$	-13.499 ± 0.011	-13.51 ± 0.03	7690 ± 70
9	$0.43^{+0.04}_{-0.03}$	$0.36^{+0.07}_{-0.05}$	-13.988 ± 0.018	-13.96 ± 0.04	6000 ± 100

Notes. Errors for ε_0 and flux are at the 68% confidence level. Errors for shock velocity are at 90% confidence level.

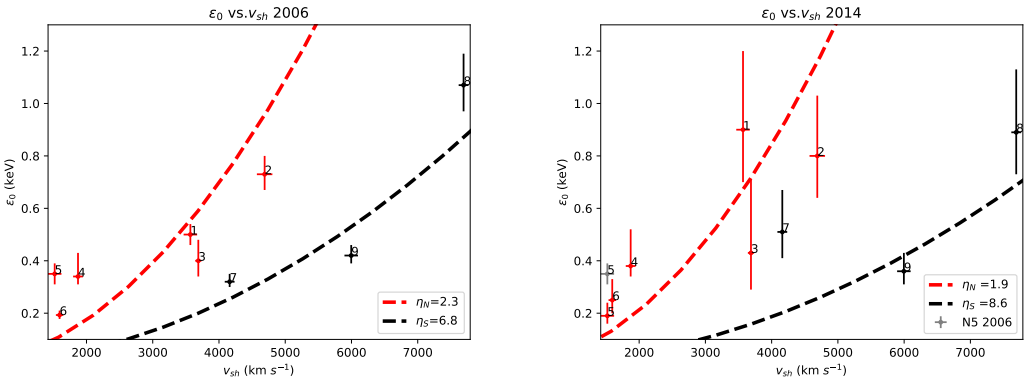

Figure 4.5: Synchrotron cutoff energy vs. current shock velocity for the year 2006 (*left panel*) and for the year 2014 (*right panel*). Red crosses mark northern regions (1-6) and the red dashed curve is the corresponding best-fit curve obtained from Equation 3.1. Black crosses mark southern regions (7-9) and the black dashed curve is the corresponding best-fit curve obtained from Equation 3.1. The gray cross in the right marks region 5 in 2006.

function of their corresponding shock velocity (v_{sh}). I assumed the same shock velocity for the two epochs. I use different colors to distinguish between data points derived from southern regions (in black) and northern regions (in red).

The Figure 4.5 clearly illustrate the separation of the data points into two distinct clusters (in both epochs), representing the southern and northern regions. This result clearly confirms the existence of two distinct regimes of electron acceleration within the same SNR, already identified in Chapter 3. By fitting each of these two clusters using Equation 3.1, I can derive the corresponding best-fit values of the Bohm factor. For the southern regions, the retrieved Bohm factors are $\eta_S = 6.8 \pm 1.1$, in 2006, and $\overline{\eta}_S = 8.6 \pm 2.0$, in 2014. As for the northern regions, the corresponding Bohm factors are $\eta_N = 2.3 \pm 0.4$ in 2006 and $\overline{\eta}_N = 1 - 3.7$ in 2014. The best-fit values of the Bohm factors align well with the values obtained in the previous Chapter (see Section 3.4), further strengthening the evidence that the electron acceleration proceeds much closer to the Bohm limit in the north than in the south. In particular, $\eta_S/\eta_N = 3.0 \pm 0.7$ and $\overline{\eta}_S/\overline{\eta}_N = 3.6 \pm 2.0$ in 2006 and 2014, respectively.

4.4.2 Synchrotron Losses vs. Acceleration Time Scale

Comparing the acceleration time scale to the synchrotron losses time scale is crucial for determining if the acceleration mechanisms can effectively counteract particle losses, thereby indicating whether the region under investigation follows a loss-limited scenario. The acceleration time of electrons is given by Equation 1.23 (Malkov & Drury 2001; Vink 2020). The synchrotron cooling time is given by Equation 1.28. I can derive the ratio τ_{acc}/τ_{sync} which does not depend on the magnetic field, but depends on v_{sh}, ε_0, η (the Bohm factor), and δ, a parameter which accounts for the energy dependence of the diffusion coefficient, and typically ranges between 0.3 and 0.7 (see Strong et al. 2007). Since I here assume an energy independent (and rigidity independent) Bohm factor, I have $\delta = 1$ by definition. I estimated the lower limit of the ratio τ_{acc}/τ_{sync} for each region by putting $\delta = \eta = 1$ and propagating the errors associated with v_{sh} and ε_0. Results are shown in Figure 4.6.

The figure shows that, except for region 5, the acceleration time scale at the Bohm limit is always shorter than the synchrotron cooling time, i. e., in these regions loss-limited conditions ($\tau_{acc}/\tau_{sync} = 1$) can be achieved with $\eta \geq 1$. In particular, in agreement with what I have discussed so far, loss-limited conditions are achieved with the values of η_S and η_N reported in Section 4.4.1 (see also Figure 4.5). In this case, I expect a steady synchrotron flux and no significant variations in the nonthermal emission between 2006 and 2014.

On the other hand, I find that in region 5 the ratio τ_{acc}/τ_{sync} is significantly larger than 1, whatever the Bohm factor. This means that the acceleration time scale is way longer than the synchrotron cooling time, so the electrons in this regions are cooling faster than they are accelerating. I then expect the synchrotron flux of this region to

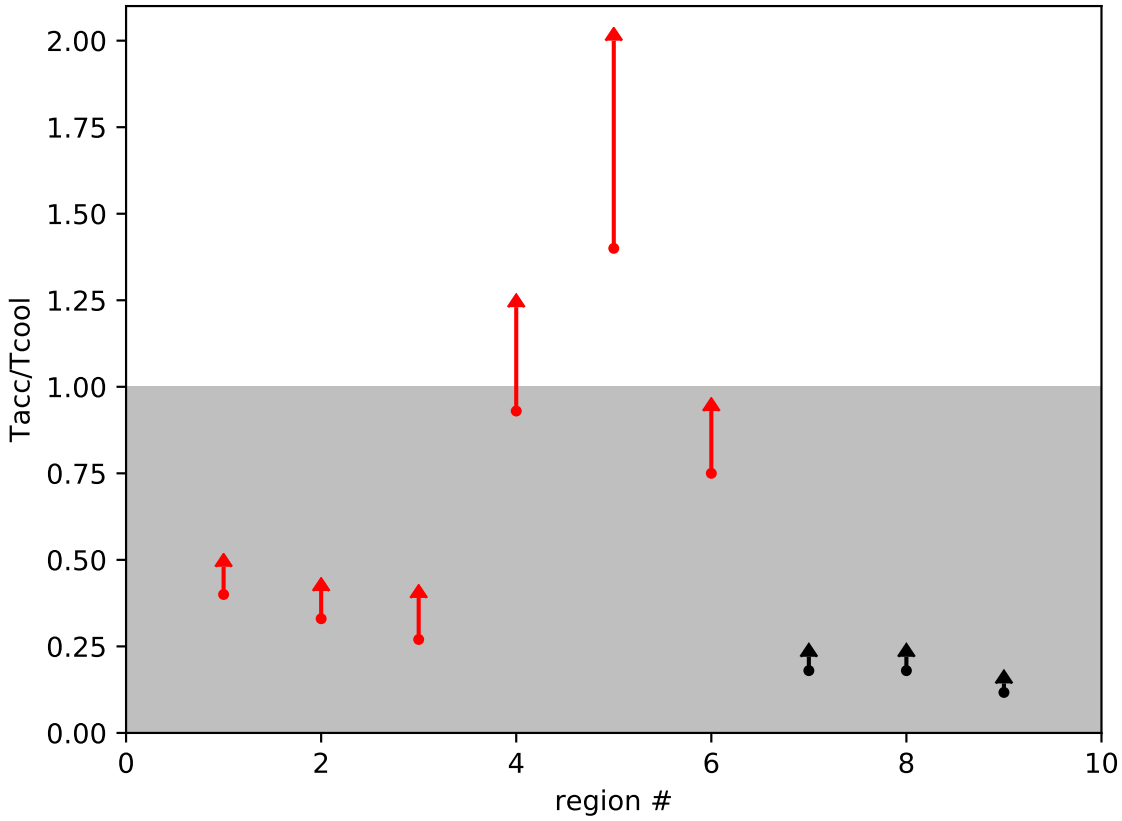

Figure 4.6: Lower limit of the ratio between the acceleration time scale and the synchrotron losses time scale, for the selected region.

decrease with time. Figure 4.6 also shows a sort of trend for regions 4, 5 and 6, which exhibit higher ratios compared to other regions. This could be suggestive that these regions may be entering a phase where the acceleration mechanisms are less efficient at counteracting particle losses. Consequently, the synchrotron flux in these regions may decrease over future epochs and might be monitored by future observations.

4.4.3 Flux Variability

In Figure 4.7, I illustrate the ratio of the synchrotron flux (4.1 – 6 keV) in 2014 to that in 2006 for the northern regions (1 – 6, in red) and the southern regions (7 – 9, in black). Remarkably, except for region 5, the examined regions do not show any significant

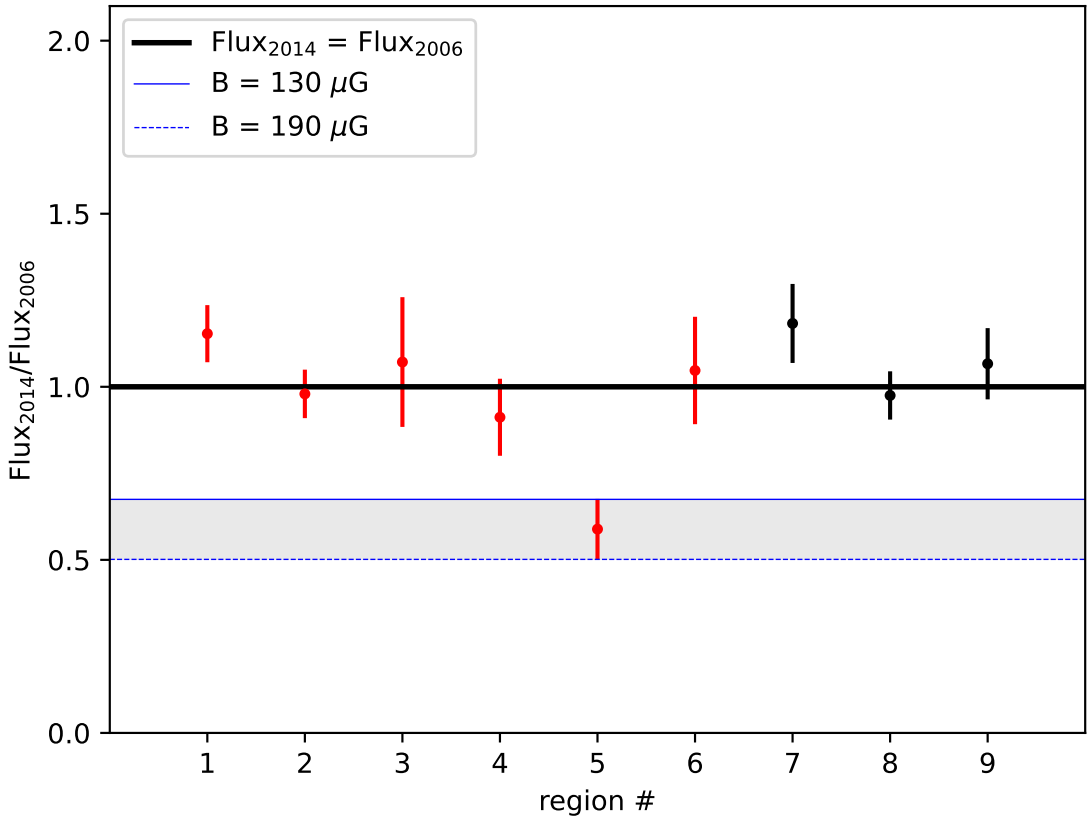

Figure 4.7: Ratio of the 2014 nonthermal flux (4.1 – 6 keV) to that measured in 2006 for northern regions (in red) and southern regions (in black). The blue lines represent the theoretical flux decrease expected for synchrotron losses with a magnetic field strength of 130 μG (solid line) and 190 μG (dashed line).

decrease in flux. This confirms that these regions have remained within a loss-limited regime throughout the eight-year time base considered, as predicted in Section 4.4.2.

Interestingly, the measurements of flux in region 5 show a significant decrease of the synchrotron radiation over this 8 year baseline. This effect is the result of the synchrotron losses being dominant over the acceleration efficiency, as predicted in Section 4.4.2 and in nice agreement with what I showed in Figure 4.6. As a further confirmation for this scenario, I show in Figure 4.7 the comparison between the observed flux decrease with

that expected from synchrotron losses[2] in a magnetic field of 130 μG and 190 μG (solid and dashed blue curves in Figure 4.7, respectively), showing the consistency between model and data points.

Conversely, region 1 and 7 show a barely significant ($\gtrsim 1\sigma$ level) increase in flux between the two epochs, which may suggest that in these regions $t_{acc} < t_{syn}$. Further investigations are necessary to confirm this latest point.

4.4.4 A comparison with radio polarization

The measurement of polarization plays a significant role in SNRs as it serves as an indicator of the ordering of the magnetic field. Taking advantage of the radio fractional polarization map, I can test the scenario I have proposed for Kepler's SNR. Figure 4.8 presents the 1.4 GHz fractional polarization map from DeLaney et al. (2002). In the map, the north shows a polarization fraction which is, on average, lower than in the south. Since a lower value of polarization fraction is associated with a more turbulent magnetic field, this results is a strong, additional proof that points toward a scenario in which the electron acceleration in the north is enhanced by a turbulent magnetic field, generated in the interaction of the shock with the dense CSM.

A similar pattern was found by Suzuki et al. (2022) in RCW86 (in the southwestern region where the remnant is interacting with a dense cloud). In particular, they retrieved a low Bohm factor in the region where radio observations show a low degree of polarization (Dickel et al. 2001).

I calculated the polarization fraction and the radio index from the data of DeLaney et al. (2002) in the nine regions shown in Figure 4.1. The regions corresponds to regions $1-9$ of Figure 4.1, but are shifted inwards to account for the expansion of the SNR in the period between the X-ray and radio observations (which date back to 1997). The measurements are shown in Table 4.3: the polarization fraction in the North (regions 3-6) is about 3 times smaller than in the South (regions 7-9).

One may use these data for an independent estimate of the difference between the Bohm factor in the North and in the South, for the radio emitting electrons. Bandiera & Petruk (2016) generalized the classic synchrotron theory to cases where electrons emit in a magnetic field with ordered and disordered components. Equation (31) in their paper relates the radio index and the ratio $\delta B_\perp / B_\perp$ to the polarization fraction (the subscript $\perp$ refers to the components in the plane of the sky). This relation yields $\delta B_\perp / B_\perp = 4.20 \pm 0.02$ and 2.30 ± 0.14 for the North and South respectively. Next, the relation $\eta \approx (\delta B/B)^{-2}$ may be used to estimate η from $\delta B/B$. In this expression, the strengths of the turbulent δB and of the ordered B components refer to the three-dimensional

[2]Theoretical decrease of the flux is calculated by numerical integration of the product of the 'single-electron' emissivity and the momentum distribution of electrons taking into account their radiative losses in the magnetic field.

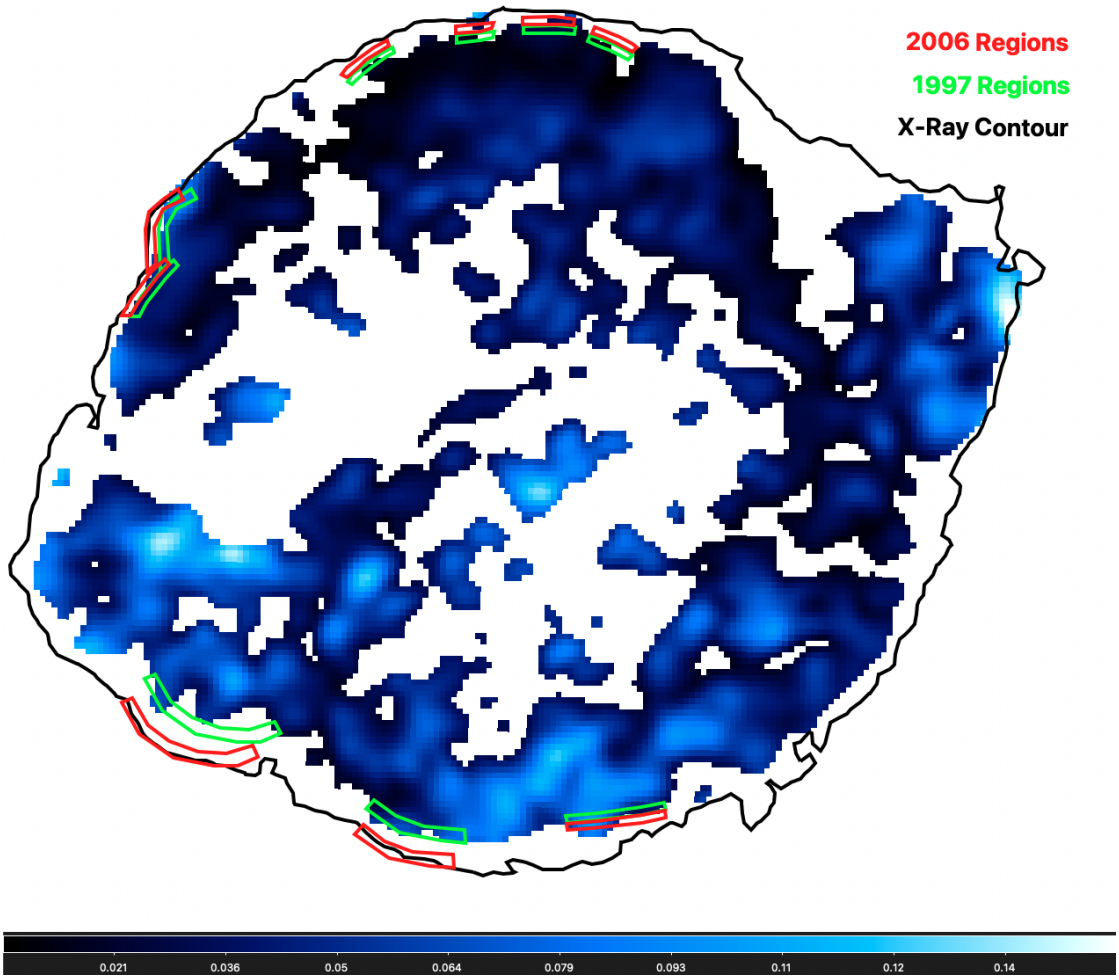

Figure 4.8: Polarization fraction at 1.4 GHz from DeLaney et al. (2002). The black contours overlaid indicate the *Chandra* image for the year 2000. The red polygons are the same as Figure 4.1. The green polygons are the extraction regions (shifted to take into account the remnant expansion) chosen to measure the spectral index and the polarization fraction.

vectors which are related to the projected ones as $\delta B_\perp = \delta B/\sqrt{3}$, $B_\perp = B \sin\varphi$ with φ being the angle between the line of sight and the vector **B**. I do not know the actual three-dimensional orientation of **B** in my regions of interest. Therefore, by assuming φ to be the same in all the regions, I derive a ratio between the Bohm parameter of southern regions (η_S) and the Bohm parameter of northern regions (η_N) as $\eta_S/\eta_N = 3.3 \pm 0.4$. This value corresponds well to that obtained from the X-ray data analysis.

Table 4.3: The radio index α between 1.4 and 4.8 GHz and the polarization fraction Π at 1.4 GHz from the radio data of DeLaney et al. (2002).

region	α	Π, %
1	0.680 ± 0.009	4.1 ± 0.5
2	0.670 ± 0.007	7.4 ± 1.2
3	0.690 ± 0.006	2.1 ± 0.2
4	0.680 ± 0.002	1.5 ± 0.1
5	0.670 ± 0.003	2.7 ± 0.2
6	0.680 ± 0.002	1.4 ± 0.2
7	0.660 ± 0.019	6.4 ± 2.5
8	0.660 ± 0.009	6.2 ± 1.5
9	0.690 ± 0.022	5.3 ± 1.5

Notes. Errors shown are 1σ statistical only.

4.5 Conclusions

I analyzed different *Chandra*/ACIS archive observations of the Kepler's SNR in two separate epochs: 2006 and 2014. My analysis has added some significant findings to my previous study (Sapienza et al. 2022, refer to Chapter 3), regarding particle acceleration and synchrotron emission in Kepler's SNR. Firstly, my research has confirmed the existence of two distinct regimes of particle acceleration, with electron acceleration proceeding closer to the Bohm limit in the northern part of the remnant than in the freely expanding southern part. This strongly supports the scenario in which the interaction between the shock and dense CSM in the northern regions results in the amplification of magnetic field turbulence that speed-up the acceleration process. The analysis of the polarization fraction in Kepler's SNR provides a further compelling evidence that the acceleration process is influenced by the magnetic field's turbulent nature. The lower polarization fraction observed in the northern region, indeed, suggests the presence of an enhancement of the magnetic field turbulence therein.

While the reduction of the Bohm factor in the North speeds up the acceleration process, the interaction with the dense CSM significantly decelerates the shock, thus increasing the acceleration time. I find that the two effects compensate to each other in the majority of the regions analyzed, and the electron acceleration proceeds steadily in the loss-limited regime. However, in one region (characterized by a very low shock speed) I find that the radiative losses dominate over the acceleration process and I report a gradual decrease in the synchrotron emission together with a decrease in the cutoff photon energy.

This provides the first evidence of fading synchrotron emission in the northern part of Kepler's SNR. The drop of the synchrotron flux allows me to estimate the local strength

of the magnetic field ($B \sim 130 - 190\ \mu$G).

Overall, my study provides a coherent and comprehensive understanding of the loss-limited acceleration in Kepler's SNR. The role played by the CSM interacting with the shock in affecting the particle acceleration and synchrotron emission has been elucidated, contributing to a deeper comprehension of this fascinating celestial object.

5

X-ray emitting structures in the Vela SNR: Ejecta anisotropies and progenitor stellar wind residuals

Abstract

The Vela SNR shows several ejecta fragments (or shrapnel) protruding beyond the forward shock, which are most likely relics of anisotropies that developed during the SN explosion. Recent studies have revealed high Si abundance in two shrapnel (A and G), located in opposite directions with respect to the SNR center. This suggests the possible existence of a Si-rich jet-counterjet structure, similar to that observed in the SNR Cassiopea A. I analyzed an *XMM-Newton* observation of a bright clump, behind shrapnel G, which lies along the direction connecting shrapnel A and G. The aim is to study the physical and chemical properties of this clump to ascertain whether it is part of this putative jet-like structure. I produced background-corrected and adaptively-smoothed count-rate images and median photon energy maps, and performed a spatially resolved spectral analysis. I identified two structures with different physical properties. The first one is remarkably elongated along the direction connecting shrapnel A and G. Its X-ray spectrum is much softer than that of the other two shrapnel, to the point of hindering the determination of the Si abundance; however, its physical and chemical properties are consistent with those of shrapnel A and G. The second structure, running along the southeast-northwest direction, has a higher temperature and appears similar to a thin filament. By analyzing the ROSAT data, I have found that this filament is part of a very large and coherent structure that I identified in the western rim of the shell. I obtained a thorough description of the collimated, jet-like tail of shrapnel G in Vela SNR. In addition I discovered a coherent and very extended feature roughly perpendicular to the jet-like structure that I interpret as a signature of an earlier interaction of the remnant

with the stellar wind of its progenitor star. The peculiar Ne/O ratio I found in the wind residual may be suggestive of a Wolf-Rayet progenitor for Vela SNR, though further analysis is required to address this point.

The work presented in this Chapter has been published under the title "*X-ray emitting structures in the Vela SNR: Ejecta anisotropies and progenitor stellar wind residuals*" in the scientific journal "Astronomy & Astrophysics, Volume 649, id. A56" (Sapienza et al. 2021, DOI: https://doi.org/10.1051/0004-6361/202140412).

5.1 Introduction

CCSNRs show complex morphologies that result from intrinsic asymmetries in the SN explosion and from the propagation of the explosion shock-waves in very inhomogeneous environments, such as pre-existing stellar winds and molecular clouds. Therefore, it is difficult to distinguish the role played by the ISM inhomogenities from that played by pristine anisotropies in the ejecta in shaping the remnant morphology. X-ray observations of SNRs are useful diagnostic tools to trace the distribution of the physical and chemical properties of the emitting ejecta and a starting point to reconstruct the details of the explosion mechanism and the structure of the ambient environment surrounding the exploded star.

Vela SNR, the relic from the explosion of a massive star that occurred $\sim$ 11 kyr ago (Taylor et al. 1993), is an interesting target to study especially because of its proximity: with a distance of only 280 pc (Dodson et al. 2003), it is the nearest SNR. This makes it possible to resolve the X-ray emission of small-scale structures spatially and to identify the ejecta to study their properties.

Aschenbach et al. (1995) identified six X-ray emitting bow-shaped ejecta fragments in regions beyond the forward shock called "shrapnel" named from A to F (see Figure 5.1). X-ray emitting ejecta have also been observed, in projection, inside the shell (Miceli et al. 2008a; LaMassa et al. 2008; Slane et al. 2018). Shrapnel A, which is one of the most distant ejecta from the explosion center, exhibits a pattern of heavy element abundances that are different from that observed in all the other ejecta. Katsuda & Tsunemi (2006) determined the abundances of the shrapnel by finding a nearly solar abundance for Ne, O, Mg and Fe, and overabundant Si. The latter is expected to be produced in deeper layers of the progenitor star compared to lower Z elements such as O, Ne, and Mg. Si-rich ejecta are not expected to be so distant from the explosion center of the remnant, indicating that an inversion of ejecta layers occurred at some point during the remnant evolution. Miceli et al. (2013b) show, with dedicated 2-D hydrodynamic simulations, that velocity and density contrast with respect to the surrounding ejecta are necessary to make the Si-rich shrapnel overtake the other shrapnel and the forward shock. More recent 3-D magneto-hydrodynamic simulations confirmed the important role played by explosion asymmetries in determining a spatial inversion of ejecta layers

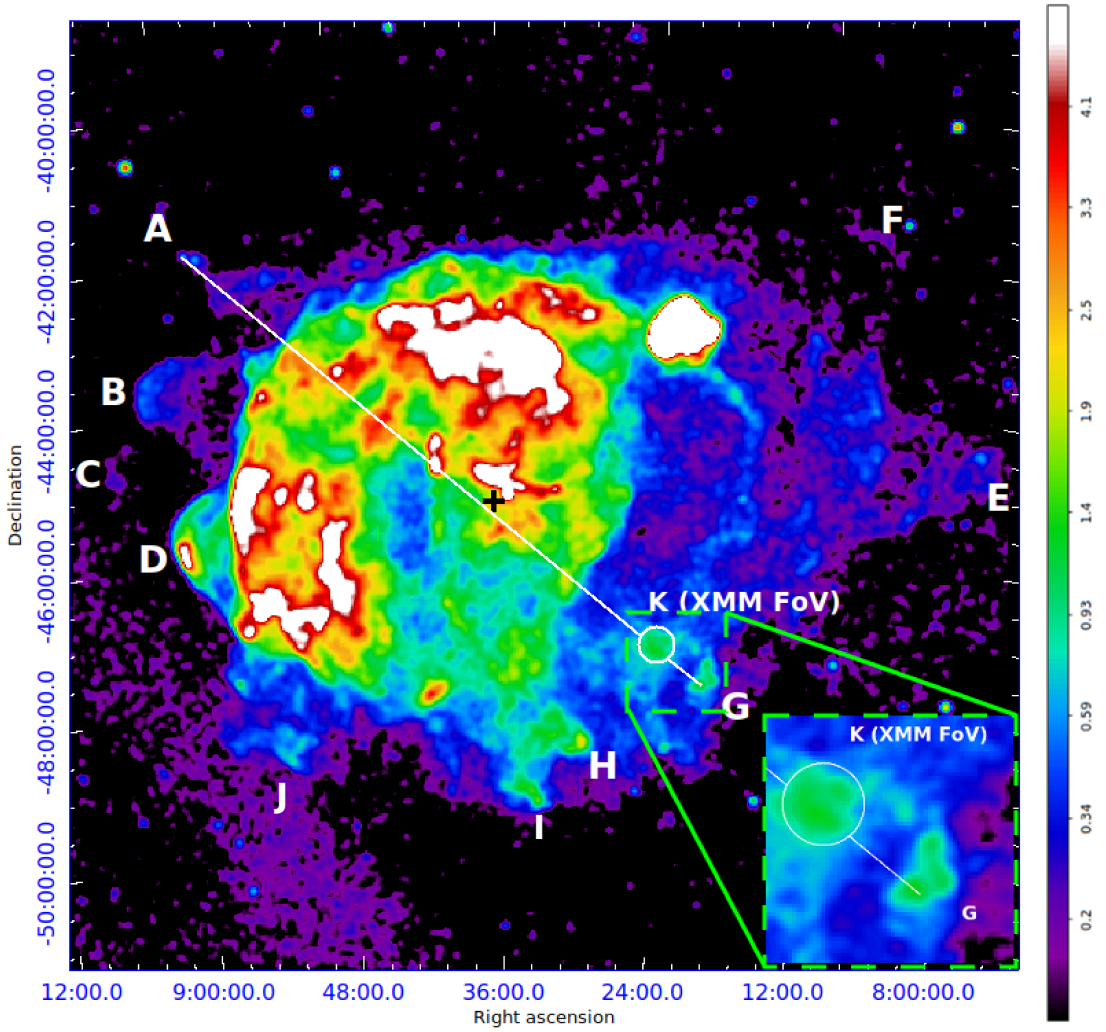

Figure 5.1: RASS count image of Vela SNR in the 0.1 – 2.4 keV energy band in squared root scale. The circle K is the region analyzed in this work, marking the *XMM-Newton* FoV. The black cross indicates the position of the Vela pulsar at the explosion time by considering an age of 11 kyr and taking into account the pulsar proper motion estimated by Caraveo et al. (2001). I assume it as the explosion center. The inset is a close-up view of the same image in the region of shrapnel G and K.

(Orlando et al. 2016, Tutone et al. 2020 and Orlando et al. 2021).

García et al. (2017) analyzed an X-ray luminous knot, named shrapnel G (see Figure 5.1), in the southwestern region of Vela SNR. Shrapnel G is located in the anticenter with respect to shrapnel A. García et al. (2017) found that the chemical composition of

shrapnel G is very similar to that of shrapnel A. This suggests that shrapnel A and G are part of a jet-counterjet-like event which has throw away the inner layer of the progenitor star and has made them overcome lighter ejecta and the forward shock (somehow similar to that observed in Cassiopea A, Vink 2004). To confirm that shrapnel A and G are part of a Si-rich jet-like structure, it is necessary to ascertain the nature of the Si emission and to study the region between the two ejecta knots in detail.

The *ROSAT* image (see Figure 5.1) of the whole Vela SNR shows that shrapnel G is followed by another bright clump, labeled "knot K". This knot seems to lay along the line connecting shrapnel A, shrapnel G, and the center of the SNR. This suggests that knot K could be physically linked to shrapnel G, which would prove the existence of a coherent Si-rich feature on a large spatial scale.

In this Chapter, I present the analysis of an *XMM-Newton* observation of knot K to study its physical and chemical properties, and to ascertain whether it is part of a jet-like structure linking shrapnel A and G. I complement the analysis of the *XMM-Newton* data with *ROSAT* archive observations from the western part of Vela SNR's shell. The Chapter is organized as follows: In Section 5.2 I present the data and their analysis; Section 5.3 and Section 5.4 show the results of *XMM-Newton* and *ROSAT* data analysis, respectively. Finally, I discuss my results in Section 5.5.

5.2 Observations and data analysis

5.2.1 *XMM-Newton*

I analyze an *XMM-Newton* (see Sect. 2.2) EPIC observation of Vela SNR knot K. The *XMM-Newton* observation was performed from October 07, 2019 to October 08, 2019 (Obs. ID 0841510101, PI: M. Miceli), with pointing coordinates α_{J2000} = $08^h23^m32.49^s$ and δ_{J2000} = -47° 11' 55.8", with the medium filter, and in the full frame mode. The exposure times are 55 ks, 55 ks, and 51 ks for the MOS1, MOS2, and pn cameras, respectively. I processed the data with the SAS software, version 18.0.0.

EPIC event files are typically contaminated by soft-protons, that is to say mildly relativistic protons that are detected by the CCD cameras. I filtered the event lists for soft-proton contamination with the `espfilt` task, thus obtaining a screened exposure time of approximately 33 ks for the MOS1, 37 ks for the MOS2, and 19 ks for the pn camera (only 37% of the total exposure). I then filtered the event lists retaining only events with `FLAG=0` and `PATTERN`$\leq$`4,12` for pn and MOS cameras, respectively. I adopted a source detection procedure, using the `edetect_chain` SAS task to remove events in circular regions (with radius 18") around point-like sources.

All images were background subtracted by adopting the double subtraction procedure described in Miceli et al. (2017) to take instrumental, particle, and X-ray background

contamination into account. For this purpose, I used the FWC and BS files available at XMM ESAC webpages[1]. All the EPIC images in this Chapter are superpositions of the MOS1, MOS2, and pn images, obtained by using the `emosaic` SAS procedure. I produced vignetting-corrected count-rate maps. It is possible to correct for vignetting by dividing the superposed images by the corresponding superposed exposure maps produced by using the `eexpmap` SAS command. The pn exposure maps were scaled by the ratio of the pn/MOS effective areas to make MOS-equivalent superposed count-rate maps. I then smoothed the resulting count-rate maps adaptively, in order to reach a user-defined signal-to-noise ratio by adopting the `asmooth` SAS task.

I performed spatially resolved spectral analysis for all three EPIC detectors. For this purpose, I corrected the vignetting effect in the spectra using the `evigweight` SAS command. For each spectrum, I produced the RMF (with the `rmfgen` task) and the ARF (with the `arfgen` task) and I binned spectra to obtain at least 25 counts per bin.

5.2.2 *ROSAT*

I also analyzed the RASS (see Sect .2.1) data of the western region of Vela SNR to complement the *XMM-Newton* data analysis. The RASS PSPC observation pointing the western part of Vela SNR was performed between October 17, 1990 and November 22, 1990, with pointing coordinate $\alpha_{J2000} = 8^h15^m00^s$ and δ_{J2000} =-45°00'00" (Observation ID WG932517P_N1_SI01.N1) without any filter in survey mode and a total exposure of 23 ks. The total FoV of the observation is a 6°30' × 6°30' box.

The *ROSAT* archive provides processed event lists, distributed as FITS files, and no further data reduction is necessary for the user. I produced *ROSAT* count maps and spectra using the XSELECT analysis system tools `extract image` and `extract spectrum`, respectively. For the spectral analysis, I used the `pspcc_gain1_256.rmf` RMF file and `pspcc_gain1_256.rsp` on-axis response matrices file to calculate the ARF file for an off-axis region with the FTOOLS command `pcarf`. All these files are stored on an HEASARC ftp server[2]. I binned the spectra energy channels in order to have at least 25 counts per channel.

The spectral analysis of *XMM-Newton* and *ROSAT* spectra was performed with the HEASOFT software XSPEC version 12.9.1 (Arnaud 1996) with the solar abundances table from Anders & Grevesse (1989).

5.3 *XMM-Newton* results

[1] https://www.cosmos.esa.int/web/xmm-newton/filter-closed
http://xmm-tools.cosmos.esa.int/external/xmm_calibration//background/bs_repository/blanksky_all.html

[2] https://heasarc.gsfc.nasa.gov/FTP/caldb/data/rosat/pspc/cpf/matrices/

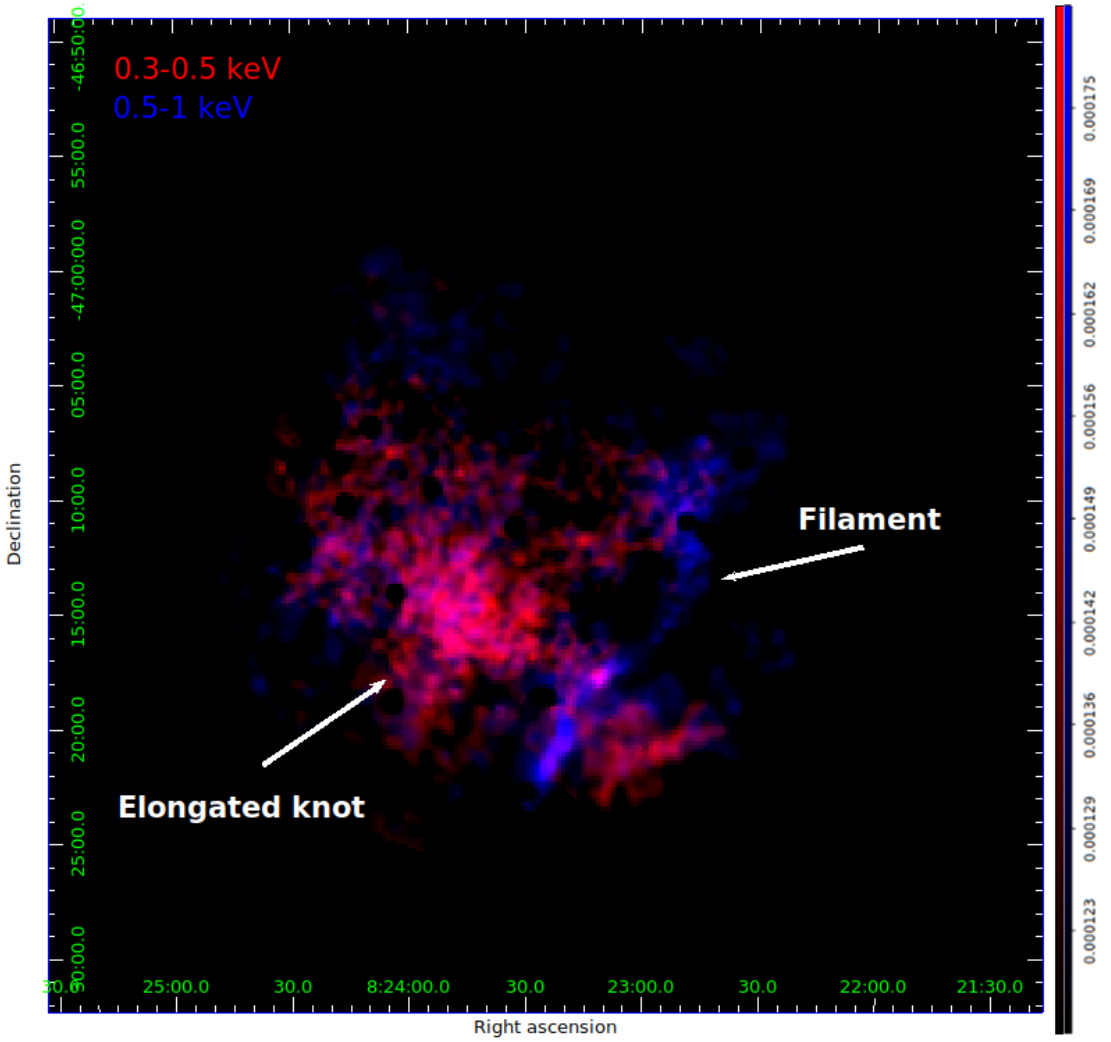

Figure 5.2: EPIC count-rate color composite image in the 0.3 – 0.5 keV band (red) and 0.5 – 1 keV band (blue) in linear scale. The bin size is 10″, and the image was adaptively smoothed to a signal-to-noise ratio of 20. North is up and east is to the left.

5.3.1 Images

In Figure 5.2, I present the EPIC composite count-rate image of the Vela SNR knot K, showing the 0.3 – 0.5 keV emission in red and the 0.5 – 1.0 keV band emission in blue. In the 0.3 – 0.5 keV band, an elongated knot clearly sticks out. This knot seems to be strongly elongated, extending for $\sim 20'$ (corresponding to $\sim 5 \times 10^{18}$ cm at a distance of 280 pc) in the northeast-southwest direction, and only $\sim 5'$ ($\sim 1 \times 10^{18}$ cm) on the average in the southeast-northwest direction. The elongated knot is less visible in the

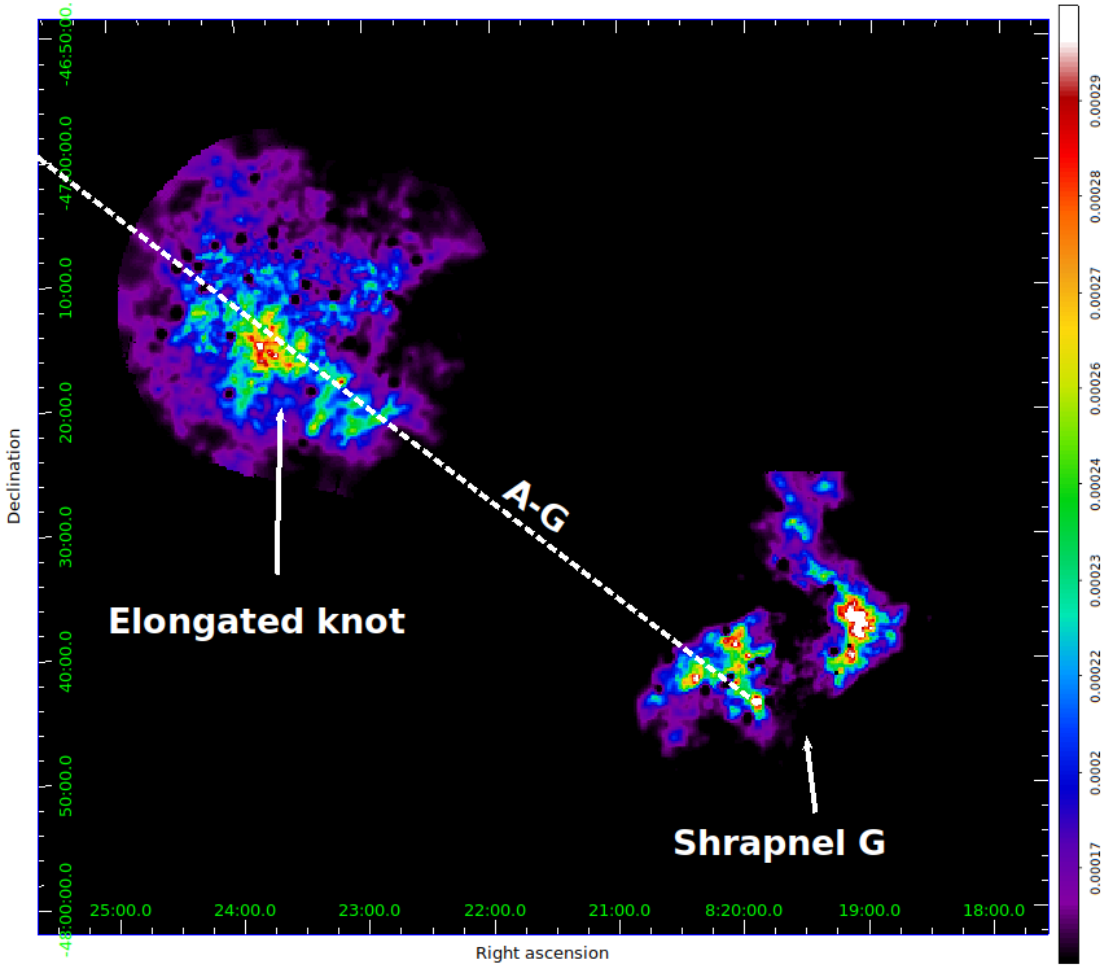

Figure 5.3: EPIC count-rate image of shrapnel G and knot K in the 0.3 – 0.6 keV energy band in squared scale. The bin size is 10″ and the image was adaptively smoothed to a signal-to-noise ratio of 20. The white dashed line connects shrapnel G and shrapnel A (shrapnel A is outside the field of view of this image, on the opposite side of Vela SNR, see Figure 5.1).

0.5 – 1 keV band, where a narrow filament running in the northwest-southeast direction emerges.

In Figure 5.3 I show the mosaic of images of the Vela SNR shrapnel G and knot K in the 0.3 – 0.6 keV energy band (i.e., the soft energy band adopted by García et al. 2017) to reveal possible connections between the structures detected in the FoV of knot K and those observed in shrapnel G by García et al. (2017). The image clearly shows that the elongated knot remarkably lays along the line (indicated by a white dashed line in Figure

5.3, see also Figure 5.1) connecting shrapnel A, shrapnel G, and the explosion site. The explosion site, shown by the black cross in Figure 5.1, can be estimated by taking into account the proper motion of the Vela pulsar (Caraveo et al. 2001) and assuming an age of 11 kyr. The excellent alignment between the explosion site, the elongated structure, and the two Si-rich shrapnel is suggestive of a possible physical link between the elongated knot and the Si-rich ejecta. This may indicate that the elongated knot is somehow part of a jet-like structure associated with shrapnel A and G (though its X-ray emission is much softer than that of the two shrapnel).

5.3.2 Median photon energy map

To investigate the thermal distribution of the X-ray emitting plasma, I produced maps of median photon energy (E_m) for the pn camera, that is to say maps showing the median energy of the photons detected pixel-by-pixel in a given energy band. These maps not only provide information on the spatial distribution of the X-ray emission spectral hardness of the source, but also on the local value of the equivalent hydrogen column (the higher the absorption, the higher the E_m value).

In Figure 5.4 I show the pn E_m map produced in the 0.3 – 1.0 keV energy band. The pixels in the map have a size of 20″ so as to collect more than ten counts per pixel. I smoothed the map by adopting the procedure described in Miceli et al. (2008b), with $\sigma = 60''$. I verified that the instrumental background does not affect the E_m value, since its count-rate is from 15 up to 30 times lower than the signal count-rate. Also, I verified from the FWC file that there are no pieces of evidence of significant fluctuations across the FoV in pn instrumental background. The map clearly shows that the E_m of the elongated knot is lower than that of the filament. Since the interstellar absorption in this region of the Vela SNR is quite uniform (refer to Lu & Aschenbach 2000), the most natural explanation is that the plasma temperature is higher in the filament than in the elongated knot. This confirms that the two structures have different physical properties.

5.3.3 Spectra

The analysis described in the previous subsections (Section 5.3.1 and Section 5.3.2) allowed me to identify X-ray emitting plasma structures with homogeneous physical properties. To further investigate the physical and chemical properties of the plasma, I performed a spatially-resolved spectral analysis. I first focused on the elongated knot which appears similar to a trailing wake of shrapnel G (see Figure 5.3).

I selected a polygonal spectral-extraction region labeled *Elong_knot*, including the whole jet-like structure, indicated by the black polygon in Figure 5.5. I extracted the spectrum of the background from the red region shown in Figure 5.5, characterized by a very low surface brightness. By selecting other background regions (within the blue areas of Fig 5.5), I verified that the results of the spectral analysis do not change

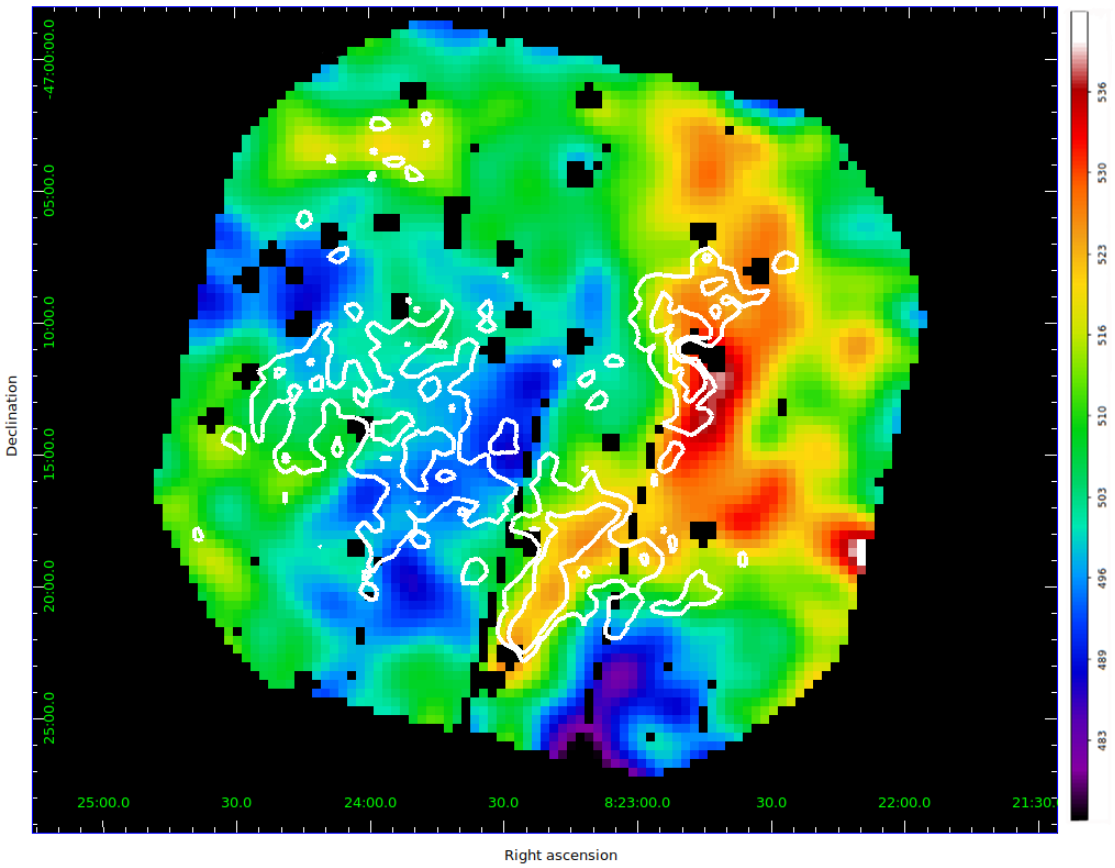

Figure 5.4: Median photon energy map of the knot K region obtained with EPIC pn data in the 0.3 – 1.0 keV energy band in linear scale. The map was smoothed by adopting a Gaussian kernel with $\sigma = 60''$. The overlaid white contours indicate the count-rate levels at 50% and 60% of the maximum in the 0.5 – 1.0 keV energy band. The bin size is 20″ and the characteristic error for the median energy is ∼ 10 eV.

significantly: The best fit parameters are all consistent within 1σ. The spectra of all cameras above 1.3 keV are dominated by the background. I verified that the results of the spectral analysis do not change significantly by performing the analysis in the 0.3 – 2 keV band or in the 0.3 – 1.3 keV band. Thus I performed the analysis in the 0.3 – 1.3 keV band to maximize the signal-to-noise ratio.

The elongated knot spectrum shows thermal features, namely emission line complexes of O VII at ∼ 0.57 keV and of Ne IX at ∼ 0.92 keV (see Figure 5.6). I fit the spectra with a model of isothermal optically-thin plasma in CIE (`vapec` model in XSPEC) with nonsolar abundances. I also included the effects of photoelectric absorption by ISM (`tbabs` model in XSPEC). By letting the O abundance free to vary, the

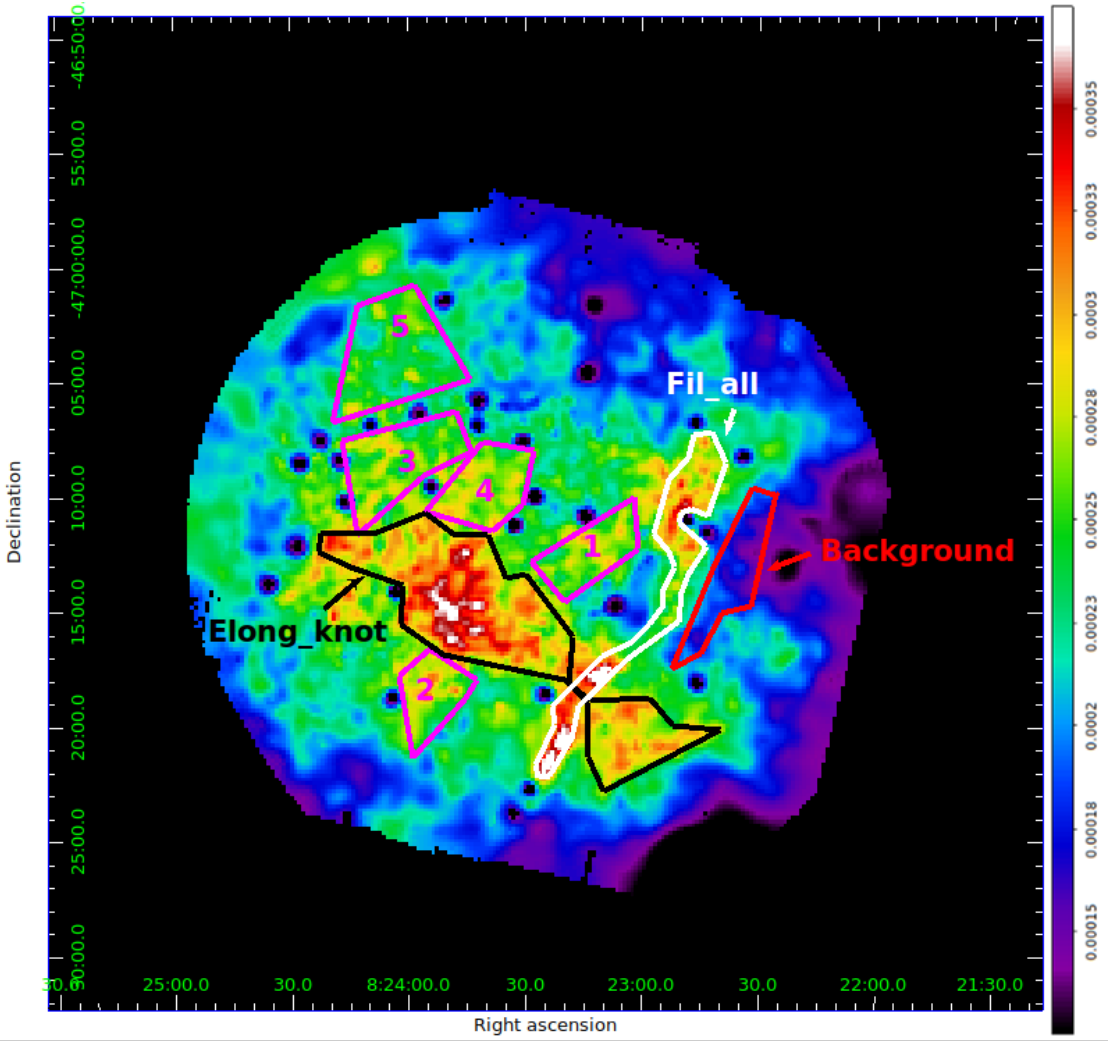

Figure 5.5: EPIC count-rate image in the 0.3 – 1.0 keV energy band in linear scale. The bin size is 10″ and the image was adaptively smoothed to a signal-to-noise ratio of 20. Regions selected to extract the spectra of the elongated knot (black polygon) and of the filament (white polygon) are superimposed. The region selected for background extraction is shown in red. The regions selected to extract control spectra are shown in magenta (see Section 5.3.3).

fit provides $\chi^2/d.o.f. = 328.14/300$. I verified that the quality of the fit does not significantly improve by letting the Ne abundance free to vary. Moreover, the fitting procedure is not sensitive to the Fe abundance, probably because the plasma temperature ($T \sim 1.5 \times 10^6$ K) is too low for significant Fe L lines to be emitted in the 0.7 – 1.3

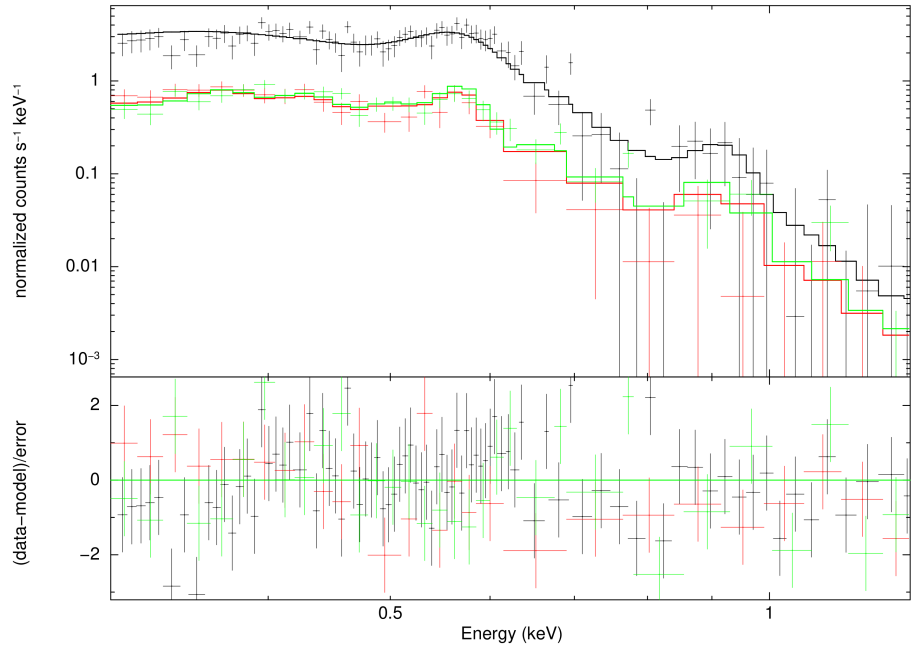

Figure 5.6: EPIC spectra (pn in black, MOS1 in red and MOS2 in green) extracted from the *Elong_knot* region (shown in Figure 5.5) with the corresponding CIE best-fit model and residuals in the 0.3 − 1.3 keV band.

keV energy band. Best-fit values are shown in Table 5.1. Error bars are at the 90% confidence level.

The best fit temperature is somehow entangled with the best fit value of the column density (as shown in Figure 5.7), which is forced to be lower than 6×10^{20} cm^{-2}, in agreement with the findings by Lu & Aschenbach (2000) in this region of the shell. Though the spectral analysis of shrapnel G makes it possible to constrain the chemical abundances of more elements than that of knot K, the Ne (and Mg) to O abundance ratio that I found in the elongated knot (Ne/O = Mg/O = $2.6^{+0.5}_{-0.4}$ with Ne and Mg abundances fixed to the solar values) is similar to that found in the ejecta in other regions of the Vela SNR. This includes shrapnel G (García et al. 2017), shrapnel A (Katsuda & Tsunemi 2006), shrapnel D (Katsuda & Tsunemi 2005), the ejecta found in the RegNe region (Miceli et al. 2008a), and those in the Vela X region (LaMassa et al. 2008). Though an ISM origin cannot be firmly excluded, this result seems to support an ejecta origin for the elongated knot.

Table 5.1: Best-fit parameters for the region *Elong_knot* shown in Figure 5.5 with the CIE best-fit model (vapec).

Parameter	Elong_knot
$^{a}N_{\rm H}$ (10^{22} cm^{-2})	> 0.05
kT (keV)	$0.124^{+0.006}_{-0.005}$
O/O$_{\odot}$	$0.36^{+0.07}_{-0.05}$
Ne/Ne$_{\odot}$	1^{b}
$^{c}n^2l$ (10^{18} cm^{-5})	$1.7^{+0.1}_{-0.2}$
$\chi^2/d.o.f.$	327.97/300

Notes. Errors are at the 90% confidence level. ^{a}Upper limit fixed to 0.06. ^{b}Fixed value. ^{c}Emission measure per unit area.

Table 5.2: Best-fit parameters for spectra from regions labeled from 1 to 5 shown in Figure 5.5.

Parameter	1	2	3	4	5
kT (keV)	$0.108^{+0.009}_{-0.012}$	$0.109^{+0.005}_{-0.015}$	$0.108^{+0.004}_{-0.015}$	$0.109^{+0.007}_{-0.009}$	$0.108^{+0.003}_{-0.017}$
O/O$_{\odot}$	$0.40^{+0.334800}_{-0.1}$	$0.66^{+0.19}_{-0.16}$	$0.5^{+0.2}_{-0.1}$	$0.56^{+0.15}_{-0.15}$	$0.6^{+0.4}_{-0.1}$
n^2l (10^{18} cm^{-5})	$1.4^{+0.5}_{-0.1}$	$2.3^{+0.6}_{-0.4}$	$1.5^{+0.6}_{-0.2}$	$1.6^{+0.3}_{-0.2}$	$1.3^{+0.6}_{-0.1}$
χ^2/d.o.f.	255.45/225	175.15/168	260.62/252	284.48/239	267.15/243

Notes. Errors are at the 90% confidence level. $N_{\rm H}$ value fixed to 0.06 and Ne/Ne$_{\odot}$ value is fixed to 1.

I also extracted spectra from five regions surrounding the *Elong_knot* (labeled 1-5 in Figure 5.5) and found that the plasma temperature therein is always significantly lower than that of the knot. Moreover, the Ne/O abundance ratio is systematically (sometimes significantly) lower than that of the elongated knot (see Table 5.2). These results clearly show that all these regions do not belong to the elongated knot, which is indeed confined to a narrow, jet-like stripe along the direction connecting shrapnel A and shrapnel G.

García et al. (2017) modeled the spectrum of shrapnel G with an absorbed isothermal component in NEI and non-solar abundances. I checked if a similar scenario can be adopted for the elongated knot K by fitting its spectrum with the same model as that in García et al. (2017) by letting only the plasma temperature and the normalization free to vary. I thus obtained a good fit to the *Elong_knot* spectrum ($\chi^2/d.o.f. = 435.55/302$). Nevertheless, the quality of the fit is clearly worse than that obtained by the model in CIE. In any case, I found that the two spectral models adopted (CIE and NEI) clearly show that the plasma temperature of the elongated knot is significantly lower than that

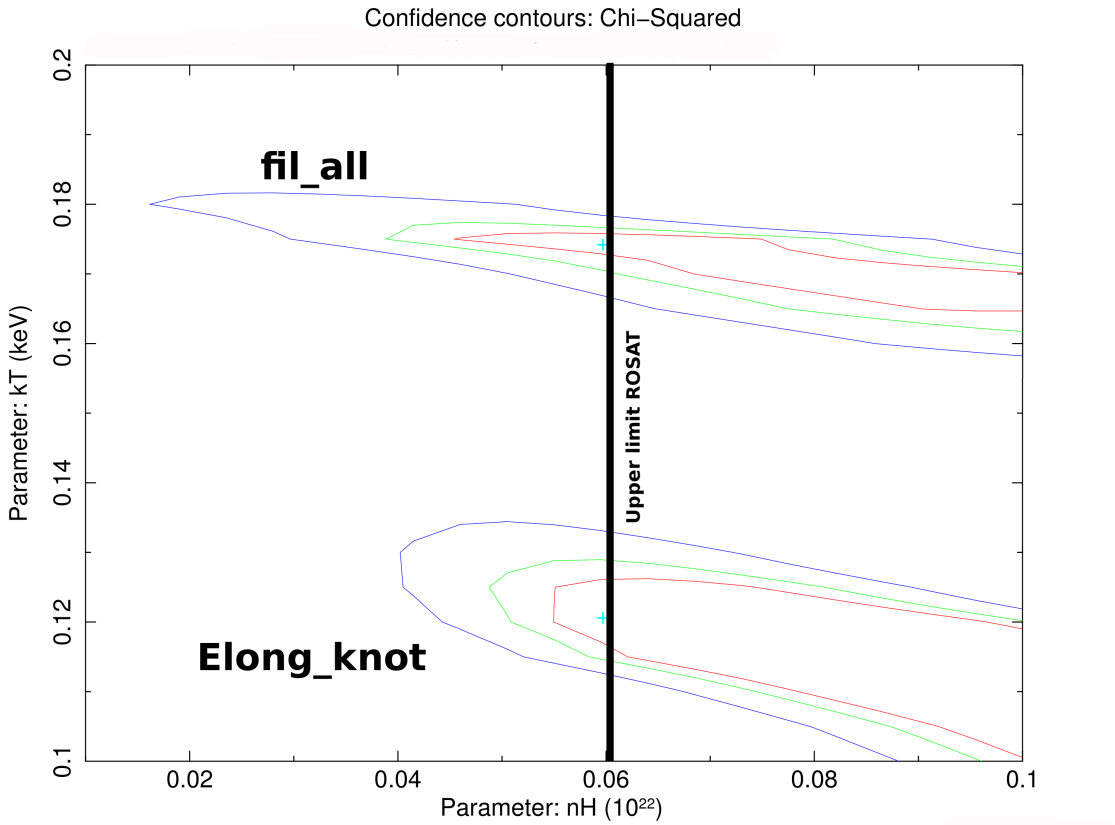

Figure 5.7: 68% (red), 95% (green), and 99.5% (blue) contour levels of the $N_{\rm H}$ vs. kT best fit values, as derived from the spectral analysis of the *fil_all* and *Elong_knot* spectra. The black line shows the upper limit for $N_{\rm H}$ found by Lu & Aschenbach (2000).

of shrapnel G (see Table 5.1 and Table 5.3), as expected. Because of its interaction with the medium swept, the head of a jet-like structure (shrapnel G) is hotter than its tail (knot K), that is interacting with an expanding medium.

At the low temperature of the elongated knot, the emissivity of the Si XIII emission line is extremely low and this hampers the emergence of the Si emission line above the continuum component of the spectrum and above the background. This hinders the possibility of obtaining an accurate measure of the Si abundance in the elongated knot, given that the emerging spectrum is actually insensitive to this parameter. I have repeated the spectral analysis of the elongated knot either in CIE or in NEI by also including the spectral data points in the 1.3 – 2 keV energy band to include the energy bins corresponding to the Si XIII emission line (around 1.8 keV). I let the Si abundance free to vary in the fitting procedure. I found that the Si abundance is almost

Table 5.3: Best-fit parameters for region *Elong_knot* shown in Figure 5.5 obtained with the NEI model compared with those found in shrapnel G by García et al. (2017).

Parameter	Elong_knot	Shrapnel G
$N_{\rm H}$ (10^{22} cm^{-2})	$0.06^{\star}$	$0.022^{+0.014}_{-0.014}$
kT (keV)	$0.113^{+0.011}_{-0.006}$	$0.49^{+0.04}_{-0.04}$
τ (10^{10} s cm^{-3})	$3.1^{\star}$	$3.1^{+0.3}_{-0.3}$
C/C$_{\odot}$ = $N/N_{\odot}$ = $O/O_{\odot}$	$0.47^{\star}$	$0.47^{+0.10}_{-0.10}$
Ne/Ne$_{\odot}$	$1.33^{\star}$	$1.3^{+0.2}_{-0.2}$
Mg/Mg$_{\odot}$	$0.92^{\star}$	$0.9^{+0.2}_{-0.2}$
Si/Si$_{\odot}$	$2.24^{\star}$	$2.2^{+0.9}_{-0.9}$
Fe/Fe$_{\odot}$	$0.29^{\star}$	$0.29^{+0.08}_{-0.08}$
$n^2 l$ (10^{18} cm^{-5})	$1.7^{+0.1}_{-0.2}$	$0.21^{+0.06}_{-0.06}$
χ^2/d.o.f.	435.55/302	635.91/451

Notes. Errors are at a 90% confidence level. *Fixed value.

unconstrained (as expected), obtaining a best fit value of 6 ± 4 in NEI, and the abundance constrained to be < 2 in CIE. In any case, the Si abundance is consistent with that found in shrapnel G by García et al. (2017) and in shrapnel A by Katsuda & Tsunemi (2006). Therefore, although it is not possible to prove that the jet-like structure is Si-rich, the spectral analysis shows that a spectrum of Si-rich plasma is perfectly consistent with the observed spectrum and that the jet-like structure could have the same Si abundance as shrapnel A and shrapnel G.

The second X-ray emitting structure that emerges in Figure 5.2 has the shape of a narrow filament. Therefore, I extracted the spectrum from a large region indicated by the white polygon, labeled *fil_all*, in Figure 5.5, including the whole filament. I adopted the same background spectrum as that used for the elongated knot. The spectrum of the region shows thermal emission, characterized by emission lines from O VII at ~ 0.57 keV, from O VIII at ~ 0.65 keV, and from Ne IX at ~ 0.92 keV (see Figure 5.8). To fit the spectrum, I first adopted a model of isothermal plasma in CIE (`vapec`) with solar abundances, including the effects of photoelectric absorption by the ISM (`tbabs`). I fixed the $N_{\rm H}$ to the best-fit value found for the elongated knot. By letting the O and Ne abundance free to vary, the fit provides $\chi^2/d.o.f. = 337.67/276$. Best-fit values are shown in Table 5.4. Error bars are at a 90% confidence level. EPIC spectra with the corresponding best-fit model and residuals are shown in Figure 5.8. The best-fit temperature in the *fil_all* region is significantly higher than that of the elongated knot (see Figure 5.7, Table 5.1 and Table 5.4). This confirms that the filament is indeed hotter than the elongated knot, as suggested by the image analysis. The Ne/O

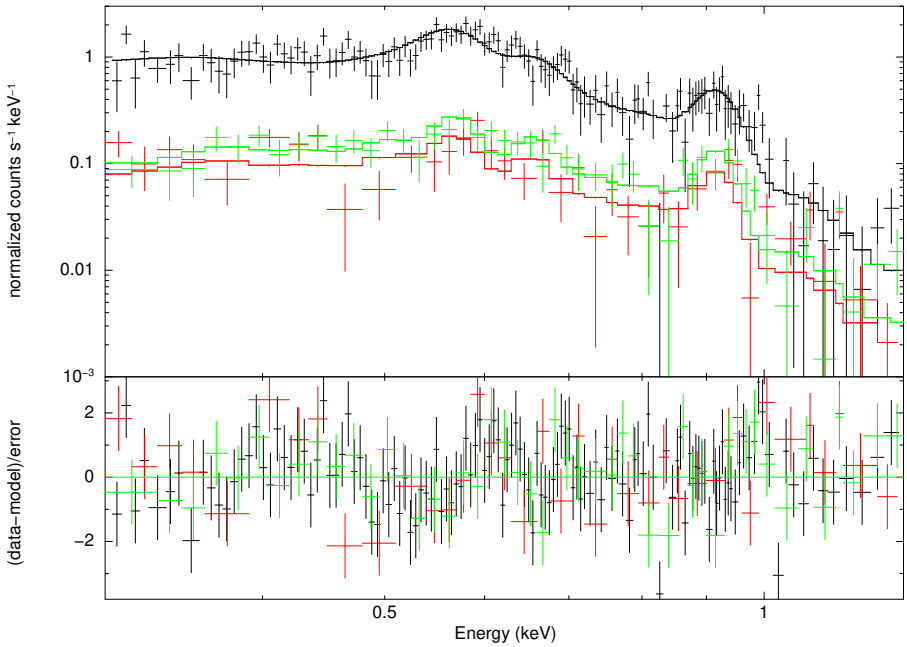

Figure 5.8: EPIC spectra (pn in black, MOS1 in red and MOS2 in green) extracted from the *fil_all* region (shown in Figure 5.5) with the corresponding CIE best-fit model and residuals in the 0.3 − 1.3 keV band.

Table 5.4: Filament spectra best-fit parameters with the CIE best-fit model (`vapec`).

Parameter	fil_all
kT (keV)	$0.174^{+0.002}_{-0.002}$
$O/O_{\odot}$	$0.48^{+0.07}_{-0.06}$
$Ne/Ne_{\odot}$	$1.9^{+0.4}_{-0.3}$
$n^2 l$ (10^{18} cm^{-5})	$0.93^{+0.12}_{-0.12}$
χ^2/d.o.f.	337.67/276

Notes. Errors are at a 90% confidence level.

ratio is significantly higher than that found for the knot ($Ne/O_{fil\_all} = 4.0^{+0.6}_{-0.8}$ versus $Ne/O_{Elong\_knot} = 2.6^{+0.4}_{-0.5}$), and it is also higher than that in the previously mentioned ejecta fragments. The different temperatures and abundances confirm the different nature

of the two plasma structures.

5.4 ROSAT results

5.4.1 Images

The filament that I found in the *XMM-Newton* observation runs from the upper right to the lower left corners of the instrument FoV (see the blue structure in Figure 5.2) and it may therefore be a part of a large-scale structure extending beyond the *XMM-Newton* FoV. I thus investigated the nature of this feature by analyzing RASS observations covering the whole western part of Vela SNR. In Figure 5.9 I show maps of photon counts of the western part of Vela SNR in the broad *ROSAT* bandpass (i.e., 0.1 – 2.4 keV) and in the 0.3 – 0.5 keV (soft) and 0.5 – 1.0 keV (hard) energy bands. In the *ROSAT* broad and soft band images, an extended filament running from north (at a position approximately corresponding to the projected location of the Puppis A SNR) to the south, and extending down exactly to the knot K region, is clearly visible. The extended filament blends with the surrounding emission in the 0.5 – 1.0 keV image.

5.4.2 Median photon energy maps

In Figure 5.10 I show the E_m map of the *ROSAT* RASS observation in the 0.3 – 1.3 keV energy band that I produced to further characterize the E_m of the extended filament. The image shows that the X-ray emission of the extended filament is less energetic than that of the surrounding plasma. Also, the whole structure is coherent in E_m on a very large spatial scale, comparable with the diameter of the shell. The relatively low E_m of the extended filament (450 – 550 eV, indicated by the blueish structure in Figure 5.10) presents only minor spatial variations that may not necessarily be caused by inhomogeneities in the plasma temperature. Variations in E_m of the soft energy band considered, in fact, may be associated with different values of the absorbing column density, which is expected to vary on these large spatial scales (Lu & Aschenbach 2000).

5.4.3 Spectra

The *ROSAT* image analysis suggests that the narrow filament detected in the *XMM-Newton* observation may be a portion of a much larger structure that clearly sticks out in Figure 5.9. I extracted the spectrum from the region indicated by the black polygon, labeled *Ext_fil*, in Figure 5.9; I also extracted the background spectrum from the circular region indicated in red in Figure 5.9. I fit the spectrum by adopting the best-fit model that I found for the *XMM-Newton* filament, that is CIE thermal emission from an isothermal plasma (`vapec`) with O and Ne abundances free to vary, and including the effects of

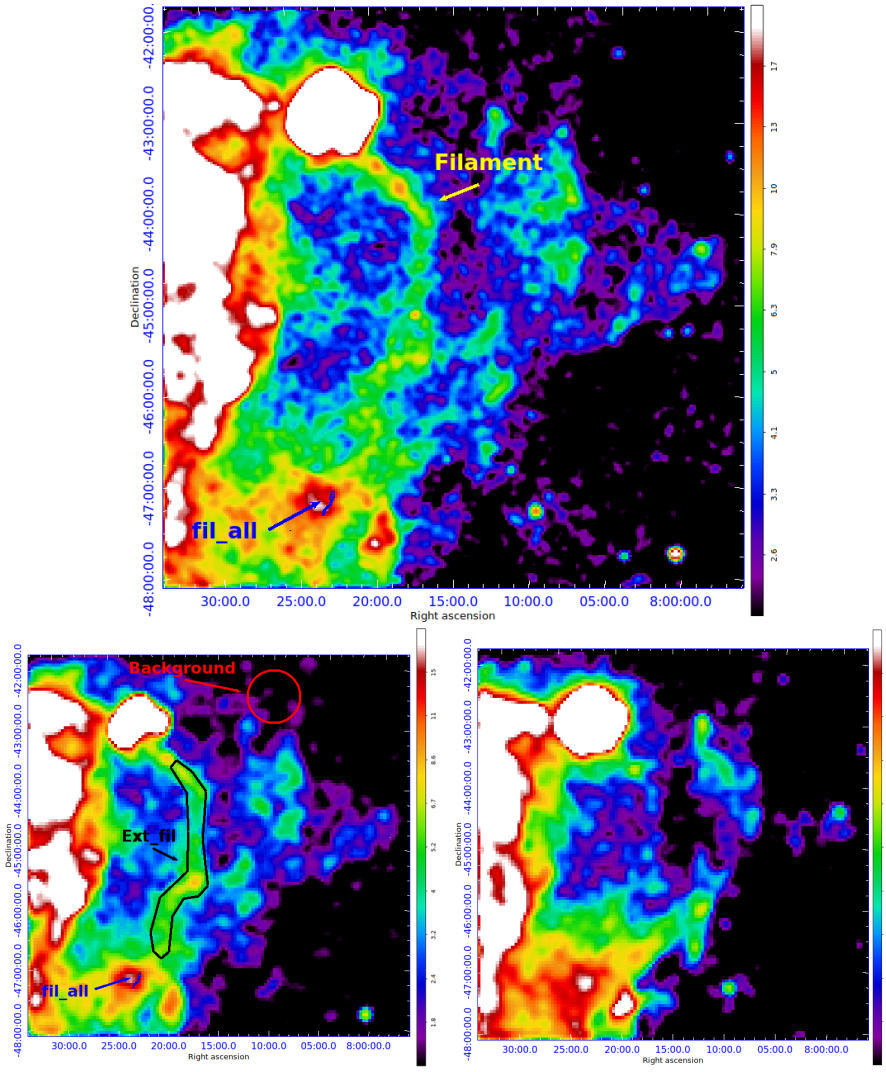

Figure 5.9: *Top panel*: *ROSAT* PSPC map of photon counts in the 0.1 – 2.4 keV energy band in squared root scale. The bin size is 1′. The map was smoothed through the convolution with a Gaussian with $\sigma = 3'$ (3 pixel). The *fil_all* spectral region (see Figure 5.5) is superimposed in blue. *Lower-left panel*: *ROSAT* PSPC map of photon counts in the 0.3 – 0.5 keV energy band in squared root scale, smoothed with $\sigma = 9'$. The bin size is 3′. The red circle indicates the background spectrum region, and the black polygon is the filament spectrum extraction region. The *fil_all* spectral region is superimposed in blue. *Lower-right panel*: *ROSAT* PSPC map of photon counts in the 0.5 – 1.0 keV energy band in squared root scale, smoothed with $\sigma = 9'$. The bin size is 3′.

ISM absorption (`tbabs`). Despite the poor *ROSAT* PSPC energy resolution, I were able to derive the best-fit parameters independently from the *XMM-Newton* spectral analysis

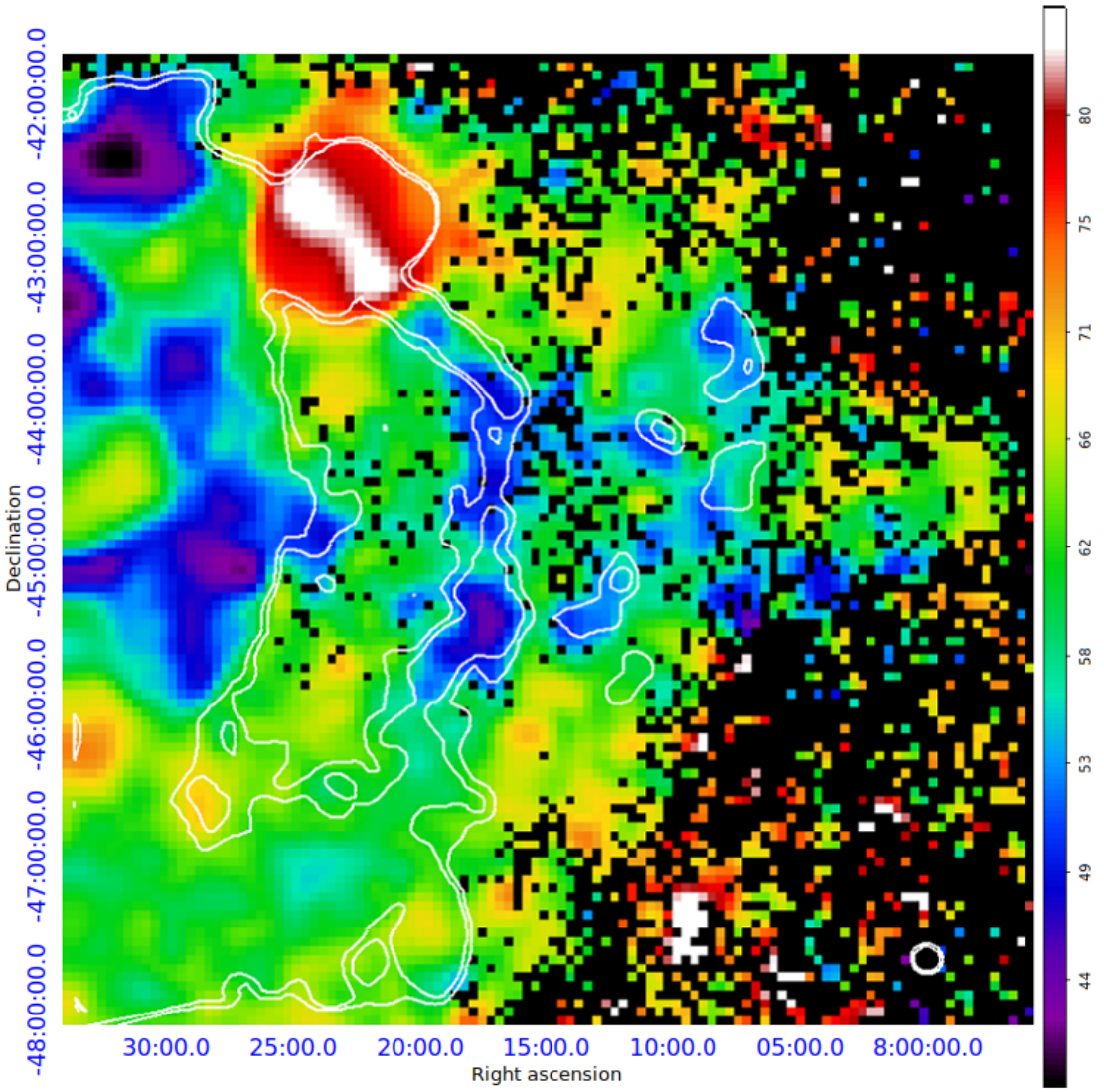

Figure 5.10: Median photon energy map of the western part of the Vela shell in the 0.3 – 1.3 keV energy band with a bin size of 3.5′ in linear scale. The scale is in units of 10 eV. White contours mark the photons' count number levels between 4 and 5 counts in the 0.3 – 0.5 keV energy band.

of the filament (see Table 5.5). The PSPC spectrum of *Ext_fil* with the corresponding best-fit model and residual is shown in Figure 5.11.

The best-fit temperature of the large filament is remarkably consistent with that obtained for the narrow filament in the *XMM-Newton* observation ($kT_{fil\_all} = 0.174^{+0.002}_{-0.002}$ $kT_{Ext\_fil} = 0.177^{+0.011}_{-0.016}$, see also Table 5.4 and Table 5.5 for comparison). It is important

Table 5.5: *ROSAT* filament best-fit.

parameter	Ext_fil
$N_{\rm H}$ (10^{22} cm^{-2})	$0.029^{+0.006}_{-0.004}$
kT (keV)	$0.177^{+0.011}_{-0.016}$
O/O$_\odot$	$0.22^{+0.09}_{-0.08}$
Ne/Ne$_\odot$	< 1.5
$n^2 l$ (10^{18} cm^{-5})	$0.017^{+0.005}_{-0.005}$
$\chi^2/d.o.f$	93.15/94

Notes. The abundance of O was frozen to the best-fit parameter in order to reduce the uncertainty of the kT parameter. The abundance of O was determined by freezing Ne abundance. Errors are at a 90% confidence level.

to note that Ne and O abundances are not well constrained because of the low energy resolution of the PSPC-C *ROSAT* spectra. Figure 5.12 shows the 68%, 95%, and 99.5% confidence contour levels of the Ne abundance versus the O abundance derived from the *ROSAT* spectrum of the large filament compared to the levels for the narrow filament in the *XMM-Newton* data. The plot shows that abundances are consistent within the 2σ (green) confidence level, thus confirming the homogeneous chemical composition of the filament. These results strongly indicate that the narrow filament is part of a coherent, bent, giant structure, running north-south behind the eastern rim of the Vela shell.

5.5 Discussions

5.5.1 Elongated Knot

In this Chapter, I have presented a detailed study of an *XMM-Newton* observation of a bright X-ray emitting clump, namely knot K, located behind shrapnel G in the southwestern region of Vela SNR (see Figure 5.1). By analyzing the *XMM-Newton* observation, I found an X-ray emitting plasma structure (predominantly in the 0.3 – 0.5 keV energy band, Figure 5.2), which is remarkably elongated in the direction connecting shrapnel A and shrapnel G (see Figure 5.3) (i.e., the only two Si-rich shrapnel detected in the Vela SNR so far). Furthermore, the elongated knot points toward the explosion site of the Vela SNR. This structure shows a soft thermal spectrum with non-solar abundances, as shown in Figure 5.6, and a temperature significantly lower than that of shrapnel A and G. Although the elongated knot has a low temperature that hampers the detection of over-solar Si abundance, I found that the Ne to O abundance ratio is consistent with that of shrapnel A (Katsuda & Tsunemi 2006) and shrapnel G (García et al. 2017).

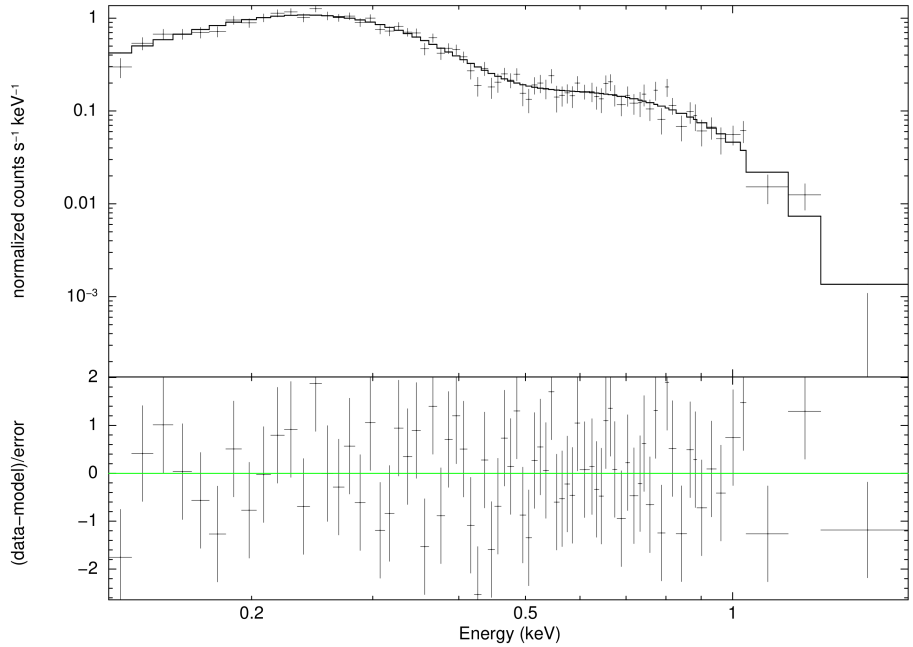

Figure 5.11: *ROSAT* PSPC-C spectrum of region *Ext_fil* (black polygon in Figure 5.9, *Lower left panel*) with the best-fit CIE model in the 0.3 − 1.8 keV energy band. The bottom panel shows the residual between the data and the model.

Moreover, the Si abundance I found (though poorly constrained) is consistent with that observed in those ejecta fragments. Enhanced Ne/O abundance ratios have also been observed in ISM clumps within the Vela SNR (Miceli et al. 2005, Katsuda et al. 2011), though with slightly lower values than those presented in Table 5.1. It is then possible that the elongated structure is a shocked ISM cloudlet. However, its highly elongated morphology seems to suggest an association with shrapnel G. Moreover, its chemical composition is consistent with being the same as that of shrapnel A and shrapnel G. In summary, my results show that a physical relationship between the jet-like elongated knot and the two Si-rich shrapnel is likely.

Assuming that the elongated knot has a cylindrical symmetry, I calculated the volume (V) of the X-ray emitting structure through the relation $V = \pi \frac{D^2}{4} l$ where l is the projected length of the elongated knot ($l \sim 5 \times 10^{18}$ cm) and D is its projected thickness ($D \sim 1 \times 10^{18}$ cm), thus obtaining $V \sim 4 \times 10^{54}$ cm^3. I point out that from the X-ray image, I can only measure the projected size of the features in the plane of the sky, so this

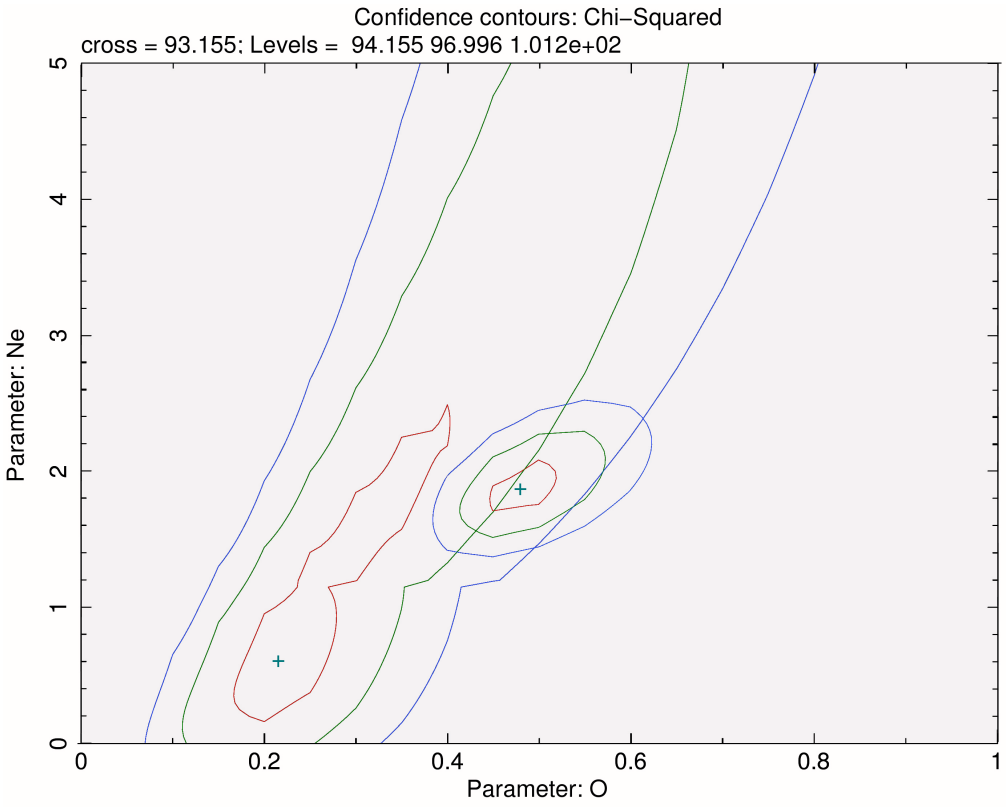

Figure 5.12: 68% (red), 95% (green), and 99.5% (blue) contour levels of the Ne abundance vs. O derived from the spectral analysis of the *Ext_fil* spectrum with the same contour levels of *fil_all* spectrum superimposed.

value should be considered as a lower limit. However, since the structure is close to the border of the shell, the actual value may not differ too much from the one reported here. Through the best-fit value of the plasma emission measure and volume, I estimated a number density of $\overline{n} = 1.20^{+0.05}_{-0.07}$ cm^{-3} for the elongated knot and a total mass of $M = 1.00^{+0.06}_{-0.04} \times 10^{31}$ g ($\sim 0.005 M_{\odot}$), using as average atomic mass $\mu = 2.1 \times 10^{-24}$ g (value for solar abundances). However this value is an upper limit since I expect oversolar chemical abundances[3].

Considering the projected distance between the explosion center of Vela SNR and the elongated knot and the age of the remnant ($\simeq$ 11000 yrs, Taylor et al. 1993), I obtained $v_k \sim 1.2 \times 10^8$ cm/s (1200 km/s) and a kinetic energy of $E_k = 7.2^{+0.3}_{-0.4} \times 10^{46}$ erg. However, if I take into account that the speed of the elongated knot decreases with

[3]The moderate spectral resolution of CCD spectrometers hampers the possibility of measuring absolute abundances and only reliable estimates of relative abundances can be obtained (see Greco et al. 2020).

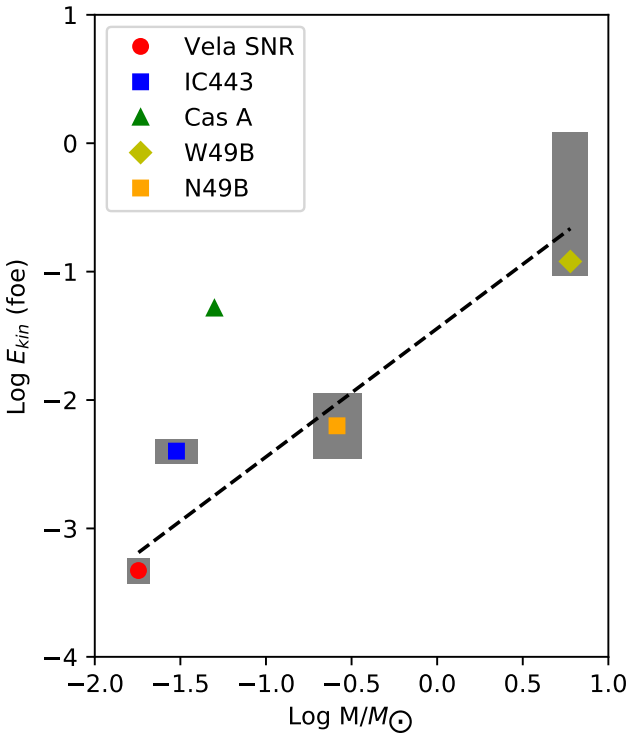

Figure 5.13: Kinetic energy vs. mass of the jet-like structure observed so far in core collapse SNRs. Kinetic energy is expressed in foe (1 foe = 10^{51} erg). Values are from this Chapter, Katsuda & Tsunemi (2006) and García et al. (2017) for Vela SNR, Greco et al. (2018) for IC443, Orlando et al. (2016) for Cas A, Park & Bhalerao (2017) for N49B and Miceli et al. (2008b) for W49B.

time and accounts only for the projected velocity, this value of kinetic energy should be considered as a lower limit. Values of mass and kinetic energy found for the elongated knot are very similar to those found for shrapnel G by García et al. (2017). By assuming that the elongated knot is part of a jet-counterjet-like structure with shrapnel A and G, its total mass and kinetic energy are $M = 0.018\ M_\odot$ and $E = 4.7 \times 10^{47}$ erg, respectively.

Similar jet-like features have been observed in a handful of CCSNRs and may be associated with anisotropies in the SN explosion (Miceli et al. 2013b, Tsebrenko & Soker 2015, Orlando et al. 2016, Bear & Soker 2018, Tutone et al. 2020). Miceli et al. (2008b) found an indication of a jet-like structure for the galactic SNR W49B with mass $M = 6M_\odot$ and $E = 1.2 \times 10^{50}$ (see also Lopez et al. 2013). However, it has been suggested that this collimated structure may not be intrinsic and may result from

a (nearly) spherical explosion in a barrel-like circumstellar environment (Miceli et al. 2008b, Zhou et al. 2011, Zhou & Vink 2018). Also the Cas A SNR, deeply analyzed by Hwang & Laming (2012), shows a jet of Si-rich plasma. Laming et al. (2006) suggest that its origin lies in an explosive jet. Detailed 3-D hydrodynamic simulations by Orlando et al. (2016) proved that this jet can be explained as the result of velocity and density inhomogeneities in the ejecta profile of the exploding star. According to these simulations, the mass and kinetic energy of the jet-counterjet structure in Cas A are $M = 0.05 M_{\odot}$ and $E = 5.2 \times 10^{49}$ erg, respectively. Park & Bhalerao (2017) found an elongated feature, which shows an overabundance of Mg, in the LMC SNR N49B, which they interpret either as the result of an SNR expanding into a nonuniform medium or as the result of an energetic jet-driven supernova. Another Mg-rich jet-like feature in the ejecta has been recently discovered in the SNR IC 443 by Greco et al. (2018) who identified a jet-like structure composed by plasma in overionization with mass and kinetic energy $M \sim 0.03 M_{\odot}$ and $E \sim 3 \times 10^{48}$ erg, respectively. A comparison between the Vela SNR and the other jet-like structures observed in CCSNRs shows a wide range of masses and energies, as shown in Figure 5.13. A simple linear regression gives $E = (4 \pm 2) \times 10^{49}$ erg $\cdot M/M_{\odot}$, but large residuals are present and the number of data points is too limited to get robust information. I conclude that the morphology, the position, and the spectral analysis strongly suggest that the elongated knot is part of a knotty, collimated ejecta structure and/or an ejecta trailing wake left behind the supersonic motion of shrapnel G.

5.5.2 Extended Filament

The 0.5 – 1.0 keV count-rate image of the *XMM-Newton* observation dominantly shows the emission of a narrow filamentary plasma structure (see Figure 5.2). The filament has a thermal spectrum (Figure 5.8) and its temperature is significantly higher than that of the elongated knot and uniform along its whole length (see Figure 5.4). The Ne to O ratio (Ne/O= $4.0^{+0.6}_{-0.8}$) is significantly higher than that of the elongated knot and, in general, than that of the ejecta fragments of Vela SNR. This indicates that the filamentary structure may have a different nature.

I demonstrated, thanks to the RASS data of Vela SNR, that this X-ray emitting plasma structure is the southern edge of a more extended filament that runs from the northern rim of the shell to knot K (see Figure 5.9). The extended filament is a giant X-ray emitting structure with a uniform temperature, whose physical and chemical properties are consistent with those measured in the *XMM-Newton* filament (as shown in Table 5.4, Table 5.5, and Figure 5.12). The projected length of this extremely long structure is $l \sim 6 \times 10^{19}$ cm. The distance between the explosion site and the extended filament shows relatively small variations, ranging from $\sim 4.5 \times 10^{19}$ cm to $\sim 5.5 \times 10^{19}$ cm.

As shown with the *ROSAT* results, this long filament is located well behind the border of the shell and its X-ray emission is softer than that of the forward shock (see Figure

5.10). Soft emission may be the result of an interaction with a dense environment, given that the shock speed scales as the inverse of the square root of the particle density and the post-shock temperature increases as the square of the shock speed. This indication, together with the almost circular shape, centered at the position of the SN progenitor, suggests that the filament may be a dense stellar wind-blown relic of the progenitor star heated by the shock wave.

Figure 5.10 also shows a high E_m belt running through the SNR Puppis A, exactly at the same position as the large-scale filament I analyzed in this Chapter. Hui & Becker (2006) suggest that this belt may be due to intervening absorbing material from Vela SNR. Dubner et al. (2013) present a comparison of the X-ray image of SNR Puppis A with the HI column distribution (Reynoso et al. 2003) that shows a stripe with enhanced hydrogen column density ($N_{\rm H} \sim 10^{21}$ cm^{-2}) in coincidence with the high E_m belt, suggesting that dense material might be responsible for absorbing soft X-ray photons. Given the spatial coincidence of the large scale filament with the high absorption feature in Puppis A, it may be possible that the filament, together with the X-ray emitting plasma, also includes cooler and denser material, which may be responsible for such a large absorption. This scenario surely requires further investigation of the lower energy emission from this feature.

In this scenario, the filament can be considered as the projection on the plane of the sky of a nearly spherical shell, likely a wall of a wind-blown bubble. Given the poor spatial resolution of the *ROSAT* telescope, the width of the shell can be estimated by the *XMM-Newton* data only (i.e., only in the southern edge of the filament) and is $W \sim 2 \times 10^{17}$ cm. In the following, I assume that this is the width along the whole filament. I estimate the volume of the X-ray emitting plasma within the photon extraction regions, which I approximated as the volume intercepted by the extraction region on two spherical shells (having width W) and different radii, $r_1 = 5.0 \times 10^{19}$ cm and $r_2 = 4.3 \times 10^{19}$ cm. This can be done by adopting the procedure described in Miceli et al. (2012, see their Appendix A).

I obtain a density $n_{fil} \sim 0.182^{+0.020}_{-0.015}$ cm^{-3} for the whole filament (region *Ext_fil* in Figure 5.9, analyzed with *ROSAT*) and $n_{fil} \sim 0.40 \pm 0.02$ cm^{-3} for the southern edge of the filament (region *fil_all* in Figure 5.5, analyzed with *XMM-Newton*). This may indicate small (within a factor of ~ 2) spatial variations in the shell density and/or variations in its width (the assumption of a uniform width may not be strictly valid and this may affect the density estimate). By considering an average density $n_{fil} = 0.2$ cm^{-3}, I also estimated the mass of the spherical shell blown by the wind with external radius $R_{ext} = 4.49 \times 10^{19}$ cm and internal radius $R_{int} = 4.47 \times 10^{19}$ cm, thus finding $M_{shell} = 2.5^{+0.3}_{-0.2} \times 10^{33}$ g ($1.26^{+0.15}_{-0.10}\ M_{\odot}$).

Considering the projected average distance between the explosion center of Vela SNR and the forward shock in the western region, I obtained a velocity of $v \sim 2 \times 10^3$ km s^{-1}. Using this velocity and considering an average distance from the explosion

center ($r_{shell} \sim 5 \times 10^{19}$ cm), I found that the shock interacted with the filament structure approximately 8 kyr after the explosion. This value is an upper limit value. Indeed, the filamentary structure was probably dragged by the interaction with the forward shock. It is also possible to get an estimate of the age of this putative wind-blown structure. By using the r_{shell} value and the characteristic speed of stellar winds in a red supergiant ($\sim$ 10 km/s), I determined that the progenitor star started to blow this wind (i.e., entered in its red supergiant phase) $\sim$ 1.6 Myr ago. The onset of the red supergiant phase typically precedes the explosion by 0.5 – 2 Myr; therefore, my time estimate is quite reasonable and strongly supports the interpretation of the filament as a wind-blown structure produced by the progenitor star.

On the other hand, the high Ne/O ratio suggests peculiar abundances for this putative wind-blown shell. A possible explanation for a high Ne/O ratio can be O depletion. In layers where the CNO cycle is active, the O abundance strongly decreases (while Ne abundance stays steady). Therefore, large Ne/O abundance ratios are expected in the inner part of the H layer of a massive star. To blow a wind with enhanced Ne/O abundances, it is then necessary for the star to lose its H envelope, as occurs in Wolf-Rayet stars (WNL-WNE). A Wolf-Rayet star can blow a fast wind that can reach, and impact, the previously ejected material, thus forming a shell with enhanced Ne/O abundances, similar to what I observed (Chieffi & Limongi 2013, Limongi & Chieffi 2018). In order to test this scenario, it would be necessary to measure the N and C abundances in the wind-blown shell. Unfortunately, I cannot obtain significant constraints on these abundances with my data and further investigations are necessary. The detection of a wind-blown relic, in any case, can convey important information on the progenitor star of Vela SNR.

6

Probing Shocked Ejecta in SN 1987A: A novel diagnostic approach using XRISM−Resolve

Abstract

SN 1987A is one of the best candidates to exploit the capabilities of the freshly launched XRISM satellite. This celestial object offers the unique opportunity to study the evolution of a SN into a young supernova remnant. To date, the X-ray emission has been dominated by the shocked CSM, with no shocked ejecta firmly detected. However, recent studies provide compelling evidence that in the forthcoming years the X-ray emission from SN 1987A will increasingly stem from the ejecta. My aim is to assess the proficiency of XRISM-Resolve high resolution spectrometer in pinpointing signatures of the shocked ejecta in SN 1987A. Taking advantage of a self consistent state-of-art MHD simulation that describes the evolution from SN 1987A to its remnant, I synthesized the XRISM-Resolve spectrum of SN 1987A, as it would be collected in the allocated observation during the performance verification phase, which is foreseen for 2024. My predictions clearly show the leading role of shocked ejecta in shaping the profile of the emission lines. The Doppler broadening associated with the bulk motion along the line of sight of the rapidly expanding ejecta is shown to increase the line widths well above the values observed so far. The quantitative comparison between my synthetic spectra and the XRISM spectra will enable us to establish a strong connection between the broadened line emission and the freshly shocked ejecta. This, in turn, will allow us to retrieve the ejecta dynamics and chemical composition from the X-ray emission.

Part of the work presented in this Chapter has been published under the title "*Probing Shocked Ejecta in SN 1987A: A novel diagnostic approach using XRISM−Resolve*" in the scientific journal "The Astrophysical Journal Letters, Volume 961, id. 9" (Sapienza

et al. 2024, DOI: https://doi.org/10.3847/2041-8213/ad16e3).

6.1 Introduction

Situated at 51.4 kpc (Panagia 1999) in the Large Magellanic Cloud (LMC), SN 1987A is the relic of a CCSN discovered on February 23rd, 1987 (West et al. 1987). The SNR is evolving in a highly inhomogeneous CSM. The CSM is characterized by a dense and clumpy equatorial ring (ER) structure embedded within a diffuse H II region (Sugerman et al. 2005). SN 1987A offers, for the first time in modern astronomy, the opportunity of resolving the evolution of a SN into its SNR through all the wavelengths of the electromagnetic spectrum (McCray & Fransson 2016), being an *unicum* in this field.

Observations in the X-ray band play a pivotal role in probing the interaction between the shock front and both the CSM and the external envelope of ejecta, as well as in studying shock physics. Hard (10 – 30 keV) X-ray emission in the region of SN 1987A was first detected six months after the explosion (Dotani et al. 1987). Subsequently, ROSAT observed a soft (0.1 – 2.4 keV) X-ray thermal emission $\sim$ 1500 days after the explosion (Beuermann et al. 1994). Since the initial detection, the X-ray emission has continuously increased for about 25 yrs, and its nature has been investigated by several studies, confirming the encounter of the shock with the equatorial ring (Borkowski et al. 1997,Park et al. 2005, Haberl et al. 2006, Zhekov et al. 2009, Maggi et al. 2012). Recent investigations in the past few years, showed that the soft X-ray emission (0.5 – 2 keV) is decreasing, while the harder component (3 – 8 keV) continues to increase (Frank et al. 2016, Sun et al. 2021, Ravi et al. 2021, Maitra et al. 2022). Additionally, indications of a Pulsar Wind Nebula (PWN), embedded in the dense and cold innermost ejecta, were found by Greco et al. (2021, 2022) in the 10 – 20 keV band (see also Fransson et al. 2024).

The overall X-ray light-curve has been impressively replicated by 3D HD and MHD simulations by Orlando et al. (2015, 2019, 2020). These simulations offer valuable insights into the temporal evolution of the X-ray emission. They indicate that the X-ray emission was initially dominated by the shocked H II region. However, as time progressed, a notable transition occurred, with the emission becoming increasingly influenced by the shocked dense ER. According to the models, the remnant is currently entering a third phase, where the X-ray emission is predominantly driven by the SN outermost ejecta, heated by the reverse shock. Therefore, X-ray features from the shocked ejecta are expected to be observed in the near future.

In a pioneering study, Miceli et al. (2019) introduced a novel data analysis approach for examining the case of SN 1987A. They analyzed the *Chandra* High Energy Transmission Grating data from 2007 and 2011 comparing them with the 3D HD simulation presented by Orlando et al. (2015). Since the simulation is able to reproduce self-consistently the whole broadening (due to the thermal motion of ions and to bulk motion

along the line of sight) of the spectral lines, they were able to deduce the post shock temperature of protons and ions through the comparison of the model with observation (see also Miceli 2023, Ravi et al. 2021).

The JAXA-NASA collaborative mission X-ray Imaging and Spectroscopy Mission (XRISM, Tashiro et al. 2020), launched on September 7th 2023, with the Resolve spectrometer (Ishisaki et al. 2022) will offer non-dispersive, high-resolution X-ray spectroscopy at <7 eV (this was the goal before launch) energy resolution with a large effective area around 6 keV (for further details, see Sect. 2.5). These capabilities open the door for in-depth investigations of young remnants like SN 1987A. Moreover, the XRISM mission will observe it in the Performance Verification (PV) phase.

Leveraging an in-house developed tool, I synthesize the XRISM-Resolve X-ray spectrum of SN 1987A from the MHD simulations by Orlando et al. (2020) and Ono et al. (2020), which have been proven to accurately reproduce the observables obtained from current telescopes. I adopt an approach similar to Miceli et al. (2019), and aim at finding new diagnostics to trace ejecta signatures for the forthcoming observations of SN 1987A.

The structure of this Chapter is as follows: Section 6.2 presents the model and details the spectral synthesis process, while Section 6.3 showcases the results obtained from the synthesized models. In Section 6.4 I discuss the possible XRISM-Resolve detection of the the ^{44}Sc emission line. Discussions and conclusions are drawn in Section 6.5.

6.2 Model and synthesis procedure

For my spectral synthesis, I harness the 3D MHD model by Orlando et al. (2020). This state-of-the-art simulation models the evolution of SN 1987A (both ejecta and CSM) from the immediate aftermath ($\sim$ 20 hours) of the 3D core-collapse model provided by Ono et al. (2020). I adopted the model configuration that best matches the observations for the progenitor star, the SN, and the SNR (B18.3 in Orlando et al. 2020 and hereafter). The progenitor star model for this configuration was proposed by Urushibata et al. (2018). It implies a 18.3 $M_{\odot}$ blue supergiant progenitor, resulting from the slow-merging (Ivanova et al. 2002) of two massive stars with 14 $M_{\odot}$ and 9 $M_{\odot}$. This model can reproduce the luminosity and surface temperature of the progenitor star of SN 1987A. The evolution from the progenitor to the CCSN was then followed by Ono et al. (2020), and then evolved into SNR by Orlando et al. (2020). The B18.3 model reproduces the X-ray light-curves and the evolution of the size and morphology of the X-ray emitting structures of remnant of SN 1987A. Moreover, it is able to reproduce the evolution of the X-ray spectra (Miceli et al. 2019), as well as the observed velocity distributions of ^{44}Ti (Boggs et al. 2015) and ^{56}Fe (Haas et al. 1990) and the spatial distribution of the SiO and CO molecules (Abellán et al. 2017).

Figure 6.1 (upper panels) shows the distribution of the EM of the X-ray emitting

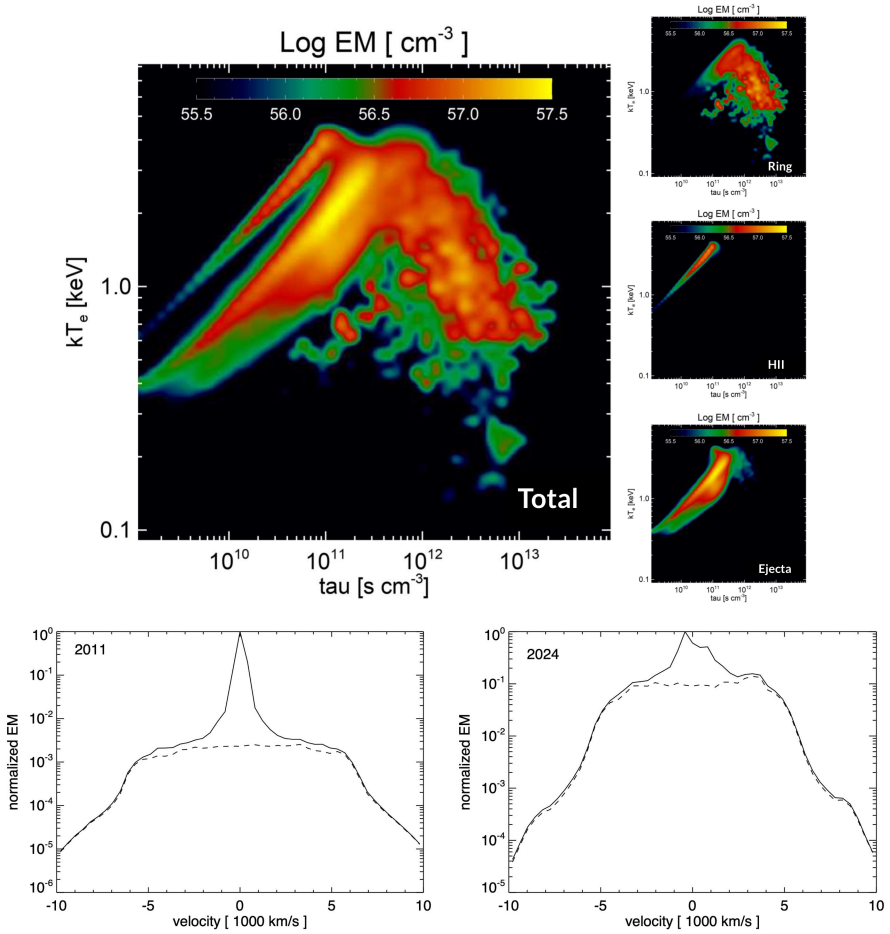

Figure 6.1: *Upper Left panel:* Distribution of EM for the total X-ray emitting plasma in SN 1987A as a function of the plasma temperature and ionization parameter, as predicted by my MHD model for year 2024. *Upper Right panels:* Same as left panel for the ER, H II region and ejecta from top to bottom, respectively. *Lower left panel:* Normalized EM distribution as a function of the velocity along the line of sight for year 2011. Black solid line marks the total EM, while the black dashed line marks the contribution of the ejecta. Negative velocity are towards the observer. *Lower right panel*: Same as *lower left panel* for the year 2024

plasma as a function of the electron temperature kT and of the ionization parameter τ (i.e., the time integral of the electron density computed from the impact with the shock front, see Section 1.3.3), as predicted by my model of SN 1987A for year 2024. The panels on the upper-right show the contribution to the EM from the ER, the H II region and the ejecta, respectively from top to bottom. The contribution to the EM from the ejecta (which are moving faster than the CSM, see lower panels of Figure 6.1) shows the

highest increase (compared to the ER and H II region) with respect to previous epochs (see Ravi et al. 2021; Greco et al. 2022). It is also worth noting that the ER shows values of τ that are, on average, higher than that of the ejecta.

To self-consistently synthesize the thermal X-ray emission from the 3D MHD simulation, I employ an in-house developed tool in a similar fashion as Miceli et al. (2019), Greco et al. (2020), and Miceli (2023). In each cell of the computational domain I derive the value of electron and proton temperature, electron density and τ. I use the aforementioned quantities as input parameters for the NEI optically thin plasma model `vnei` from XSPEC (Arnaud 1996) (version 12.12.0, ATOMDB version 3.0.9). I include the effects of the interstellar and intergalactic absorption by using the `tbabs` model in XSPEC, with an equivalent column density $n_H = 0.235 \times 10^{20}$ cm^{-2} as in Park et al. (2006). The X-ray emission models, folded through the response matrix with an energy resolution of 7 eV[1] (High resolution grade only) of XRISM-Resolve, are calculated using XSPEC for different values of electron temperature and ionization time, and stored in a look-up table. In this part of the Chapter, I consider the nominal XRISM-Resolve effective area (i.e., with the gate valve open). Results with the gate valve closed are presented in Section 6.3.1.

The MHD simulation shows that in 2024 the bulk of shocked ejecta belongs to the outer mantle (which is mainly composed of H and He, Ono et al. 2020). For the spectral synthesis, I assume that this external envelope of ejecta has the same chemical composition as the CSM. In particular, I adopt the abundances of Zhekov et al. (2009). Though also a fraction of metal-rich ejecta is expected to be shocked in 2024, I estimate from the simulation that their contribution to the ejecta X-ray emission is less than 0.0001% of the total, so I will not consider it in this Chapter.

My tool incorporates the ability to add in the spectral synthesis the line broadening arising from the bulk velocities along the line of sight of the different X-ray emitting parts of the remnant, namely: ejecta and CSM (ER and H II region). In addition to this effect, I also include the thermal broadening arising from the thermal motion of the ions in the plasma. To this end, I assume the ion temperature to be mass-proportional with respect to the proton temperature (Miceli et al. 2019; Miceli 2023). Once obtained the complete spectral model by summing cell by cell the computed spectra, I applied a Poissonian randomization to synthesize the spectra.

6.3 Results

As an initial step, I generate the XRISM-Resolve spectrum of SN 1987A, without applying any broadening effects, for the year 2024, to highlight the effects of broadening,

[1] I adopted the response matrix available at the XRISM-JAXA Researchers website (https://xrism.isas.jaxa.jp/research/proposer/obsplan/response/index.html)

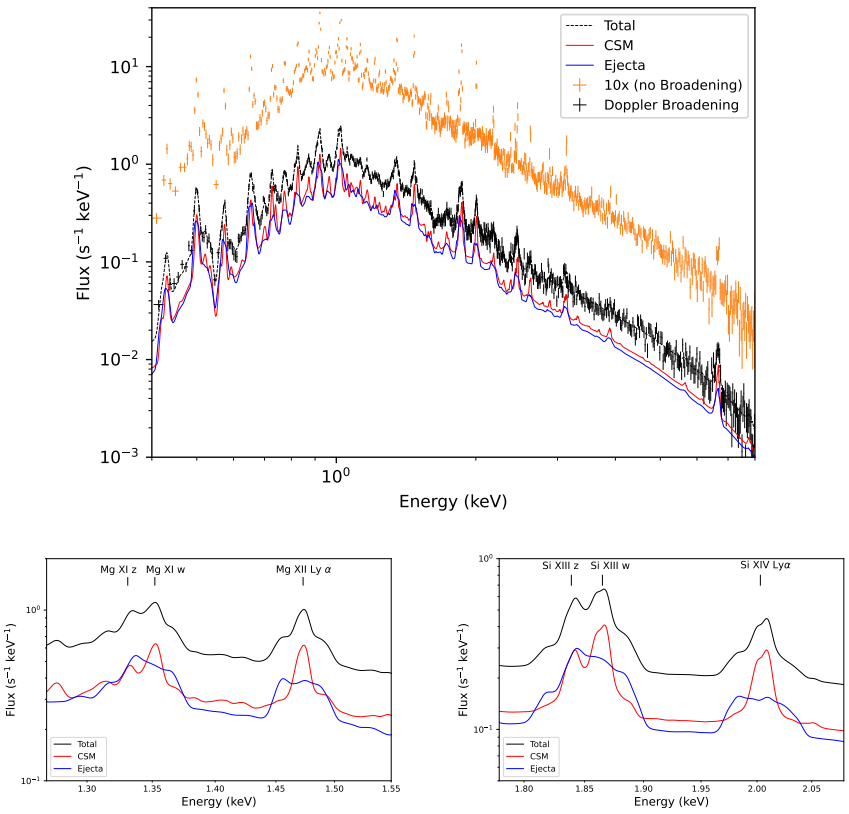

Figure 6.2: *Upper panel:*Synthetic XRISM-Resolve spectra of SN 1987A for the year 2024 with an exposure time of 100 ks. The orange spectrum was synthesized without any broadening effects except for the instrumental broadening, and it was multiplied by a factor 10 for visualization purposes. The black spectrum was synthesized including bulk motion Doppler broadening. All spectra are binned using the Kaastra & Bleeker (2016) optimal binning algorithm. The synthetic XRISM-Resolve spectral model is superimposed with a black dashed line. The red curve shows the contribution of the CSM (ER and H II) to the spectral model, while the blue curve shows the contribution of the ejecta. *Lower left panel:* Close-up view of the spectral model shown in upper panel in the 1.27 – 1.55 keV band. *Lower right panel:* Same as left panel in the 1.78 – 2.08 keV band.

shifts, and blending of emission lines by comparing this spectrum with the one including all broadening effects. I assume an exposure time of 100 ks, mirroring the allocated time granted for the PV phase of the mission (before launch). The resulting spectrum is presented in Figure 6.2 (upper panel, orange crosses).

Next, I introduce the broadening and shift effect caused by the bulk motion of the

plasma, the black spectrum in Figure 6.2 (upper panel) illustrates the outcome of this operation. The Doppler effect significantly broadens the emission lines, giving rise to complex profiles and line blending. These intricate and extensively broadened emission lines reflect the presence of different contributions from the different parts of the remnant in shaping the observed profiles. Figure 6.2 also shows the total spectral model (black dashed curve) for the X-ray emission from SN 1987A, as seen by XRISM-Resolve, and its ejecta (blue curve) and CSM (red curve) component. The contribution to the emission from the ejecta is comparable to the contribution from the CSM, as already noted in Orlando et al. (2020).

Figure 6.2 (lower panels) shows a close up view of the spectral model in the Mg (lower left panel) and Si (lower right panel) emission lines energy bands, respectively. The Mg XII Lyα and the Si XIV Lyα lines, being quite isolated, are the perfect probe for examining the line profile. The line profile, indeed, presents a composite structure with broad wings and a relatively narrow peak. The broad line wings are clearly associated with the rapidly expanding ejecta, whose emission is marked by the blue curve in Figure 6.2. The narrow and slightly blue shifted central peak reflects the CSM contribution (see the red solid curve in Figure 6.2) to the emission. The Mg XI w, z and the Si XIII w, z emission lines, instead, exhibit a broader and blended profile, with a dominating influence of the ejecta in shaping the X-ray emission compared to the CSM. I do not consider the Mg XI x, y and the Si XIII x, y lines because it can be seen from the spectrum without broadening (Figure 6.2, upper panel, orange crosses) that they do not contribute significantly to the X-ray emission. This pronounced effect can be primarily attributed to the ionization state of the ejecta, which are freshly shocked, and therefore heavily under-ionized (as shown in Figure 6.1). Consequently, their contribution to the emission of less ionized species, such as the Mg XI w, z and Si XIII w, z lines, is higher than in lines of H-like ions.

To point out the time evolution of the ejecta contribution to the X-ray emission predicted by the MHD model, I show in Figure 6.1 (lower panels) the distribution of the EM of the X-ray emitting plasma as a function of the plasma velocity along the line of sight in 2011 and 2024. The comparison between the 2011 and 2024 distributions underscores significant differences between these two epochs. The EM of the CSM has increased by a factor of $\sim 2-3$, accompanied by a slight blue shift of its peak, due to the random distribution of dense clumps in the ring, which may have coincidentally placed one or two dense clumps in the blue-shifted portion of the ring. In 2024, a large contribution to the line broadening arises from the freshly shocked and fast moving outer ejecta. Indeed, the actual contribution to the X-ray emission from the ejecta in SN 1987A has been observed increasing year by year, as attested by Sun et al. (2021) and Maitra et al. (2022). This is also clearly visible in Figure 6.1 (lower panels), where the contribution of the ejecta has increased by about 2 orders of magnitude from the year 2011 to the year 2024.

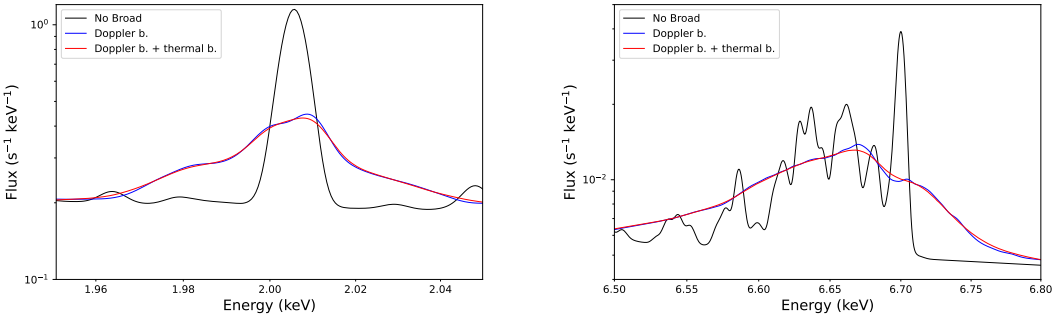

Figure 6.3: *Left panel:* Close-up view of the synthetic X-ray spectral model of SN 1987A for the Si XIV Lyα emission line. The figure displays the spectrum synthesized in three ways: the black curve without including Doppler and thermal broadening, the blue curve synthesized by considering only Doppler broadening, and the red curve synthesized by accounting for both Doppler and thermal broadening. *Right panel:* same as left panel for the Fe XXV emission lines complex.

I then synthesize the XRISM-Resolve spectrum of SN 1987A, adding the contribution of the thermal broadening to that of the Doppler broadening. I here focus on two emission lines: the Si XIV Lyα line to have a comparison with previous studies (Miceli et al. 2019, Miceli 2023) and the Fe XXV w, x, y, z lines (hereafter, Fe XXV lines complex), to explore the unprecedented capability of resolving the thermal broadening at high energy provided by this new instrument. I do not discuss here the line emission of H-like iron (Fe XXVI Lyα), which could have been a much more simple probe for the thermal broadening, because it does not emerge from the continuum (see Figure 6.2). Figure 6.3 shows a comparison between the synthetic spectrum considering the Doppler broadening and the synthetic spectrum including also the thermal broadening, for the Si XIV Lyα line (left panel) and the Fe XXV lines complex (right panel). From both the plots it is clear that, by adding the thermal broadening contribution to the spectrum, the shape of the emission line does not change significantly. A direct comparison between the Si XIV Lyα emission lines in 2007, 2011 (Miceli et al. 2019) and 2018 (Ravi et al. 2021; Miceli 2023) with those from this work, shows that in 2024 the Doppler broadening is expected to increase so much (because of the increased emission from the fast moving ejecta) that the relative contribution of thermal broadening is predicted to become negligible.

Hereafter, I show how the effect of the ejecta dynamics can be revealed in the forthcoming 100 ks XRISM-Resolve observation of SN 1987A, which will unveil the role of the ejecta in shaping the line profiles shown in Figure 6.2. I adopt four Gaussian components, added to a thermal continuum (I also include the effect of interstellar and intergalactic absorption) to model the synthetic emission lines of Mg (Figure 6.4, left

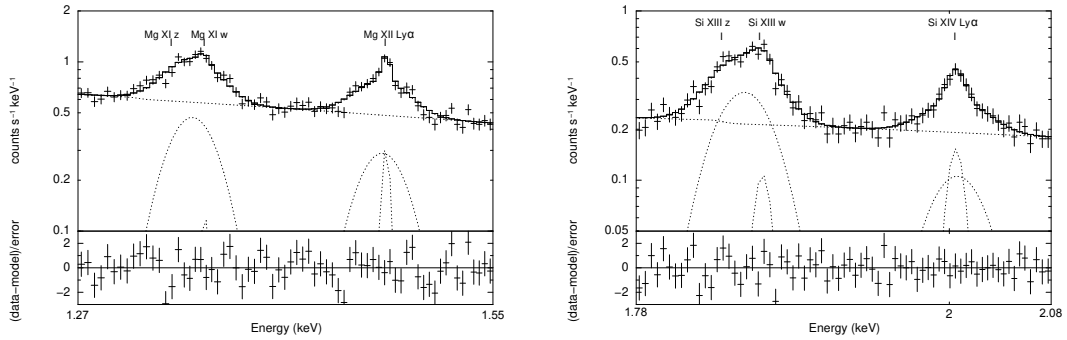

Figure 6.4: *Left panel:* Close-up view of the synthetic XRISM-Resolve spectrum (Figure 6.2, black crosses) highlighting the Mg XI w, z and Mg XII Lyα lines (1.27 – 1.55 keV band), with the corresponding best-fit model and residual. *Right panel:* Same as left panel for the Si XIII w, z and Si XIV Lyα lines (1.78 – 2.08 keV band).

panel) in the 1.27 – 1.55 keV band. I follow the same approach to model the Si lines (Figure 6.4, right panel) in the 1.78 – 2.08 keV band. I include these lines in my fitting procedure to accurately constrain the broadening of the lines stemming from the ejecta (which dominates the emission for He-like ions, see Figure 6.2) and from the CSM (which are visible in the emission of H-like ions). Specifically, two Gaussian lines model the narrow CSM components respectively, in the lines of H-like ions (i.e. Mg XII Lyα and Si XIV Lyα), and the He-like ions (i.e. Mg XI w and Si XIII w). The other two Gaussian lines are adopted to model the broad ejecta components in the lines of He-like and H-like ions. Given $\sigma_{3,1}$ and $E_{3,1}$ the width and the centroid of the ejecta components in the lines of He-like and H-like species, respectively, I impose $\sigma_1 = \sigma_3 \cdot E_1/E_3$ in the fitting procedure. Similarly, I impose $\sigma_2 = \sigma_4 \cdot E_2/E_4$, being $\sigma_{4,2}$ and $E_{4,2}$ the width and the centroid of the CSM components in the lines of He-like and H-like species.

Figure 6.4 shows the spectra of the Mg (left) and Si (right) lines with the corresponding best fit models and residuals. The best fit values with error bars at the 90% confidence level, are reported in Table 6.1. The different components (#1, #3, #4 in Table 6.1) are detected with high significance (their normalization being larger than zero at more than the 4σ confidence level) and clearly show different expansion velocities for CSM and ejecta. The #2 lines in Table 6.1 are detected with 2σ confidence level for the Mg XI w and 3σ confidence level for the Si XIII w confidence level.

I caution the reader that in the procedure described above I opt for a single Gaussian line to characterize the He-like ejecta triplets. The introduction of additional Gaussian lines for the He-like triplets is not statistically necessary and does not enhance the quality of the fit significantly. Nevertheless, I verify that the line broadenings reported in Table

Table 6.1: Best-ft values for the synthetic spectrum in the Mg and Si energy bands and the velocities retrieved from the Doppler broadening.

#	Emission line	Energy (keV)	σ (eV)	Velocity (km s^{-1})	Norm (cm^{-2} s^{-1})
		Mg $C-stat/d.o.f.=85.09/61$			
1	Mg XI w, z	$1.3440^{+0.0018}_{-0.0014}$			$8.0^{+0.6}_{-0.7}\times10^{-5}$
2	Mg XI w	$1.352^{+0.007}_{-0.007}$			$0.4^{+0.3}_{-0.3}\times10^{-5}$
3	Mg XII Lyα	$1.4709^{+0.0017}_{-0.0022}$	$17.7^{+1.2}_{-0.7}$	3610^{+240}_{-140}	$4.5^{+0.5}_{-0.5}\times10^{-5}$
4	Mg XII Lyα	$1.4734^{+0.0010}_{-0.0010}$	<3	<600	$0.9^{+0.2}_{-0.2}\times10^{-5}$
		Si $C-stat/d.o.f.=62.79/63$			
1	Si XIII w, z	$1.8543^{+0.0014}_{-0.0015}$			$6.9^{+0.5}_{-0.5}\times10^{-5}$
2	Si XIII w	$1.867^{+0.002}_{-0.004}$			$0.7^{+0.4}_{-0.3}\times10^{-5}$
3	Si XIV Lyα	$2.005^{+0.005}_{-0.004}$	$21.1^{+1.4}_{-1.3}$	3160^{+210}_{-190}	$2.2^{+0.4}_{-0.6}\times10^{-5}$
4	Si XIV Lyα	$2.0047^{+0.0019}_{-0.0020}$	$5.3^{+1.9}_{-1.5}$	800^{+300}_{-200}	$1.1^{+0.5}_{-0.3}\times10^{-5}$

Notes. Error bars are at 90% confidence level.

6.1 are not affected by this issue and are robust. To this end, I consider a spectral model including all the lines (i.e. three lines for the He-like triplets and one line for the H-like emission, for both the ejecta and CSM components). Though with the statistics provided by a 100 ks observation it is not possible to constrain such a large number of free parameters, I can determine the line centroids and normalizations from my simulation by considering a synthetic spectrum with an unrealistically high exposure time ($t_{exp} = 10^8$ s). I then find that the line widths for the ejecta remain consistent within the error bars with those shown in Table 6.1, which then provide reliable values for the velocity of ejecta and CSM.

6.3.1 Gate Valve Closed Updated Spectra

As explained in Sect. 2.5, the XRISM Telescope safety gate valve for the Resolve instrument has not opened so far. As a consequence, the effective area of XRISM-Resolve results degraded, as shown in Figure 2.5 (right panel). Following the same procedure described in Sect. 6.2, I produced the synthetic spectrum of SN 1987A for the year 2024, using the new RMF and ARF files that take into account the effects of the gate valve closed, available in the HEASARC XRISM website[2].

Right panel of Figure 6.5 shows the updated version of Figure 6.2, for an exposure time of 160 ks, which is the amended exposure time for the PV phase observation of SN 1987A, increased with respect to the original 100 ks to compensate the loss of effective area. Unfortunately, the effective area below 2 keV is severely compromised, hampering me to carry on the diagnostic procedure for the Mg and Si emission lines. However,

[2] https://heasarc.gsfc.nasa.gov/docs/xrism/proposals/responses.html

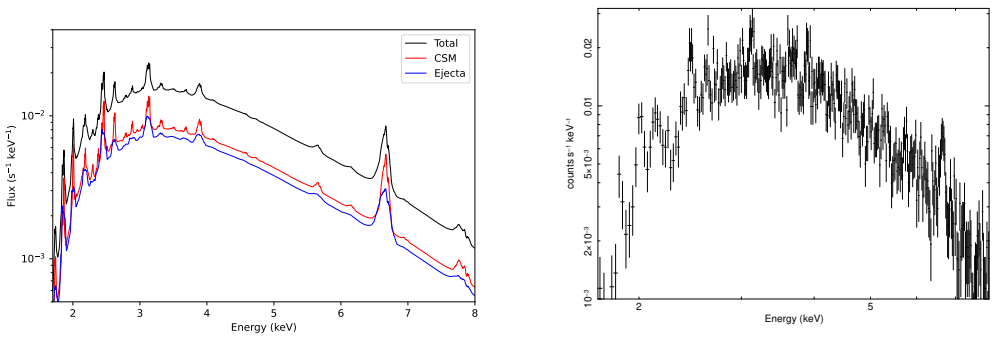

Figure 6.5: *Left panel:* Synthetic XRISM-Resolve spectral model including the effects of the gate valve closed (black solid line, including Doppler broadening). The red curve shows the contribution of the CSM (ER and H II) to the spectral model, while the blue curve shows the contribution of the ejecta. *Right panel:* Updated synthetic XRISM-Resolve spectrum with a 160 ks exposure time.

Table 6.2: Best-ft values for the synthetic spectrum in the S energy bands and the velocities retrieved from the Doppler broadening.

#	Emission line	Energy (keV)	σ (eV)	Velocity (km s^{-1})	Norm (cm^{-2} s^{-1})
		S $C-stat/d.o.f. = 63.43/73$			
1	S XV w-z	$2.458^{+0.007}_{-0.008}$	27^{+7}_{-6}	3300^{+800}_{-700}	$8.2^{+2.0}_{-1.8} \times 10^{-4}$
2	S XVI Lyα	$2.614^{+0.010}_{-0.009}$			$7.1^{+2.0}_{-1.8} \times 10^{-4}$

Notes. Error bars are at 90% confidence level.

the quality of the spectrum remains adequate for applying the same diagnostics to the S lines. I then fitted the S line profiles adopting only 2 broad Gaussian components (due to the reduced statistic), for the S XV w-z and for the S XVI Lyα, modeling the continuum emission with a power law and accounting for the interstellar and intergalactic absorption. Similarly to Section 6.3 $\sigma_2 = \sigma_1 \cdot E_2/E_1$, being $\sigma_{1,2}$ and $E_{1,2}$ the width and the centroid of the ejecta components in the lines of He-like and H-like species. Figure 6.6 shows a close-up view of the synthetic spectrum highlighting the S lines with the corresponding best fit model and residuals. The best fit values with error bars at the 90% confidence level, are reported in Table 6.2. The different components (#1 and #2 in Table 6.2) are detected with high significance (their normalization being larger than zero at more than the 5σ confidence level) and clearly show a large expansion velocity, which nicely accounts for the ejecta bulk motion.

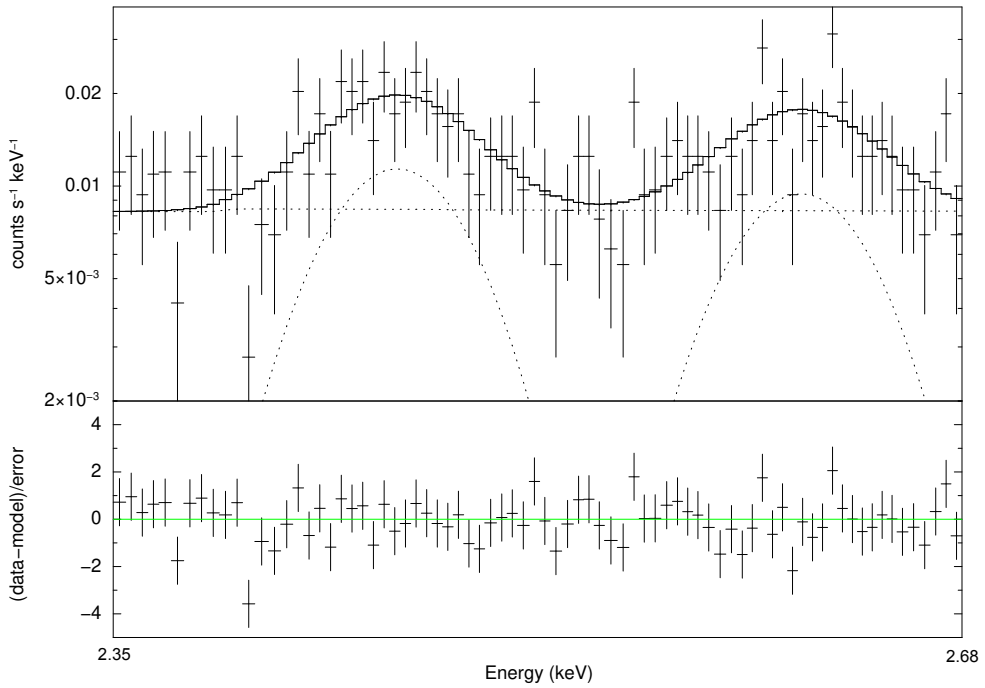

Figure 6.6: Close-up view of the synthetic XRISM-Resolve spectrum (Figure 6.5, right panel) highlighting the S XV w-z and S XVI Lyα lines (2.35 – 2.68 keV band), with the corresponding best-fit model and residual.

6.4 ^{44}Sc emission line detection in SN 1987A

Incidentally to this work, I am collaborating to the paper "Measuring the initial mass of ^{44}Ti in SN 1987A through the ^{44}Sc emission line" (Giuffrida et al., submitted to ApJ), where we measure the initial mass of ^{44}Ti in SN 1987A via its decay product, the ^{44}Sc emission line at 4.09 keV, using *Chandra* observations. Through a multi-epoch spectral analysis focusing on the inner (X-ray dim) part of the remnant, we provide the detection of the ^{44}Sc emission line in the central part of SN 1987A. From the simultaneous fit of the spectra extracted from observations between 2016 and 2021, we detect the line with a significance of 95.5% and a flux $F_{Sc} = (6 \pm 3) \times 10^{-7}$ photons s^{-1} cm^{-2}, corresponding to a mass $M_{44} = (1.5 \pm 0.7) \times 10^{-4} M_{\odot}$ (in agreement with that derived with *NuSTAR* observations by Boggs et al. 2015).

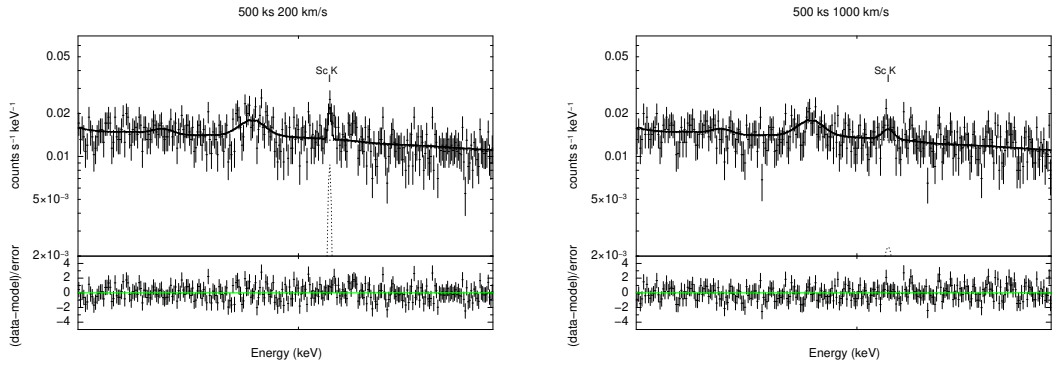

Figure 6.7: *Left panel*: XRISM-Resolve synthetic spectra in the 3.5 – 4.5 keV band obtained by adding to the thermal model the expected Sc line for the year 2024 and assuming an exposure time of 500 ks and a line width of 200 km s^{-1}. *Right panel*: Same as left panel but for a line width of 1000 km s^{-1}.

My contribution to this work is mainly focused on synthesizing the XRISM-Resolve spectra in order to asses the feasibility of a detection of the ^{44}Sc line with this instrument. SN 1987A will not be spatially resolved by the XRISM mirrors, preventing the extraction of spectra from small regions to reduce contamination from thermal X-ray emission as done with Chandra. However, the high spectral resolution provided by the XRISM-Resolve spectrometer will help in distinguishing the line from the continuum.

To this aim, I simulated the XRISM-Resolve spectra for the year 2024 using the model described in this Chapter, assuming an exposure time of 500 ks and including the effects of the gate valve closed. To this model, I added a Gaussian component to account for the ^{44}Sc line and an absorbed power law (Greco et al. 2022) for the year 2024 to model the X-ray emission of the putative PWN.

Figure 6.7 shows the synthetic spectra obtained with different line widths: 200 km s^{-1} and 1000 km s^{-1} in the left and right panels, respectively (the flux of the line being the same in both cases). If the line width associated with the ^{44}Sc bulk motion is lower than 1000 km s^{-1}, it will be possible to observe the line with high significance, its flux being larger than zero at the 99% confidence level.

6.5 Discussion and Conclusions

In this Chapter, I present a spectral synthesis of the X-ray emission of SN 1987A, mirroring the new XRISM-Resolve micro-calorimeter observation, which will take place during the PV phase of the mission, shedding new light on this intriguing celestial object.

I used a recently proposed approach, which leverages 3D MHD modelling to derive observables for different epochs, taking into account self-consistently the evolution of the remnant since the core-collapse. The resulting synthetic spectrum, which takes into account the effect of the Doppler shifts and broadening due to the bulk motion of the X-ray emitting plasma along the line of sight, shows a complex and largely broadened profile for the emission lines.

The model used in this study indicates that X-ray emission was primarily dominated by the shocked CSM, with a smaller contribution from shocked ejecta in epochs prior to 2020. This resulted in relatively narrow emission lines, reflecting the bulk motion of shocked CSM material (mainly from the ER) along the line of sight (Miceli et al. 2019, Ravi et al. 2021, Miceli 2023). I note that the emission lines predicted here for 2024 exhibit a significantly larger broadening than before. This is due to the increased contribution from shocked ejecta, which are characterized by higher velocities along the line of sight. Indeed, in 2024 the contribution to the X-ray emission stemming from freshly-shocked and fast moving ejecta will be two orders of magnitude higher than in 2011 (see Figure 6.1, lower panels). The increased Doppler broadening of the lines will provide information on the ejecta velocity (though hampering the measurement of ion temperatures).

In the model, the X-ray emission from the ejecta originates from the metal-poor outer envelope. I note that Larsson et al. (2023) recently analyzed JWST NIRSpec observations of SN 1987A, finding evidence for two Fe-rich inner ejecta plumes interacting with the reverse shock, not predicted by the model I adopted. This fast moving material could increase the emissivity of the Fe lines of the actual spectrum with respect to my predictions, thus further enhancing the broadening effect in these lines.

In any case, the measurement of the Doppler broadening will provide direct evidence for the shocked ejecta and their expansion. I have shown in Section 6.3 that a 100 ks XRISM-Resolve observation (with the gate valve open) of SN 1987A will allow me to derive the ejecta dynamics by disentangling the peaked emission of the CSM from the broad wings stemming from the ejecta in the emission lines of H-like ions, and simultaneously measuring the Doppler broadening from the emission lines of He-like ions, dominated by the ejecta emission. In particular, from the fitting of the synthetic Mg and Si line profiles (obtained with an exposure time of 100 ks) I retrieved an ejecta velocity of 3610^{+240}_{-140} km s^{-1} and 3160^{+210}_{-190} km s^{-1} (see Table 6.1). I notice that the "true" values (directly desumed from the MHD simulation) are 3480 km s^{-1} and 3280 km s^{-1}, respectively, thus confirming that synthetic spectra provide a very robust diagnostic tool. I point out that, since the emission depends on temperature, ionization parameter and particle density, I do not expect the broadening of Mg and Si lines to be exactly the same. Also for the same reason, I do not expect the ratio between ejecta and CSM for the integrated flux of the Lyα lines to be the same in Mg and Si lines.

I also show that even the forthcoming 160 ks observation (with the gate valve closed)

will make it possible to derive the ejecta dynamics by measuring the broadened S lines profile. Specifically, from the fitting of the synthetic spectrum, I retrieved a velocity of 3300^{+800}_{-700} which is remarkably in line with the velocities derived before. In a related study, (Giuffrida et al., Submitted to ApJ), I also evaluated the effectiveness of XRISM-Resolve in detecting the ^{44}Sc line in SN 1987A.

In summary, my findings represent an exploration of the spectral characteristics of SN 1987A, leveraging the capabilities of the XRISM-Resolve micro-calorimeter spectrometer. Our analysis sheds light on the diverse contributions from the CSM and ejecta in the next observations from the new satellite. I also emphasize the relevance of Doppler broadening in shaping the emission lines for future observations. These insights lay the groundwork for future observations and provide a deeper understanding of the evolving dynamics within this iconic supernova remnant.

7

Summary and Conclusions

The intricate morphologies observed in SNRs arise from inherent asymmetries in the SN explosion and the propagation of shock waves in highly inhomogeneous environments, including stellar winds swept by the progenitor system and pre-existing molecular clouds. Understanding the dynamic interplay between the ejected material shaped by the SN explosion and the surrounding CSM in forging the SNR morphology is essential for gaining insights into the nature of SN explosions, the evolution of massive stars leading up to their deaths, and the subsequent interaction between expelled stellar material and the surrounding interstellar environment. Furthermore, exploring this intricate interplay provides valuable information on the emission mechanisms within SNRs, offering crucial insights into particle acceleration processes and the origin of cosmic rays. In this thesis, I tackled these long-standing problems by addressing several open issues in SNR physics.

The first study presented in this thesis involves a spatially resolved spectral analysis of Kepler's SNR, aiming to understand how the surrounding environment influences the acceleration process. Indeed, Kepler's SNR presents a unique opportunity for this kind of studies, interacting with a dense nitrogen-rich CSM in the north and expanding in a tenuous environment in the south. This contrast provides an excellent laboratory to explore variations in synchrotron radiation features under different conditions. Utilizing archival *NuSTAR* observations, I conducted an analysis of Kepler's SNR to examine electron acceleration efficiency across its various regions. I detected a hard non-thermal X-ray emission, especially bright in the northern part where the shock front interacts with dense circumstellar material. I conducted a spatially resolved spectral analysis, combining *NuSTAR* and *XMM-Newton* spectra, employing the loss-limited synchrotron emission model by Zirakashvili & Aharonian (2007) to determine the cutoff photon energy in 11 regions. The investigation revealed distinct acceleration regimes in the northern and southern limbs of Kepler's SNR. Notably, lower Bohm factors, indicating more efficient electron acceleration, were identified in the northern shell. I proposed that

the interaction of the shock front with the high-density CSM in the north generates an amplified, possibly turbulent, magnetic field, facilitating enhanced particle acceleration. An alternative scenario positing a constant cutoff energy across the SNR shell was disfavored by the analysis. Such a scenario, in which the radiative losses do not affect the maximum electron energy, requires a magnetic field lower than observed, and it is statistically unlike although it cannot be definitively ruled out. The generated SED, incorporating *NuSTAR* X-ray data, was successfully modeled using a lepto-hadronic approach. Parameters included a magnetic field of 100 μG, a medium density of 20 cm^{-3}, electron energy $W_e = 2.7 \times 10^{47}$ erg, and proton energy $W_p = 4.2 \times 10^{48}$ erg. The density derived in the modeling aligns with that found in the northern region, suggesting that the majority of hadronic emission originates from this part of the remnant. The observed bright non-thermal hard X-ray emission in the northern half strongly indicates it as a significant site for leptonic emission as well.

However, the slow shock speed observed in the northern region (Coffin et al. 2022) induces a prolonged acceleration time scale (refer to Equation 1.23), ~300 years, potentially leading to a reduction in the maximum electron energy due to radiation losses. In an effort to untangle this intriguing scenario at smaller scales, I conducted a comprehensive study of the synchrotron flux evolution in various filaments within Kepler's SNR. For this investigation I conducted a detailed analysis of various *Chandra* archival observations of Kepler's SNR at two distinct epochs: 2006 and 2014. This follow-up study builds upon my prior research and unveils significant findings pertaining to particle acceleration and synchrotron emission dynamics within Kepler's SNR. Firstly, my investigation reaffirms the existence of two distinct regimes of particle acceleration within Kepler's SNR. This lends robust support to the hypothesis that the interaction between the shock and the dense CSM in the northern regions leads to the amplification of magnetic field turbulences. The analysis of the radio polarization fraction in Kepler's SNR adds further compelling evidence that the acceleration process is influenced by the turbulent nature of the magnetic field. The lower polarization fraction observed in the northern region, where the shock interacts with the CSM, suggests an enhancement of magnetic field turbulence in this area. Consequently, this interaction results in the acceleration of electrons in a loss-limited regime closer to the Bohm limit compared to the southern regions, where the shock interacts with a tenuous medium, exhibiting less efficient acceleration features. Furthermore, my study indicates a gradual decrease in synchrotron emission in a region at the very northern edge of the remnant, attested by a reduction in the cutoff photon energy between the two analyzed epochs. This could potentially signify the first evidence of fading synchrotron emission from a specific region in the northern part of Kepler's SNR. The observed decline in flux and cutoff energy enables the estimation of the local strength of the magnetic field. Given that in this region the shock speed is the lowest, one derives that, under a certain speed threshold, the acceleration process might exit the loss-limited regime. In summary, my research

provides a coherent and comprehensive understanding of loss-limited acceleration in Kepler's SNR. The elucidation of the role played by the CSM interacting with the shock in influencing electron acceleration, magnetic field turbulence and synchrotron emission contributes to a deeper comprehension of this fascinating celestial object.

The second part of my thesis is focused on the study of the ejecta in two core-collapse SNRs: the nearest one, Vela SNR, and the youngest one, SN 1987A.

Vela SNR, being at only 280 pc (Dodson et al. 2003), is an ideal laboratory for scrutinizing the morphology and spatial distribution of ejecta. Indeed, the remnant exhibits distinct X-ray emitting bow-shaped ejecta fragments in regions beyond the forward shock, referred to as "shrapnel" (Aschenbach et al. 1995). Among these, shrapnel A and G, located antipodally with respect to the explosion center, stand out as they are the only Shrapnel showing overabundant Si (Katsuda & Tsunemi 2006, García et al. 2017). The presence of Si-rich ejecta at such distances from the remnant's center suggests an inversion of ejecta layers during the remnant's evolution. This inversion implies that shrapnel A and G may have been part of a jet-counterjet-like event, propelling them beyond lighter ejecta and the forward shock. To test this scenario, I conducted an analysis of an *XMM-Newton* observation focusing on a bright clump, labeled "knot K," situated behind shrapnel G along the line connecting shrapnel A, G, and the SNR center with the aim of elucidating its nature. The analysis revealed two structures with distinct spectral characteristics:

- An elongated X-ray emitting plasma structure oriented prominently along the direction connecting shrapnel A and G. The highly elongated morphology of the knot, coupled with its chemical composition (consistent with that of shrapnel A and G), indicates a plausible physical connection between this jet-like elongated knot and the two Si-rich shrapnel, possibly being the trail wake of the shrapnel G.

- A narrow filament exhibiting a significantly higher temperature than the elongated knot and a distinct chemical composition. The analysis, leveraging the RASS data of Vela SNR, identified this X-ray emitting plasma structure as the southern edge of a giant filament extending from the northern rim of the shell to knot K ($\sim$ 20 pc). The characteristics of this extended filament suggest it may be a relic of a dense stellar wind blown by the progenitor star during its RSG phase, approximately 1.5 Myr before the explosion and heated by the shock wave. The distinctive Ne/O ratio in the wind residual hints at a Wolf-Rayet progenitor for Vela SNR.

This comprehensive analysis provides insights into the complex dynamics of the Vela SNR, shedding light on the interplay between the Si-rich ejecta, a jet-like structure, and a stellar wind-blown relic, ultimately contributing to a deeper understanding of the progenitor star's evolutionary history.

SN 1987A is a SNR evolving in a highly inhomogeneous CSM, offering the unique opportunity to study the transition from a SN to its SNR across the whole electromagnetic

spectrum. Current models indicate that the remnant is entering a phase where X-ray emission is primarily driven by the outermost SN ejecta, heated by the reverse shock. Consequently, the observation of X-ray features from the shocked ejecta is expected in the near future. In this thesis I presented a spectral synthesis of the X-ray emission of SN 1987A, anticipating the upcoming XRISM-Resolve micro-calorimeter observation during the PV phase of the mission. My approach leveraged a recently proposed method based on 3D MHD modeling, providing observables for different epochs while self-consistently considering the remnant's evolution since core-collapse. The resulting synthetic spectrum, accounting for Doppler shifts and broadening due to the bulk motion of the X-ray emitting plasma along the line of sight, reveals complex and largely broadened emission line profiles. Notably, the predicted emission lines for 2024 exhibit significantly larger broadening than those observed up to now, as a result of the increased contribution from shocked ejecta, which are characterized by higher velocities along the line of sight. Specifically, the X-ray emission from freshly-shocked and fast-moving ejecta in 2024 is expected to be two orders of magnitude higher than in 2011, leading to increased Doppler broadening that might result in the first unambiguous detection of X-ray emissing ejecta in SN 1987A, also providing valuable information on the ejecta velocity. This fast-moving material could enhance the emissivity of Fe lines in the actual spectrum, further amplifying the broadening effect in these lines. In summary, my analysis highlighted the diverse contributions from the CSM and ejecta in the upcoming observations from the new XRISM X-ray telescope. I underscored the significance of Doppler broadening in shaping the emission lines for future observations, providing crucial insights into the evolving dynamics within this iconic SNR and laying the groundwork for further investigations.

7.1 Future prospects

Starting from my background, from the acquired expertise on X-ray emission data analysis, I plan to analyze archival observations, and propose new ones. With a series of tools I personally developed, I will investigate and identify structures associated with anisotropies in the ejecta and wind residuals, to understand the role of these features in characterizing the acceleration processes for several SNRs. My research will be focused mainly on two different lines:

1. Deciphering the origin of anisotropies in SNRs;
2. Studying the cosmic ray acceleration process in SNRs evolving in an inhomogeneous ambient medium.

These two points are tightly correlated, given that, e.g., thermal emission can provide constraints on the plasma density (which is important to estimate the hadronic gamma-ray

emission), and on the back-reaction of cosmic ray acceleration on the hydrodynamics of the post-shock flow. Since core-collapse SNRs typically exhibit a high level of anisotropy due to the deviation from the spherical symmetry in the SN explosion and to the propagation of the shock-waves in inhomogeneous environments, my research will focus on obtaining insight on the physical and chemical parameters determining the degree of anisotropy in the outcome of the explosion, which is important to constrain the processes at work in a core-collapse SN. At the same time, I will also investigate the role of the late evolution of the progenitor star in shaping the anisotropies. Progenitor stars can produce wind blown bubbles (surrounded by dense cavity walls), circumstellar rings (as in SN 1987A), as well as knotty, dense, and irregular shells of wind residuals (like the one I discovered in the Vela SNR) and pre-SN bursts. To properly understand the lack of symmetry in core-collapse SNRs, I plan to disentangle the effects of the initial conditions (anisotropies in the SN explosion) from those of the ambient conditions (propagation of the shock front in a complex environment).

To this end, I will start an investigation on the spatial distribution of the ejecta, using advanced statistical tools (and developing machine learning tools) to analyze the X-ray observations in several galactic core-collapse SNRs, with the aim of find asymmetries and collimated structures and link them with anisotropies in the SN explosion, as well as find some relation between the various structures of the different SNRs. Then, I will focus on the study of the shock interaction with dense wind residuals. I will study the inhomogeneities in the CSM and the chemical composition of the wind residuals, which I plan to compare with that predicted by stellar evolution codes (as MESA and FRAMEC), to derive information on the progenitor mass and rotation.

The results obtained during my PhD show that turbulence in the medium where the shock front propagates significantly affect the efficiency of particle acceleration. Besides the results that I obtained for Kepler's SNR, similar findings have been obtained for RX J1713.7-3946 (Inoue et al. 2012, Sano et al. 2015). I plan to expand this promising study. Indeed, my results suggest possible temporal variations in the X-ray fluxes in the regions of SNRs interacting with dense material (with a characteristic time scale of the order of a decade). I will extend this analysis to other remnants and expand the investigation by considering also the polarization of the X-ray synchrotron radiation, by taking advantage of observation that are provided by the *IXPE* telescope, and of the observations I plan to propose.

Moreover, I will link the properties of nonthermal X-ray emission with those of the $\gamma-$ray radiation (Inverse Compton, and hadronic emission), using computational codes for nonthermal radiation from relativistic particle populations (e.g. *Naima*, Zabalza 2015), like I did for Kepler's SNR. In this framework, I have been recently approved an *XMM-Newton* proposal of observation pointing towards the $\gamma-$ray emitting SNR G106.3+2.7. The aim is to seek for synchrotron emission that would be the signature of secondary leptons produced by the interaction with ambient protons of very high-energy

cosmic rays accelerated in this Pevatron candidate.

Appendices

Appendix to Chapter 3

A.1 Proper motion

To estimate the current velocity of the shock front in regions 1-11 (shown in Figure 3.1), I considered the proper motion measurements by Coffin et al. (2022) and Katsuda et al. (2008). These measurements were obtained in small (with respect to our regions 1-11) regions at the shock front. For each region I considered the closest region(s) by Coffin et al. (2022), when available, and by Katsuda et al. (2008) elsewhere, as shown in detail in Table A.1. When more than one measurement of the proper motion were available, I considered their arithmetic mean. I did not find measurements of the proper motion in the areas of the shell corresponding to our region 1 and 10.

Table A.1: Match between regions with proper motion measurements available in the literature, and regions from this work.

Region #	Coffin et al. (2022) Region #	Katsuda et al. (2008) Region #
1	/	/
2	7	/
3	8-9	/
4	9	/
5	/	9-10-11
6	/	13
7	16	/
8	1	/
9	2	/
10	/	/
11	3-4	/

Acronym Index

ACIS = Advanced CCD Imaging Spectrometer
AGB = Asymptotic Giant Branch
ARF = Ancillary Response File
BS = Blank Sky
CALDB = CALibration DataBase
CCD = Charge-Coupled Device
CCF = Current Calibration Files
CCSN = Core-Collapse SuperNova
CIAO = *Chandra* Interactive Analysis of Observation
CIE = Collisional Ionization Equilibrium
CMB = Cosmic Microwave Background
CR = Cosmic Ray
CSM = CircumStellar Medium
CTAO = Cherenkov Telescope Array Observatory
CXO = *Chandra* X-ray Observatory
CZT = CdZnTe (Cadmium Zinc Telluride)
DD = Double Degenerate
Dec = Declination
dof = degrees of freedom
DSA = Diffusive Shock Acceleration
EFF = Extended Full Frame
EM = Emission Measure
ER = Equatorial Ring
ESA = European Space Agency
ESAC = European Space Astronomy Center
EPIC = European Photon Imaging Camera

eROSITA = extended ROentgen Survey with an Imaging Telescope Array
FermiLAT = Fermi Large Area Telescope
FF = Full Frame
FIR = Far InfraRed
FoV = Field of View
FPMA/B = Focal Plane Module A/B
FWC = Filter Wheel Closed
FWHM = Full Width Half Maximum
GTI = Good Time Intervals
HD = HydroDynamic
HEO = High Elliptical Orbit
HESS = High Energy Stereoscopic System
HEW = Half Energy Width
HRC = High Resolution Camera
HRI = High Resolution Imager
HXD = Hard X-ray Detector
IC = Inverse Compton
IR = InfraRed
ISM = InterStellar Medium
JAXA = Japan Aerospace eXploration Agency
JWST = James Webb Space Telescope
LEO = Low Earth Orbit
LMC = Large Magellanic Cloud MAGIC = Major Atmosphere Gamma-ray Imaging Cherenkov
MHD = Magneto-HydroDynamic
MOS = Metal Oxide Semiconductor
MPE = Median Photon Energy
NASA = National Aeronautics and Space Administration
NEI = Non Equilibrium Ionization
NIR = Near InfraRed
NS = Neutron Star
NuSTAR = Nuclear Spectroscopic Telescope ARray
NuSTARDAS = NuSTAR Data Analysis Software
ODF = Observation Data Files
OM = Optical Mirror
PI = Principal Investigator
PIMMS = Portable Interactive Multi-Mission Simulator
PNS = Proto-Neutron Star
PSF = Point Spread Function
PSPC = Position Sensitive Proportional Counter

PV = Performance Verification
PWN = Pulsar Wind Nebula
RA = Right Ascension
RASS = ROSAT All Sky Survey
RGS = Reflection Grating Spectrometer
ROSAT = ROentgen SATellite
RMF = Redistribution Matrix File
RRC = Radiative Recombination Continuum
RSG = Red SuperGiant
SD = Single Degenerate
S/N = Signal-to-noise ratio
SAS = Science Analysis Software
SASI = Standing Accretion Shock Instability
SED = Spectral Energy Distribution
SIM = Science Instrument Module
SN = SuperNova
SNR = SuperNova Remnant
SOC = Scientific Organization Committee
SRG = Spektrum-Roentgen-Gamma
UV = UltraViolet
VERITAS = Very Energetic Radiation Imaging Telescope Array System
VHE = Very High Energy
WD = White Dwarf
XMA = X-ray Mirror Assembly
XMM-Newton = X-ray Multi-mirror Mission Newton
XRISM = X-Ray Imaging and Spectroscopy Mission
XRT = X-Ray Telescope
XSA = *XMM-Newton* Science Archive
XSPEC = X-ray SPECtral fitting package

Acknowledgements

I would like to acknowledge the referees of my doctoral thesis, Dr. Tea Temim and Dr. Ping Zhou. Their insightful comments and rigorous scrutiny have contributed to the refinement of this work.

I would like to express most sincere gratitude to my supervisor, Marco Miceli. Without his support, guidance and encouragement, this thesis simply would not have been possible. Academically speaking (and not), he has been like a father to me and a truly valuable friend, helping me to grow as a scientist and as a man. I cannot thank him enough, also for the *Pizzette* and the coffee, which he offered. I want to thank also my colleague Roberta, who shared with me the same "father", the same coffee breaks, the same academic journey and a lot of adventurous "missions". *S2*.

I want to acknowledge Dr. Salvatore Orlando for the priceless support, comments and contributions to the studies I have extensively wrote on this manuscript. Part of this thesis would have not been possible without his hard work. My thanks extend to all the people of the SNR OAPa group for their ideas and input, that were always helpful.

I would like acknowledge professor Aya Bamba and everyone at Bamba-ken. Their engaging discussions, warm welcome, and both financial and non-financial support greatly facilitated my time in Tokyo. I would also like to express my heartfelt gratitude to my dear friend Saki, with whom I shared unforgettable experiences and countless memories during my time in Japan. Unflagging hiking partner and her kindness and cheerful spirit made my journey in Japan truly worthwhile. Living in Japan, as an Italian, can be though if you cannot find any kind of pasta different from *Spaghetti*, therefore I acknowledge my friend Riccardo for a three month worthy pasta supply, but also for the karaoke nights and the some of the most peculiar experiences of my life.

I want to express my gratitude to all the people at the 2^{nd} floor of via Archirafi 36, for make me feel like I was home. A special mention goes to Alessio, "my partner in crime"

during the days at the department but especially during the craziest nights. *Tisanina?*

I would like to extend my heartfelt thanks to all my friends. To those I've met and those I've parted ways with over the years, your presence has shaped my life in countless ways. Whether near or far, your companionship is invaluable to me.

Special thanks goes to my family who never stopped to believe in me. Your constant encouragement and understanding have been a source of strength. *Grazie Mamma, Papá, Salvo e Chiara.* I have to say that my family does not stop there, I indeed want to thank my uncle, my aunt, and my cousins for their unconditional love.

Un ringraziamento speciale va alla mia famiglia che non ha mai smesso un giorno di credere in me. Il vostro costante incoraggiamento e la vostra compresione sono stati la mia forza. Grazie Mamma, Papá, Salvo e Chiara. La mia famiglia non finisce mica qui, voglio infatti ringraziare i miei zii e le mie cugine per il loro amore incodizionato nei miei confronti.

Dulcis in fundo I want to thank my girlfriend Gabriella for being amazingly supportive. Even if we met recently, she has stood by me during one of the most thought period of my PhD journey, writing this thesis. *Grazie Giuggi*

Bibliography

Abellán, F. J., Indebetouw, R., Marcaide, J. M., et al. 2017, Astrophysical Journal Supplements Letters, 842, L24

Acero, F., Lemoine-Goumard, M., & Ballet, J. 2022, Astronomy and Astrophysics, 660, A129

Acero, F. et al. 2016, Astrophysical Journal Supplements Series, 224, 8

Ackermann, M., Ajello, M., Allafort, A., et al. 2013, Science, 339, 807

Aharonian, F., Akhperjanian, A. G., Barres de Almeida, U., et al. 2008, Astronomy and Astrophysics, 488, 219

Aharonian, F. A. & Atoyan, A. M. 1999, Astronomy and Astrophysics, 351, 330

Aleksić, J., Alvarez, E. A., Antonelli, L. A., et al. 2012, Astronomy and Astrophysics, 541, A13

Aloy, M. Á. & Obergaulinger, M. 2021, Monthly Noticed Royal Astronomical Society, 500, 4365

Anders, E. & Grevesse, N. 1989, Geochimica and Cosmochimica Acta, 53, 197

Arnaud, K. A. 1996, Astronomical Society of the Pacific Conference Series, Vol. 101, XSPEC: The First Ten Years, ed. G. H. Jacoby & J. Barnes, 17

Aschenbach, B., Egger, R., & Trümper, J. 1995, Nature, 373, 587

Axford, W. I., Leer, E., & Skadron, G. 1977, in International Cosmic Ray Conference, Vol. 11, International Cosmic Ray Conference, 132

Baade, W. & Zwicky, F. 1934a, Proceedings of the National Academy of Science, 20, 259

Baade, W. & Zwicky, F. 1934b, Proceedings of the National Academy of Science, 20, 254

Balsara, D., Benjamin, R. A., & Cox, D. P. 2001, Astrophysical Journal, 563, 800

Bamba, A., Ueno, M., Nakajima, H., & Koyama, K. 2004, Astrophysical Journal, 602, 257

Bamba, A., Yamazaki, R., Yoshida, T., Terasawa, T., & Koyama, K. 2005, Astrophysical Journal, 621, 793

Bandiera, R. 1987, Astrophysical Journal, 319, 885

Bandiera, R. & Petruk, O. 2016, Monthly Noticed Royal Astronomical Society, 459, 178

Bear, E. & Soker, N. 2018, Astrophysical Journal, 855, 82

Bell, A. R. 1978a, Monthly Noticed Royal Astronomical Society, 182, 147

Bell, A. R. 1978b, Monthly Noticed Royal Astronomical Society, 182, 443

Bell, A. R. 2004, Monthly Noticed Royal Astronomical Society, 353, 550

Bennett, L. & Ellison, D. C. 1995, Journal of Geophysical Research, 100, 3439

Beuermann, K., Brandt, S., & Pietsch, W. 1994, Astronomy and Astrophysics, 281, L45

Blair, W. P., Ghavamian, P., Long, K. S., et al. 2007, Astrophysical Journal, 662, 998

Blandford, R. D. & McKee, C. F. 1976, Physics of Fluids, 19, 1130

Blandford, R. D. & Ostriker, J. P. 1978, Astrophysical Journal Supplements Letters, 221, L29

Blondin, J. M. & Mezzacappa, A. 2007, Nature, 445, 58

Blondin, J. M., Mezzacappa, A., & DeMarino, C. 2003, Astrophysical Journal, 584, 971

Boggs, S. E., Harrison, F. A., Miyasaka, H., et al. 2015, Science, 348, 670

Borkowski, K. J., Blondin, J. M., & McCray, R. 1997, Astrophysical Journal, 477, 281

Caraveo, P. A., De Luca, A., Mignani, R. P., & Bignami, G. F. 2001, Astrophysical Journal, 561, 930

Cassam-Chenaï, G., Decourchelle, A., Ballet, J., et al. 2004, Astronomy and Astrophysics, 414, 545

Chevalier, R. A. 1982, Astrophysical Journal, 258, 790

Chieffi, A. & Limongi, M. 2013, Astrophysical Journal, 764, 21

Chiotellis, A., Schure, K. M., & Vink, J. 2012, Astronomy and Astrophysics, 537, A139

Coffin, S. C., Williams, B. J., & Katsuda, S. 2022, Astrophysical Journal, 926, 84

Collaboration, H. 2018, VizieR Online Data Catalog, J/A+A/612/A3

DeLaney, T., Koralesky, B., Rudnick, L., & Dickel, J. R. 2002, Astrophysical Journal, 580, 914

Dickel, J. R., Strom, R. G., & Milne, D. K. 2001, Astrophysical Journal, 546, 447

Dodson, R., Legge, D., Reynolds, J. E., & McCulloch, P. M. 2003, Astrophysical Journal, 596, 1137

Dotani, T., Hayashida, K., Inoue, H., et al. 1987, Nature, 330, 230

Dubner, G., Loiseau, N., Rodríguez-Pascual, P., et al. 2013, Astronomy and Astrophysics, 555, A9

Eichler, D. 1979, Astrophysical Journal, 229, 419

Ellison, D. C. & Eichler, D. 1984, Astrophysical Journal, 286, 691

Foglizzo, T. 2016, in Handbook of Supernovae, ed. A. W. Alsabti & P. Murdin (Cham: Springer International Publishing), 1–21

Frank, K. A., Zhekov, S. A., Park, S., et al. 2016, Astrophysical Journal, 829, 40

Fransson, C., Barlow, M. J., Kavanagh, P. J., et al. 2024, Science, 383, 898

Gabici, S., Evoli, C., Gaggero, D., et al. 2019, International Journal of Modern Physics D, 28, 1930022

García, F., Suárez, A. E., Miceli, M., et al. 2017, Astronomy and Astrophysics, 604, L5

Giacalone, J. & Jokipii, J. R. 2007, Astrophysical Journal Supplements Letters, 663, L41

Ginzburg, V. L. & Syrovatskii, S. I. 1965, Annual Review of Astronomy and Astrophysics, 3, 297

Giuffrida, R., Miceli, M., Caprioli, D., et al. 2022, Nature Communications, 13, 5098

Greco, E., Miceli, M., Orlando, S., et al. 2021, Astrophysical Journal Supplements Letters, 908, L45

Greco, E., Miceli, M., Orlando, S., et al. 2022, Astrophysical Journal, 931, 132

Greco, E., Miceli, M., Orlando, S., et al. 2018, Astronomy and Astrophysics, 615, A157

Greco, E., Vink, J., Miceli, M., et al. 2020, Astronomy and Astrophysics, 638, A101

Greggio, L., Renzini, A., & Daddi, E. 2008, Monthly Noticed Royal Astronomical Society, 388, 829

H. E. S. S. Collaboration, Abdalla, H., Abramowski, A., et al. 2018, Astronomy and Astrophysics, 612, A5

H. E. S. S. Collaboration, Aharonian, F., Ait Benkhali, F., et al. 2022, Astronomy and Astrophysics, 662, A65

Haas, M. R., Colgan, S. W. J., Erickson, E. F., et al. 1990, Astrophysical Journal, 360, 257

Haberl, F., Geppert, U., Aschenbach, B., & Hasinger, G. 2006, Astronomy and Astrophysics, 460, 811

Hess, V. F. 1912, Phys. Z., 13, 1084

Hillas, A. M. 2005, Journal of Physics G Nuclear Physics, 31, R95

Hirata, K., Kajita, T., Koshiba, M., et al. 1987, Physical Review Letters, 58, 1490

Holland-Ashford, T., Slane, P., Lopez, L. A., Auchettl, K., & Kashyap, V. 2023, Astrophysical Journal, 955, 77

Hoyle, F. & Fowler, W. A. 1960, Astrophysical Journal, 132, 565

Hui, C. Y. & Becker, W. 2006, Astronomy and Astrophysics, 454, 543

Hwang, U. & Laming, J. M. 2012, Astrophysical Journal, 746, 130

Inoue, T., Yamazaki, R., Inutsuka, S.-i., & Fukui, Y. 2012, Astrophysical Journal, 744, 71

Ishisaki, Y., Kelley, R. L., Awaki, H., et al. 2022, in Society of Photo-Optical Instrumentation Engineers (SPIE) Conference Series, Vol. 12181, Space Telescopes and Instrumentation 2022: Ultraviolet to Gamma Ray, ed. J.-W. A. den Herder, S. Nikzad, & K. Nakazawa, 121811S

Ivanova, N., Podsiadlowski, P., & Spruit, H. 2002, Monthly Noticed Royal Astronomical Society, 334, 819

Izzo, L., de Ugarte Postigo, A., Maeda, K., et al. 2019, Nature, 565, 324

Janka, H.-T. 2017, in Handbook of Supernovae, ed. A. W. Alsabti & P. Murdin, 1575

Janka, H. T., Langanke, K., Marek, A., Martínez-Pinedo, G., & Müller, B. 2007, Physics Reports, 442, 38

Kaastra, J. S. & Bleeker, J. A. M. 2016, Astronomy and Astrophysics, 587, A151

Kasuga, T., Vink, J., Katsuda, S., et al. 2021, Astrophysical Journal, 915, 42

Katsuda, S., Mori, K., Maeda, K., et al. 2015, Astrophysical Journal, 808, 49

Katsuda, S., Mori, K., Petre, R., et al. 2011, Publication of the Astronomical Society of Japan, 63, S827

Katsuda, S. & Tsunemi, H. 2005, Publication of the Astronomical Society of Japan, 57, 621

Katsuda, S. & Tsunemi, H. 2006, Astrophysical Journal, 642, 917

Katsuda, S., Tsunemi, H., & Mori, K. 2008, Astrophysical Journal Supplements Letters, 678, L35

Katsuda, S., Tsunemi, H., Uchida, H., & Kimura, M. 2008, The Astrophysical Journal, 689, 225

Kawasaki, M. T., Ozaki, M., Nagase, F., et al. 2002, Astrophysical Journal, 572, 897

Kerzendorf, W. E. & Sim, S. A. 2014, Monthly Noticed Royal Astronomical Society, 440, 387

Kinugasa, K. & Tsunemi, H. 1999, Publication of the Astronomical Society of Japan, 51, 239

Koyama, K., Petre, R., Gotthelf, E. V., et al. 1995, Nature, 378, 255

LaMassa, S. M., Slane, P. O., & de Jager, O. C. 2008, Astrophysical Journal Supplements Letters, 689, L121

Laming, J. M., Hwang, U., Radics, B., Lekli, G., & Takács, E. 2006, Astrophysical Journal, 644, 260

Landau, L. D. & Lifshitz, E. M. 1959, Fluid mechanics

Larsson, J., Fransson, C., Sargent, B., et al. 2023, Astrophysical Journal Supplements Letters, 949, L27

Limongi, M. & Chieffi, A. 2018, Astrophysical Journal Supplements Series, 237, 13

Longair, M. S. 2011, High Energy Astrophysics

Lopez, L. A., Grefenstette, B. W., Auchettl, K., Madsen, K. K., & Castro, D. 2020, Astrophysical Journal, 893, 144

Lopez, L. A., Grefenstette, B. W., Reynolds, S. P., et al. 2015, Astrophysical Journal, 814, 132

Lopez, L. A., Pearson, S., Ramirez-Ruiz, E., et al. 2013, Astrophysical Journal, 777, 145

Lu, F. J. & Aschenbach, B. 2000, Astronomy and Astrophysics, 362, 1083

Madsen, K. K., Beardmore, A. P., Forster, K., et al. 2017, Astronomical Journal, 153, 2

Maggi, P., Haberl, F., Sturm, R., & Dewey, D. 2012, Astronomy and Astrophysics, 548, L3

Maitra, C., Haberl, F., Sasaki, M., et al. 2022, Astronomy and Astrophysics, 661, A30

Malkov, M. A. & Drury, L. O. 2001, Reports on Progress in Physics, 64, 429

Matheson, H. & Safi-Harb, S. 2005, Advances in Space Research, 35, 1099

McCray, R. & Fransson, C. 2016, Annual Review of Astronomy and Astrophysics, 54, 19

McKee, C. F. 1974, Astrophysical Journal, 188, 335

Mewe, R. 1999, in X-Ray Spectroscopy in Astrophysics, ed. J. van Paradijs & J. A. M. Bleeker, Vol. 520, 109

Mezzacappa, A. 2005, Annual Review of Nuclear and Particle Science, 55, 467

Miceli, M. 2023, Plasma Physics and Controlled Fusion, 65, 034003

Miceli, M., Bamba, A., Orlando, S., et al. 2017, Astronomy and Astrophysics, 599, A45

Miceli, M., Bocchino, F., Decourchelle, A., Ballet, J., & Reale, F. 2010, Astronomy and Astrophysics, 514, L2

Miceli, M., Bocchino, F., Decourchelle, A., et al. 2012, Astronomy and Astrophysics, 546, A66

Miceli, M., Bocchino, F., Decourchelle, A., et al. 2013a, Astronomy and Astrophysics, 556, A80

Miceli, M., Bocchino, F., Maggio, A., & Reale, F. 2005, Astronomy and Astrophysics, 442, 513

Miceli, M., Bocchino, F., & Reale, F. 2008a, Astrophysical Journal, 676, 1064

Miceli, M., Decourchelle, A., Ballet, J., et al. 2008b, Advances in Space Research, 41, 390

Miceli, M., Decourchelle, A., Ballet, J., et al. 2006, Astronomy and Astrophysics, 453, 567

Miceli, M., Orlando, S., Burrows, D. N., et al. 2019, Nature Astronomy, 3, 236

Miceli, M., Orlando, S., Reale, F., Bocchino, F., & Peres, G. 2013b, Monthly Noticed Royal Astronomical Society, 430, 2864

Minkowski, R. 1941, Publications of the Astronomical Society of the Pacific, 53, 224

Morlino, G. & Caprioli, D. 2012, Astronomy and Astrophysics, 538, A81

Nagayoshi, T., Bamba, A., Katsuda, S., & Terada, Y. 2021, Publication of the Astronomical Society of Japan, 73, 302

Nomoto, K., Thielemann, F. K., & Yokoi, K. 1984, Astrophysical Journal, 286, 644

Obergaulinger, M. & Aloy, M. Á. 2020, Monthly Noticed Royal Astronomical Society, 492, 4613

Obergaulinger, M. & Aloy, M. Á. 2021, Monthly Noticed Royal Astronomical Society, 503, 4942

Obergaulinger, M. & Aloy, M. Á. 2022, Monthly Noticed Royal Astronomical Society, 512, 2489

Obergaulinger, M., Cerdá-Durán, P., Müller, E., & Aloy, M. A. 2009, Astronomy and Astrophysics, 498, 241

Olinto, A. V. 2001, in Relativistic Aspects of Nuclear Physics (WORLD SCIENTIFIC)

Ono, M., Nagataki, S., Ferrand, G., et al. 2020, Astrophysical Journal, 888, 111

Orlando, S., Bocchino, F., Reale, F., Peres, G., & Pagano, P. 2008, Astrophysical Journal, 678, 274

Orlando, S., Miceli, M., Petruk, O., et al. 2019, Astronomy and Astrophysics, 622, A73

Orlando, S., Miceli, M., Pumo, M. L., & Bocchino, F. 2015, Astrophysical Journal, 810, 168

Orlando, S., Miceli, M., Pumo, M. L., & Bocchino, F. 2016, Astrophysical Journal, 822, 22

Orlando, S., Ono, M., Nagataki, S., et al. 2020, Astronomy and Astrophysics, 636, A22

Orlando, S., Wongwathanarat, A., Janka, H. T., et al. 2021, Astronomy and Astrophysics, 645, A66

Pakmor, R., Kromer, M., Röpke, F. K., et al. 2010, Nature, 463, 61

Pakmor, R., Kromer, M., Taubenberger, S., et al. 2012, Astrophysical Journal Supplements Letters, 747, L10

Panagia, N. 1999, in New Views of the Magellanic Clouds, ed. Y. H. Chu, N. Suntzeff, J. Hesser, & D. Bohlender, Vol. 190, 549

Parizot, E., Marcowith, A., Ballet, J., & Gallant, Y. A. 2006, Astronomy and Astrophysics, 453, 387

Park, S. & Bhalerao, J. 2017, Astrophysical Journal, 834, 189

Park, S., Zhekov, S. A., Burrows, D. N., et al. 2006, Astrophysical Journal, 646, 1001

Park, S., Zhekov, S. A., Burrows, D. N., & McCray, R. 2005, Astrophysical Journal Supplements Letters, 634, L73

Phillips, M. M. 1993, Astrophysical Journal Supplements Letters, 413, L105

Ravi, A. P., Park, S., Zhekov, S. A., et al. 2021, Astrophysical Journal, 922, 140

Raymond, J. C., Winkler, P. F., Blair, W. P., & Laming, J. M. 2017, Astrophysical Journal, 851, 12

Rettig, R. & Pohl, M. 2012, Astronomy and Astrophysics, 545, A47

Reynolds, S. P. 1998, Astrophysical Journal, 493, 375

Reynolds, S. P. 2008, Annual Review of Astronomy and Astrophysics, 46, 89

Reynolds, S. P., Borkowski, K. J., Hwang, U., et al. 2007, Astrophysical Journal Supplements Letters, 668, L135

Reynolds, S. P., Williams, B. J., Borkowski, K. J., & Long, K. S. 2021, Astrophysical Journal, 917, 55

Reynoso, E. M. & Goss, W. M. 1999, Astronomical Journal, 118, 926

Reynoso, E. M., Green, A. J., Johnston, S., et al. 2003, Monthly Noticed Royal Astronomical Society, 345, 671

Ruiz-Lapuente, P., Damiani, F., Bedin, L., et al. 2018, Astrophysical Journal, 862, 124

Sankrit, R., Raymond, J. C., Blair, W. P., et al. 2016, Astrophysical Journal, 817, 36

Sano, H., Fukuda, T., Yoshiike, S., et al. 2015, Astrophysical Journal, 799, 175

Sapienza, V. 2023, in Proceedings of 38th International Cosmic Ray Conference — PoS(ICRC2023), Vol. 444, 843

Sapienza, V., Miceli, M., Bamba, A., et al. 2022, Astrophysical Journal, 935, 152

Sapienza, V., Miceli, M., Bamba, A., et al. 2024, The Astrophysical Journal Letters, 961, L9

Sapienza, V., Miceli, M., Peres, G., et al. 2021, Astronomy and Astrophysics, 649, A56

Sato, T. & Hughes, J. P. 2017, Astrophysical Journal, 845, 167

Sedov, L. I. 1959, Similarity and Dimensional Methods in Mechanics (Academic Press)

Slane, P., Lovchinsky, I., Kolb, C., et al. 2018, Astrophysical Journal, 865, 86

Smith, R. K. & Hughes, J. P. 2010, Astrophysical Journal, 718, 583

Spitzer, L. 2006, Physics of fully ionized gases; 2nd rev. ed. (Mineola, NY: Dover)

Strong, A. W., Moskalenko, I. V., & Ptuskin, V. S. 2007, Annual Review of Nuclear and Particle Science, 57, 285

Sugerman, B. E. K., Crotts, A. P. S., Kunkel, W. E., Heathcote, S. R., & Lawrence, S. S. 2005, Astrophysical Journal Supplements Series, 159, 60

Sun, L., Vink, J., Chen, Y., et al. 2021, Astrophysical Journal, 916, 41

Suzuki, H., Katsuda, S., Tanaka, T., et al. 2022, Astrophysical Journal, 938, 59

Tashiro, M., Maejima, H., Toda, K., et al. 2020, in Society of Photo-Optical Instrumentation Engineers (SPIE) Conference Series, Vol. 11444, Space Telescopes and Instrumentation 2020: Ultraviolet to Gamma Ray, ed. J.-W. A. den Herder, S. Nikzad, & K. Nakazawa, 1144422

Taylor, G. 1950, Proceedings of the Royal Society of London Series A, 201, 159

Taylor, J. H., Manchester, R. N., & Lyne, A. G. 1993, Astrophysical Journal Supplements Series, 88, 529

Temim, T. & Slane, P. 2017, in Astrophysics and Space Science Library, Vol. 446, Modelling Pulsar Wind Nebulae, ed. D. F. Torres, 29

Temim, T., Slane, P., Sukhbold, T., et al. 2019, Astrophysical Journal Supplements Letters, 878, L19

Treumann, R. A. 2009, The Astronomy and Astrophysics Review, 17, 409

Truelove, J. K. & McKee, C. F. 1999, Astrophysical Journal Supplements Series, 120, 299

Tsebrenko, D. & Soker, N. 2015, Monthly Noticed Royal Astronomical Society, 453, 166

Tsuji, N., Uchiyama, Y., Khangulyan, D., & Aharonian, F. 2021, Astrophysical Journal, 907, 117

Tutone, A., Orlando, S., Miceli, M., et al. 2020, Astronomy and Astrophysics, 642, A67

Urushibata, T., Takahashi, K., Umeda, H., & Yoshida, T. 2018, Monthly Noticed Royal Astronomical Society, 473, L101

Velázquez, P. F., Vigh, C. D., Reynoso, E. M., Gómez, D. O., & Schneiter, E. M. 2006, Astrophysical Journal, 649, 779

Vink, J. 2004, New Astronomy Review, 48, 61

Vink, J. 2008, Astrophysical Journal, 689, 231

Vink, J. 2020, Physics and Evolution of Supernova Remnants

Vink, J., Bleeker, J., van der Heyden, K., et al. 2006, Astrophysical Journal Supplements Letters, 648, L33

Vink, J., Prokhorov, D., Ferrazzoli, R., et al. 2022, Astrophysical Journal, 938, 40

Völk, H. J., Berezhko, E. G., & Ksenofontov, L. T. 2005, Astronomy and Astrophysics, 433, 229

West, R. M., Lauberts, A., Jorgensen, H. E., & Schuster, H. E. 1987, Astronomy and Astrophysics, 177, L1

Wheeler, J. C., Meier, D. L., & Wilson, J. R. 2002, Astrophysical Journal, 568, 807

Whelan, J. & Iben, Icko, J. 1973, Astrophysical Journal, 186, 1007

Williams, B. J., Chomiuk, L., Hewitt, J. W., et al. 2016, Astrophysical Journal Supplements Letters, 823, L32

Wolter, H. 1952, Annalen der Physik, 445, 94

Woltjer, L. 1972, Annual Review of Astronomy and Astrophysics, 10, 129

Woosley, S. & Janka, T. 2005, Nature Physics, 1, 147

Xiang, Y. & Jiang, Z. 2021, Astrophysical Journal, 908, 22

Yamaguchi, H. 2020, Astronomische Nachrichten, 341, 150

Yamaguchi, H., Bamba, A., & Koyama, K. 2009, Publication of the Astronomical Society of Japan, 61, S175

Yamaguchi, H., Katsuda, S., Castro, D., et al. 2016, Astrophysical Journal Supplements Letters, 820, L3

Yang, X. J., Tsunemi, H., Lu, F. J., et al. 2013, Astrophysical Journal, 766, 44

Zabalza, V. 2015, Proc. of International Cosmic Ray Conference 2015, 922

Zhekov, S. A., McCray, R., Dewey, D., et al. 2009, Astrophysical Journal, 692, 1190

Zhou, P., Prokhorov, D., Ferrazzoli, R., et al. 2023, Astrophysical Journal, 957, 55

Zhou, P. & Vink, J. 2018, Astronomy and Astrophysics, 615, A150

Zhou, X., Miceli, M., Bocchino, F., Orlando, S., & Chen, Y. 2011, Monthly Noticed Royal Astronomical Society, 415, 244

Zirakashvili, V. N. & Aharonian, F. 2007, Astronomy and Astrophysics, 465, 695

Zirakashvili, V. N. & Aharonian, F. A. 2010, Astrophysical Journal, 708, 965